eman ta zabal zazu

Universidad del País Vasco
Euskal Herriko Unibertsitatea

ELECTRON DYNAMICS IN THE INTERACTION OF ATOMIC PARTICLES WITH SPHERICAL METAL CLUSTERS

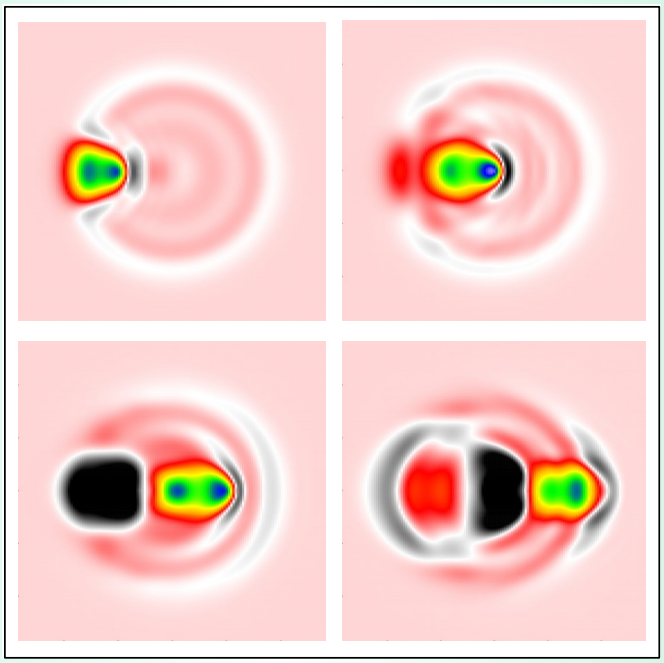

DOCTORAL THESIS SUBMITTED TO THE
UNIVERSITY OF THE BASQUE COUNTRY
FOR THE DEGREE OF DOCTOR IN PHYSICS

BY NATALIA KOVAL

2016

eman ta zabal zazu

Universidad del País Vasco
Euskal Herriko Unibertsitatea

PhD Thesis

Electron Dynamics in the Interaction of Atomic Particles with Spherical Metal Clusters

Natalia Koval

Thesis supervisors:

Ricardo Díez Muiño

Daniel Sánchez-Portal

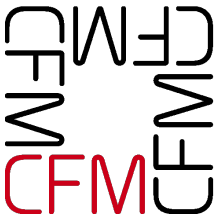

Donostia - San Sebastián, 2016

Acknowledgements

It is a pleasure for me to thank all people whose help and support made this thesis possible.

First of all I would like to express my gratitude to Dr. Ricardo Díez Muiño and Dr. Daniel Sánchez-Portal, my research supervisors, for their continuous support, encouragement and professional guidance. Thank you for being always enthusiastic about our work and for the opportunity to learn a lot from you in the area of dynamics of charges in matter and physics in general. I am particularly grateful to Daniel and Ricardo for careful reading of the manuscript of this thesis and for their valuable comments. Finally, my sincere appreciation to both of them for always understanding my kids-related issues. It has been a great pleasure to be a part of your team!

My special thanks to Dr. Andrey Borissov, our collaborator, for sharing his computational codes (without which this work would not be possible) and brilliant ideas with us and for his help and assistance which contributed significantly to the advancement of this project.

I wish to thank Prof. Pedro Luis Grande for the collaboration which led to an interesting work.

I am grateful to Prof. Pedro Miguel Echenique, whose lectures about what does it mean to be a scientist were very important for me at my first steps in science.

I wish to acknowledge the financial support from Consejo Superior de Inestigaciones Científicas (CSIC) through the Materials Physics Center (MPC/CFM) and from the Donostia International Physics Center (DIPC).

Many thanks to the administrative and computational staff both at DIPC and at CFM, Bélen Isla, Txomin Romero, Iñigo Aldazabal, Garbine Egana, Ana López de Goicoechea, and Amaya Moral for always helping me to resolve my

problems.

I would like to thank my present and former office-mates for sharing their experiences and for friendly atmosphere in our room. Giuseppe Foti, Itziar Goikoetxea, Afaf El Said, Eneko Malatsetxebarria, Mohamed Nosir, Oihana Galparsoro, Ivor Lončarić, Alba Pascual, Flavio Matias, it was great to meet all of you!

I wish to thank my friends, Liubov Aguilova, Oksana Sukhostavets, Stepan and Olga Tsirkin, for always being there for me during the good and the bad.

My heartfelt gratitude to my family and friends in Russia for supporting and encouraging me even being so far. Especially to my mom for always believing in me.

Finally, the most important and difficult part, because there are no enough words to express how grateful I am to my dear husband Peter. Without his encouragement I would not even start my scientific career. Besides the constant love and support he is always my teacher and an example of passionate and talented scientist. This thesis is dedicated to Peter and to our children, Eugeny and Eva.

Abstract

In this thesis we apply time-dependent density functional theory (TDDFT) to study nonadiabatic phenomena in the interaction of charged particles, atoms, and molecules with spherical metallic clusters. These phenomena include the screening processes of projectiles in matter as well as the energy loss processes in a broad range of projectile velocities. In this thesis we focus on two related topics.

The first part, described in Chapter 4, is devoted to the study of the coupled dynamic screening of a localized hole and a photoelectron emitted from a metal cluster or from an adsorbate on the surface of the cluster using a semi-classical model. The motion of the photoelectron is represented classically, while the electronic density dynamics in the cluster is calculated with TDDFT. We calculate the energy loss of the photoemitted electron moving away from the cluster with different velocities. As a result we see that the dynamic screening of the hole by the cluster electrons affects the motion of the photoemitted electron, namely it gives rise to a significant reduction of the energy lost by the photoelectron.

In the second part we present the study of energy loss processes in the interaction of antiprotons and protons, as well as hydrogen dimers, with spherical clusters. In Chapter 5 we investigate how the stopping power for the projectile as a function of velocity can change depending on initial conditions such as the initial state of the cluster (ground or excited state) and the presence of another particle in close proximity to the moving projectile (so-called vicinage effect). First, we calculate the energy loss for an antiproton colliding with a small Al cluster, both when the cluster is initially in the ground state and in an excited electronic state created by a previous collision. We show that the antiproton loses less energy when penetrating a cluster previously excited. We show as well that the projectile creates a plasmon in the cluster and that the energy of the plasmon peak shifts to higher values in the collision with an excited cluster. This shift is

mostly related to the small, positive charge-state in which the cluster is left after the first collision.

In addition, we study the vicinage effect in the energy loss of two antiprotons moving at different distances from each other through the metal cluster. We stress the importance of the plasmon excitation in the cluster, which influences the motion of the trailing antiproton. The vicinage effect is studied for a hydrogen dimer as well. We calculate the stopping power ratio for a large number of projectile velocities and orientations of the dimer axis with respect to the translational velocity. The results of our calculations are in good agreement with recent experimental information from the group of Prof. P. L. Grande in Federal University of Rio Grande do Sul, with whom we have established a collaboration to study this phenomenon.

Chapter 6 is devoted to the study of dissipative effects in the particle-cluster interaction from a different perspective. We calculate the friction force experienced by an antiproton approaching the surface of a metal cluster. Our aim is to establish whether or not it is possible to define a friction coefficient meaningfully. We find that this is indeed the case in the low velocity limit. We show that the friction coefficient does not strongly depend on the projectile velocity, but strongly depends on the distance between the particle and the cluster surface, as well as more weakly on the direction of motion of the projectile (whether it enters or moves away from the cluster).

Contents

Chapter 1

Introduction

The understanding of phenomena taking place when charged particles penetrate solid media is of immense importance for fundamental research as well as for applied physics. The slowing down of charged particles in matter is a key phenomenon in many experimental techniques. Electronic structure and properties of solids, surfaces and nanostructures are experimentally studied by different spectroscopic techniques. In such experiments the material to study is usually probed by incident particles such as electrons (electron energy loss spectroscopy, EELS), photons (photoemission spectroscopy, PES), or ions (ion scattering, IS). Projectiles penetrating the solid or the surface create electronic excitations in the target material. The quantitative description of the dynamics of the probe particles at surfaces and in solids, as well as of the electron dynamics in the excited target, is essential for the correct interpretation of the results of these experiments.

This thesis is devoted to the study of electron dynamics during the interaction of charged and neutral particles with spherical metallic clusters. We focus on nonadiabatic effects, i.e., the effects associated with the dissipation of energy, which means here the transfer of kinetic energy of a moving projectile to electron excitations in the target (metal cluster) or vice versa. In general, we study the dissipative processes that accompany such physical phenomena as the screening and stopping of electrons during photoemission, the screening and stopping of ions and molecules traversing metal clusters and the electronic friction at metallic surfaces. The investigation of such processes allows us to get information about the properties of both the target and the projectile.

The complexity of electronic dynamic processes in solids is a challenge for theoretical methods. In this thesis we study the interaction of metallic clusters

with moving particles using an efficient methodology based on **Time-Dependent Density Functional Theory** (TDDFT), an *ab initio* quantum-mechanical method that allows us to study the dynamical processes taking place during the interaction of probe particles with matter over a large range of velocities of the projectiles. More precisely, we use for the implementation of TDDFT the real-time **Wave Packet Propagation** (WPP) method, an efficient tool for the treatment of the dynamical processes in time domain. The particular WPP code we use in this work was developed by Dr. Andrey Borissov [1, 2] and has been successfully applied to study the dynamic screening of charges in finite-size systems [3, 4] and to the calculation of the energy transfer between particles and small gas-phase clusters [5, 6]. In this work we focus on further investigation of more complex processes using the WPP methodology.

1.1 Metal clusters

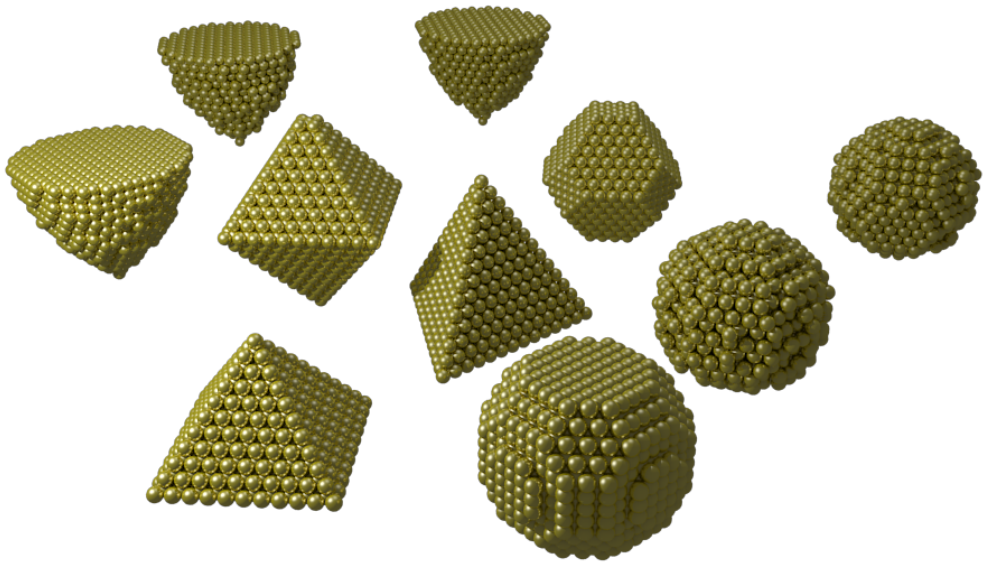

Figure 1.1: Metal clusters [7].

The choice of metals as target materials is motivated, among other reasons, by their catalytic and plasmonic properties. Nano-sized (1 nm = 10^{-9} m) metal clusters (Fig. 1.1) deserve special attention being the main objects of the modern *nanocatalysis* and *nanoplasmonics* research fields.

The importance of catalysis in industry is difficult to overestimate. A *catalyst*

is a substance that accelerates the rate of a chemical reaction, but is unchanged itself by the reaction. Nanocatalysis is a new field in which the nanomaterials are used as catalysts. Nanoparticles have advantages in comparison with ordinary catalysts, because of their high activity at low temperature and stability. The high activity of nanoparticles is due to their large surface-to-volume ratio, since catalytic reactions take place at the surface. By modifying the size and the shape of the nanoparticles it is possible to control their efficiency as catalysts [8].

Another subfield of nanoscience in which metal nanoparticles are of great interest is nanoplasmonics. Nanoplasmonics deals with the optical properties of metal nanoparticles, or, in other words, the control of light at the nanoscale. A remarkable property of metallic nanoparticles is the confinement of light at the nanoscale due to the existence of modes called *surface plasmons*. Surface plasmons are collective electronic excitations at the surface of small metal particles, which enhance the absorption and emission of light at their resonance frequency. Furthermore, they have the ability to localize and enhance light in the proximity of the surface of nanostructures (localizing the electromagnetic field down to the nanometer scale). There are plenty of possible applications of plasmonic nanoparticles such as nanoantennas[9, 10], photovoltaics[11, 12], photocatalysts[13, 14], optical elements, integrated chips, and sensors[15, 16].

The large amount of possible applications of metal clusters has stimulated many theoretical studies of the electronic properties of these objects. The interest in the study of clusters grew significantly after it became possible to produce clusters of various compositions by the laser vaporization technique [17]. It is not only their practical relevance that makes nanoclusters interesting objects to study, but also the fact that they provide a bridge between molecules and solids. By changing the size of a cluster it is possible to change its properties, which helps to understand some of the key concepts in materials physics, chemistry, biology, and medicine. Thus, clusters not only represent a bridge between phases, but also between disciplines [18].

Physics of metal clusters in its modern sense emerged relatively recently – in the 1980's, when it was discovered that atoms of some alkali and noble metals can form systems with an important feature unknown before. The pioneering experiments by W. D. Knight *et al.* [19] showed that metal clusters have an electronic shell structure. The mass spectra of sodium clusters, obtained by W. D. Knight, is shown in the upper panel of Fig. 1.2. Peaks corresponding to a

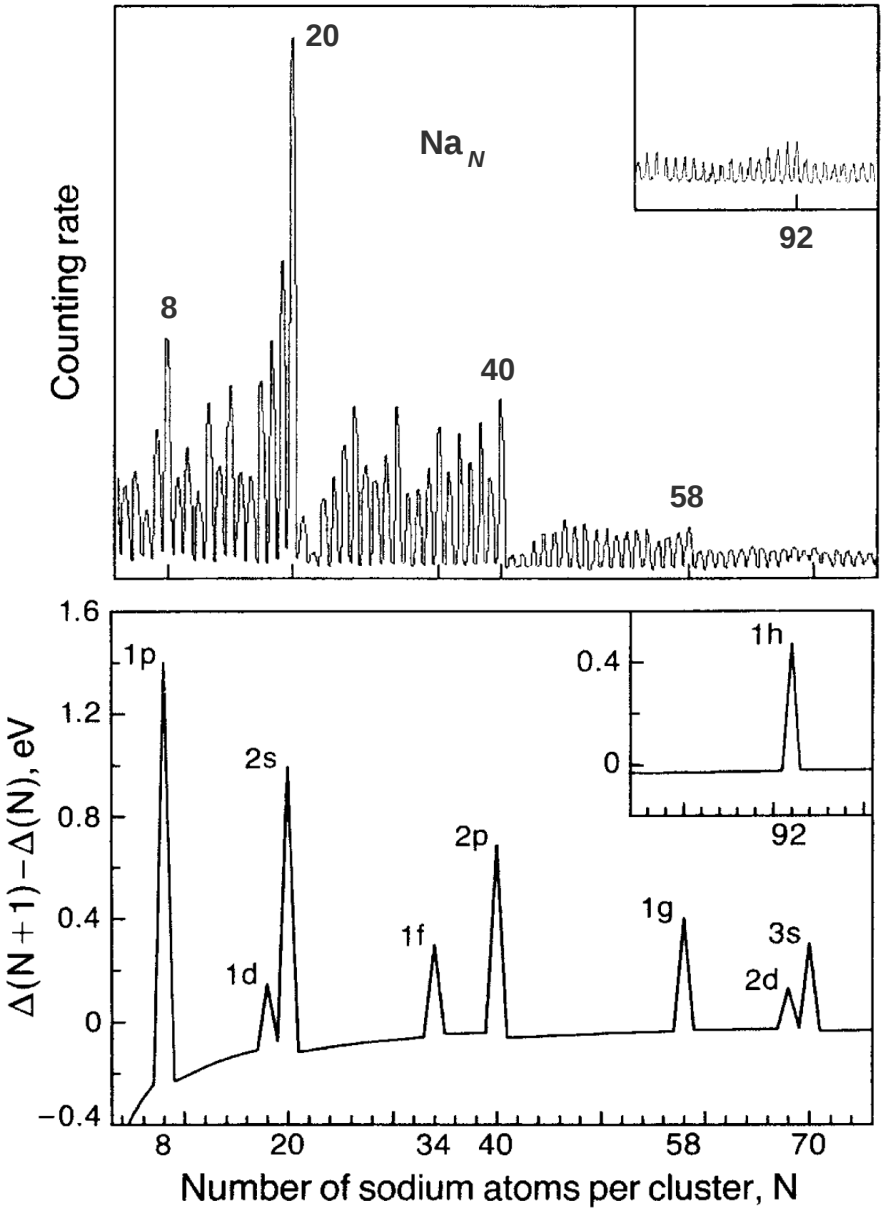

Figure 1.2: Upper panel: mass spectrum of sodium clusters; lower panel: change in electronic energy difference calculated with Jellium model [19].

number of atoms per cluster equal to $N = 8,\ 20,\ 40,\ 58$, and 92 are appreciably large. Points at which these peaks occur have been termed *magic numbers*. Magic numbers indicate especially stable clusters.

Practically at the same time the existence of electronic shells in metal clusters was independently predicted by W. Ekardt [20] using the **jellium model** (JM). After this important discovery, the electronic shell structure was observed in

various alkali and noble metal clusters. The features of the mass spectra are well reproduced by the JM calculations (lower panel of Fig. 1.2), in which the ions are replaced by a uniform positive charge. In clusters with the number of electrons corresponding to magic numbers, the shells are completely filled with electrons, i.e., these clusters have a closed-shell structure, which is more stable. In all the studies presented in this thesis metal clusters are represented in the framework of the spherical jellium model (SJM). A great number of papers have shown that a self-consistent jellium model is able to reproduce qualitatively, and in some cases also quantitatively, many properties of metal clusters observed experimentally [20–22].

In this thesis we focus on two general topics: photoemission and energy loss. The type of processes studied and the methodology used are similar in both cases. Although we study only finite size systems as targets, some of our conclusions are expected to remain valid in extended systems such as metal surfaces or solids. The introduction to both topics follows.

1.2 Photoemission

The first topic, described in Chapter 4 of the present thesis, is related to photoemission. Photoemission, or the *photoelectric effect* (Fig. 1.3), is the emission of electrons from a target following the absorption of photons. It was discovered more than 100 years ago by H. Hertz. Later, in 1905, Albert Einstein explained this effect as a quantum phenomenon. Nowadays, photoemission-based techniques (photoemission spectroscopy (PS), angle-resolved photoemission spectroscopy (ARPES)) are among the most important techniques used to study the structure of molecules, surfaces and solids [23]. In this technique an analyzer (Fig. 1.3) is used to measure the kinetic energy of the photoemitted electrons. The photoemission spectrum, as a result of such experiment, depicts the valence or the core-level binding energies of electrons in the sample, depending on the energy of incoming photons (UV or X-ray) [24]. This allows to analyze the composition of the target material, the electronic properties, and the chemical state of the material.

In photoemission studies nanoclusters are interesting objects for two reasons: first, because if clusters are sufficiently large, they reproduce bulk properties of

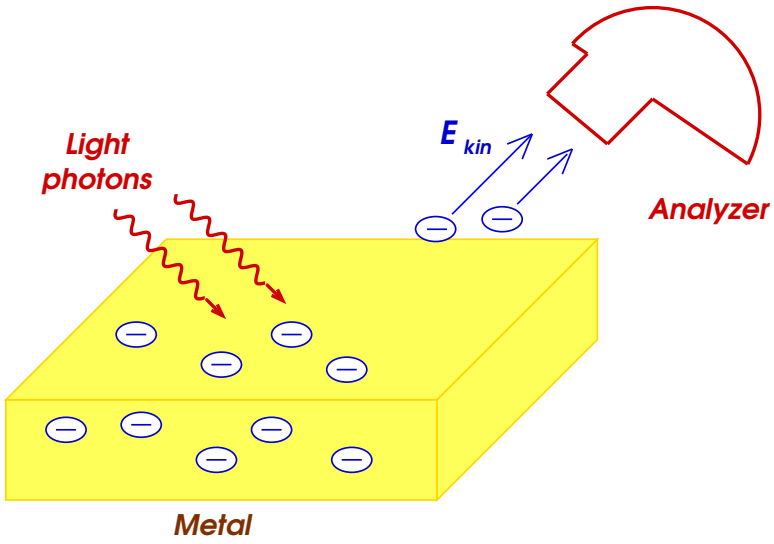

Figure 1.3: Photoemission spectroscopy.

the metal; and second, due to the fact that nanoclusters are better photoemitters than solids. Studies of photoemission from small metal particles from the early 1980's [25] have shown that the yield of photoelectrons per unit incident photon is significantly enhanced if the size of the emitter is less than ten nanometers.

The particular problem of the dynamic screening during photoemission, considered in this thesis, is a subject of interest since the 1970's [26, 27] and is still studied nowadays [28], in particular for jellium clusters [29]. At the beginning of the photoemission process, when the core-hole is created, the screening plays an important role in the electron dynamics of the system. How this screening dynamics affects the movement of the photoemitted electron is a question we pose in our work.

In recent years, progress in laser technology has made it possible the development of photoemission spectroscopy in the attosecond range (1 as $= 10^{-18}$ s) [30]. Attosecond techniques permit access to the time scale of the electronic motion in atoms, molecules, and solids. Due to this experimental advance, there is a growing interest in the theoretical description of the dynamical electronic processes taking place in the subfemtosecond time scale [31–34].

In Chapter 4 we study the dynamic screening and the energy loss of an electron photoemitted from a metal cluster as well as the screening of a localized hole left behind. We also study the case of photoemission from an adsorbate on the surface of a metal cluster. In this case, besides the screening and energy loss processes, we analyze the charge transfer from the metal substrate to the adsor-

bate. We consider the case where one of the atoms in the metallic cluster (or the adsorbed atom) undergoes core-electron photoemission. We study the combined dynamic screening of the static localized core-hole and of the photoemitted electron. We investigate how the presence of the hole affects the many-body electronic dynamics in the cluster and the emission dynamics of the photoelectron.

1.3 Energy loss processes

The second topic, described in Chapter 5 and Chapter 6 of this thesis, is related to the energy loss processes and the dissipative effects in the interaction of antiprotons and protons, as well as their dimers, with metal clusters of different sizes. A charged particle moving across a metallic target is able to create electronic excitations in the medium at the expense of its own kinetic energy. Research on this phenomenon has been broad in condensed matter physics and materials science because of its relevance in various fundamental and applied topics, such as radiation damage, medical physics, and ion sputtering.

A key point in the theoretical analysis of the slowing down of charged particles in metals is the intensity of the perturbation that the moving particle introduces in the medium. For a particle of charge Q moving with a velocity v in a standard metal, the perturbation strength can be roughly characterized by the Sommerfeld parameter $\eta = Q/v$ [35]. If such ratio is small, $\eta << 1$, linear theory can be applied and accurate results for the particle energy loss are usually found. If $\eta >> 1$, the charged particle represents a strong perturbation to the target metal. In such cases one needs to go beyond a perturbative approach in the description of the particle energy loss. Various non-perturbative methodologies have been developed over the years to calculate the energy loss in the limit of low velocities. One of the most successful is the use of scattering theory for target electrons at the Fermi energy, in combination with the self-consistent calculation of the screened scattering potential using static Density Functional Theory (DFT) [36, 37]. In between these two cases, in the regime of intermediate velocities, accurate descriptions of the energy loss process are much more involved because quasistatic or perturbative approximations break down even for unit-charge projectiles. Only recently calculations based on time-dependent density functional theory (TDDFT) [5, 6, 38–44] have shown its potential to close this gap.

Chapter 5 is devoted to the study of the energy loss of antiprotons and protons traversing different metallic clusters. In Section 5.1 we present the study of the energy loss of antiprotons colliding with small aluminum clusters in ground and excited states. We investigate how the energy loss of the projectile is affected by the initial electronic state of the target. The experimental investigation of the excitation and ionization of neutral metal clusters by collision with positively or negatively charged particles has been intensive. In particular, the ionization of metal clusters by low energy singly and multiply charged ions and protons [45, 46] and the ionization of neutral metal clusters by slow electrons [47–50] have been studied. Description of such processes from the theoretical point of view is incomplete and requires further investigation.

In Section 5.2 we explore how the energy loss of an antiproton is changed by the presence of another antiproton in close proximity to the first one. The difference between the energy loss of a single particle interacting with a solid and the energy loss of two particles, traveling in close proximity to each other, is called the *vicinage effect*. The vicinage effect was experimentally quantified for the first time by Brandt *et al* [51] and has been extensively studied since then both experimentally and theoretically (see [52] and references therein for earlier works and [53–60] for recent works). In this thesis we present the first TDDFT study of the vicinage effect in the interaction of two charges moving through metallic media. The large spherical Na and Al clusters are considered as targets and the massive negative particles are chosen as projectiles. We provide a systematic study of the vicinage effect in the energy loss of two antiprotons in metals for a wide range of distances between the incident particles.

In Section 5.3 we present a study of the vicinage effect in the interaction of a hydrogen dimer, H_2, with spherical nanoclusters of high densities, corresponding to the effective densities of Al, Ti and Si oxides. In this case we investigate the vicinage effect as a function of the projectile kinetic energy and compare our results with experimental findings [61].

Chapter 6 is devoted to the study of the dissipative effects in the interaction of antiprotons with metallic surfaces. Namely, we calculate the dissipative part of the force acting on the projectile approaching the surface of the metal cluster due to the creation of electronic excitations (electron-hole pairs). For low projectile velocities (below the Fermi velocity of the target electrons) the dissipative force is just the friction force, which is usually considered to depend linearly on velocity

for extended metallic systems. Thus, we can define the friction coefficient. The knowledge of the friction coefficient is important, for instance, in surface science, where there is dissipation of energy during adsorption or dissociation of atoms and molecules at metal surfaces. A recent proposal in surface science was the calculation of the friction coefficient thought the so-called *Local Density Friction Approximation* (LDFA) [62, 63]. In LDFA the friction coefficient for a projectile moving in an inhomogeneous system is obtained as the friction coefficient in a homogeneous electron gas with the density equal to the density at a given point of the projectile trajectory. Thus, the LDFA friction coefficient depends locally on the electronic density and does not depend on the details of the projectile trajectory. In this thesis we calculate the friction coefficient for an inhomogeneous system, such as the surface of metallic cluster, using a more sophisticated methodology (TDDFT). We compare our results with the standard LDFA results. We do not limit our study to low velocities and test the validity of the friction coefficient concept for high projectile velocities as well.

Chapter 2

Fundamentals of DFT and TDDFT

2.1 Many-body problem

To describe matter at the nanoscale we need to use quantum mechanics. The fundamental equation of non-relativistic quantum mechanics is the *Schrödinger equation*. The full time-independent Schrödinger equation for the many-body system is:

$$\hat{\mathcal{H}}\Psi_{\mathrm{n}}(\mathbf{R},\mathbf{r}) = \mathcal{E}_{\mathrm{n}}\Psi_{\mathrm{n}}(\mathbf{R},\mathbf{r}), \tag{2.1}$$

where $\mathcal{E}_{\mathrm{n}}$ are the energy eigenvalues and $\Psi_{\mathrm{n}}(\mathbf{R},\mathbf{r})$ are the corresponding eigenstates, or the wave functions of the many-electron and many-nuclei system. The wave function describes the quantum state of a system.

The general Hamiltonian $\hat{\mathcal{H}}$ has the following form [64]:

$$\begin{aligned}\hat{\mathcal{H}} = &-\sum_{I=1}^{P}\frac{1}{2M_I}\nabla_I^2 - \sum_{i=1}^{N}\frac{1}{2}\nabla_i^2 + \frac{1}{2}\sum_{I=1}^{P}\sum_{J\neq I}^{P}\frac{Z_I Z_J}{|\mathbf{R}_I-\mathbf{R}_J|}\\ &+\frac{1}{2}\sum_{i=1}^{N}\sum_{j\neq i}^{N}\frac{1}{|\mathbf{r}_i-\mathbf{r}_j|} - \sum_{I=1}^{P}\sum_{i=1}^{N}\frac{Z_I}{|\mathbf{R}_I-\mathbf{r}_i|},\end{aligned} \tag{2.2}$$

where $\mathbf{R} = \{\mathbf{R}_I, I = 1,...,P\}$ is a set of P nuclear coordinates and $\mathbf{r} = \{\mathbf{r}_i, i = 1,...,N\}$ is a set of N electronic coordinates. M_I and Z_I are the nuclear masses and charges, respectively. Atomic units are used throughout the thesis, with $\hbar = e = m_{\mathrm{e}} = 1$, where $\hbar$ is the reduced Planck constant, m_{e} is the electron mass and e is the electron charge, unless otherwise stated.

The equation (2.1) depends on $3(P+N)$ spatial coordinates and analytically exact solutions are possible only for very simple systems, like the hydrogen atom or the H_2^+ ion. Exact numerical solutions are problematic, since this equation is not separable because of the two-body character of the Coulomb interaction potential. Therefore, exact numerical solutions can be found only for systems with a small number of electrons. However, in practice, for real physical problems, such as the interaction of matter with light or atoms and molecules, one needs a quantitative description of systems with a large number of particles.

The first simplification of the complex Schrödinger equation (2.1) and (2.2) is the so-called *adiabatic approximation*. The idea behind this approximation is based on the fact that the nucleus of an atom is at least 1836 times heavier than the electron. Therefore, under typical conditions, the velocity of the electron is much larger than that of the nucleus and we can consider the nucleus as fixed. The electrons can be considered as instantaneously following the motion of the nuclei, while remaining always in the same stationary state. Since the time scales of the electronic and nuclear motions are at least three orders of magnitude different, the total wave function Ψ can be separated into the electronic and nuclear components:

$$\Psi_{\text{total}}(\mathbf{R},\mathbf{r}) = \Phi_{\text{electronic}}(\mathbf{R},\mathbf{r}) \times \Theta_{\text{nuclear}}(\mathbf{R}). \tag{2.3}$$

Therefore, in the adiabatic approximation, the Schrödinger equation for the electronic wave functions is:

$$\hat{h}_{\text{e}}\Phi_{\text{n}}(\mathbf{R},\mathbf{r}) = \mathcal{E}_{\text{n}}(\mathbf{R})\Phi_{\text{n}}(\mathbf{R},\mathbf{r}), \tag{2.4}$$

with the electronic Hamiltonian

$$\hat{h}_{\text{e}} = \hat{K} + \hat{V}_{\text{ee}} + \hat{V}_{\text{ne}}, \tag{2.5}$$

which consists of three operators: the electronic kinetic energy operator $\hat{K} = -\sum_{i=1}^{N}\frac{1}{2}\nabla_i^2$, the potential energy operator of the electron-electron interaction $\hat{V}_{\text{ee}} = \frac{1}{2}\sum_{i,j,j\neq i}^{N}\frac{1}{|\mathbf{r}_i-\mathbf{r}_j|}$, and the potential energy operator of the electron-nuclear interaction $\hat{V}_{\text{ne}} = -\sum_{I=1}^{P}\sum_{i=1}^{N}\frac{Z_I}{|\mathbf{R}_I-\mathbf{r}_i|}$. The potential $\hat{V}_{\text{ne}} = \hat{V}_{\text{ext}}$ is considered as

an external perturbation to the electrons. In the equation (2.4) nuclear coordinates R enter as parameters. The electronic wave functions $\Phi_{\rm n}(\mathbf{R}, \mathbf{r})$ are solutions of the electronic Schrödinger equation, corresponding to a particular nuclear configuration. The total energy of the system E includes the electronic energy $\mathcal{E}_e$ and the nucleus-nucleus repulsion energy

$$V_{\rm nn} = \frac{1}{2} \sum_{I=1}^{P} \sum_{J \neq I}^{P} \frac{Z_I Z_J}{|\mathbf{R}_I - \mathbf{R}_J|} = \text{const}, \tag{2.6}$$

so that

$$E = \mathcal{E}_{\rm e} + V_{\rm nn}. \tag{2.7}$$

The last term in (2.7) can be added after solving the electronic Schrödinger equation for $\mathcal{E}_{\rm e}$. In (2.7) the quantum corrections due to the dependence of electronic wave functions on nuclear coordinates are neglected, as suggested by Max Born and J. Robert Oppenheimer (1927). Thus the nuclei are treated as classical particles [64].

The adiabatic approximation is only valid for problems where the Hamiltonian evolves slowly in time and the electrons always remain in a given, well-defined state (usually the ground state). It thus ignores the possibility of non-radiative transitions between different energy levels due to the nuclear motion. In order to apply safely the adiabatic approximation, the non-diagonal terms that couple different electronic levels of the system should be small as compared to the energies of the electronic excitations. This condition is not fulfilled in systems with degenerate levels, partially occupied levels at the Fermi energy, or with very small band gaps, e.g., in metals. Thus, the adiabatic approximation should be applied with care in such cases. Perturbations that change with time sufficiently rapidly, such as fast ions traversing matter, can lead to strong electronic excitations in the target and, therefore, these processes require to go beyond the adiabatic approximation. We usually talk of nonadiabatic processes or dynamics to refer to such situations.

The separation of the electronic and nuclear motion significantly simplifies the many-body problem. However, one still has to deal with the electronic wave function $\Phi(\mathbf{r}_1, \mathbf{r}_2, \mathbf{r}_3, ..., \mathbf{r}_N)$, a function of $3N$ coordinates, with N being the number of interacting electrons in the system.

2.2 Hartree-Fock and Thomas-Fermi-Dirac methods

The first attempt to solve the many-electron problem was made by D. R. Hartree in 1928. Hartree proposed to write the many-electron wave function simply as a product of the single-electron wave functions (also called electronic orbitals) of the non-interacting electrons [64]:

$$\Phi(\mathbf{r}) = \prod_{i=1}^{N} \psi_i(\mathbf{r}_i). \tag{2.8}$$

Each electron of the system in this approximation is assumed to move in an average field created by the rest of the electrons. This is the basics of the so called *self-consistent field* approach. Each electronic orbital $\psi_i(\mathbf{r}_i)$ satisfies the one-electron Schrödinger equation

$$(\hat{K} + \hat{V}_{\text{ext}} + \hat{V}_{\text{H}}^i)\ \psi_i(\mathbf{r}) = \epsilon_i\ \psi_i(\mathbf{r}) \tag{2.9}$$

in which the Hamiltonian besides the kinetic energy operator $\hat{K}$ and the potential energy operator due to the nuclei $\hat{V}_{\text{ext}}$ also includes the so-called *Hartree potential*, $\hat{V}_{\text{H}}^i$, due to the average field of the other electrons in the system. The Hartree potential can be obtained from the solution of Poisson's equation [65]:

$$\nabla^2 V_{\text{H}}^i(\mathbf{r}) = 4\pi \sum_{j=1, j\neq i}^{N} |\psi_j(\mathbf{r})|^2, \tag{2.10}$$

and thus is given by the following expression:

$$V_{\text{H}}^i(\mathbf{r}) = \sum_{j\neq i}^{N} \int d\mathbf{r}' \frac{|\psi_j(\mathbf{r}')|^2}{|\mathbf{r} - \mathbf{r}'|}. \tag{2.11}$$

The Hartree approximation significantly simplifies the many-electron problem. However, it is inaccurate since in this approach the electrons are treated as distinguishable particles and any exchange and correlation effects are disregarded.

Considerable improvement to the Hartree approach was made by V. A. Fock in 1930, who required the many-electron wave function to be composed of prop-

erly anti-symmetrized products of one-electron orbitals. This gave rise to the appearance of an additional exchange term in Hartree equation (2.9). The so-called Hartree-Fock approximation gives more accurate energies, comparing to the Hartree method. However, the lack of correlation effects can still lead to significant deviations from the experimental results.

At the same time as Hartree and Fock developed their methods, another two scientists, L. Thomas (1927) and E. Fermi (1928), independently proposed a different approach based on the calculation of the total energy of the electronic system only in terms of the *electronic density* $n(\mathbf{r})$. In the Thomas-Fermi method, the kinetic energy of the system of electrons is approximated as a functional of the density of non-interacting electrons in a homogeneous gas with the density equal to the local density at a given point. The method of Thomas and Fermi did not include exchange and correlation effects among the electrons. This was corrected by P. Dirac in 1930, who formulated for the first time the local approximation for the exchange. The Thomas-Fermi-Dirac (TFD) energy functional for the system of electrons in an external potential $V_{\text{ext}}(\mathbf{r})$ is expressed as [66]:

$$\begin{aligned} E_{\text{TFD}}[n] = \frac{3}{10}(3\pi^2)^{\frac{2}{3}} \int d^3r \; n(\mathbf{r})^{(5/3)} + \int d^3r \; V_{ext}(\mathbf{r}) \; n(\mathbf{r}) \\ -\frac{3}{4}\left(\frac{3}{\pi}\right)^{\frac{1}{3}} \int d^3r \; n(\mathbf{r})^{(4/3)} + \int d^3r \; d^3r' \; \frac{n(\mathbf{r}) \; n(\mathbf{r}')}{|\mathbf{r}-\mathbf{r}'|}. \end{aligned} \tag{2.12}$$

The first term in (2.12) is the kinetic energy in the local approximation, the third term is the local exchange energy and the last term is the Hartree energy. The total ground state energy can be found by minimizing the functional $E_{TFD}[n]$.

The TFD method is much simpler than the full many-body Schrödinger equation and it is an important precursor to **Density Functional Theory** (DFT). However, it is inaccurate because it is based on a too poor approximation for the kinetic energy as well as for the exchange energy. Moreover, it can not properly describe the shell structure of atoms and the bonding of molecules [66].

2.3 Density Functional Theory

The problems of the Hartree and Thomas-Fermi approaches were solved when P. Hohenberg and W. Kohn formulated and proved in 1964 the theorem which is

the basis of the modern DFT.

The Hohenberg-Kohn theorem [67] is split in two parts.

Theorem 1: *The ground state electronic density $n(\mathbf{r})$ of a system of interacting electrons in an external potential $V_{\text{ext}}(\mathbf{r})$ uniquely determines this potential, to within an additive constant.*

Since the density determines the number of electrons N and the external potential $V_{\text{ext}}(\mathbf{r})$, it also determines the ground state wave functions and all the electronic properties of the many-body system through the Schrödinger equation. The external potential $V_{\text{ext}}(\mathbf{r})$ and therefore the total energy are unique functionals of the electronic density $n(\mathbf{r})$:

$$E[n(\mathbf{r})] = \int n(\mathbf{r}) V_{\text{ext}}(\mathbf{r}) d\mathbf{r} + F[n(\mathbf{r})], \tag{2.13}$$

where $F[n(\mathbf{r})]$ is an unknown, but nevertheless universal, functional of the electronic density only.

Theorem 2: *the ground state energy can be obtained variationally: the density that minimizes the total energy is the exact ground state density.*

$$\begin{aligned} E_0 = E[n] =& F[n] + \int n(\mathbf{r}) V_{\text{ext}}(\mathbf{r}) d\mathbf{r} \\ =& K[n] + E_{\text{H}}[n] + E_{\text{xc}}[n] + \int n(\mathbf{r}) V_{\text{ext}}(\mathbf{r}) d\mathbf{r}. \end{aligned} \tag{2.14}$$

Since the universal functional $E[n]$ and the ground state density are unknown, equation (2.14) can not be solved. However, in 1965 W. Kohn and L. J. Sham developed a theoretical approach [68], simplifying the problem. They proposed to replace a many-body problem of interacting electrons by a problem of non-interacting electrons moving in an effective potential $V_{\text{eff}}([n], \mathbf{r})$, like it was earlier proposed by Hartree. The difference from the Hartree method is that the KS effective potential includes the exchange and correlation potential. As the electrons are non-interacting, we can separate the corresponding Schrödinger equation into a system of single-electron equations. These equations are called Kohn-Sham (KS) equations and have the following form:

$$\left\{ -\frac{1}{2}\nabla^2 + V_{\text{eff}}([n], \mathbf{r}) \right\} \psi_i^{\text{KS}}(\mathbf{r}) = \varepsilon_i \psi_i^{\text{KS}}(\mathbf{r}), \tag{2.15}$$

where ε_i are the eigenvalues of the KS equations and ψ_i^{KS} are the one-electron

KS wave functions.

Solving iteratively the self-consistent KS equations (2.15), we can obtain the exact electronic density of the system of interacting electrons (provided V_{eff} is known exactly):

$$n(\mathbf{r}) = \sum_{i=1}^{N} |\psi_i^{\text{KS}}(\mathbf{r})|^2. \tag{2.16}$$

The density is normalized to the total number of electrons in the system, so that

$$\int n(\mathbf{r}) d^3r = N. \tag{2.17}$$

The effective potential in the KS equations (2.15) is composed by three potentials:

$$V_{\text{eff}}([n], \mathbf{r}) = V_{\text{ext}}(\mathbf{r}) + V_{\text{H}}([n], \mathbf{r}) + V_{\text{xc}}([n], \mathbf{r}), \tag{2.18}$$

where $V_{\text{ext}}(\mathbf{r})$ is the external potential in which the electrons move, $V_{\text{xc}}([n], \mathbf{r})$ is the so-called exchange-correlation potential, in which all the many-body effects are included, and $V_{\text{H}}([n], \mathbf{r})$ is the Hartree (or Coulomb) potential, created by the electronic density:

$$V_{\text{H}}([n], \mathbf{r}) = \int d\mathbf{r}' \frac{n(\mathbf{r}')}{|\mathbf{r} - \mathbf{r}'|}. \tag{2.19}$$

The exchange-correlation potential and the corresponding exchange-correlation energy are the only unknown functionals in KS approach. By definition, the exchange-correlation potential is the functional derivative of the exchange-correlation energy E_{xc} with respect to the density $n(\mathbf{r})$:

$$V_{\text{xc}}(\mathbf{r}) = \frac{\delta E_{\text{xc}}[n]}{\delta n(\mathbf{r})}. \tag{2.20}$$

The exchange-correlation potential includes the modification of the interaction between electrons in a system due to Pauli exclusion principle (exchange), as well as corrections due to Coulomb interactions. If the functional $E_{\text{xc}}[n]$ would be known exactly, the KS equations would give the exact ground state energy of the many-body system. The search for an accurate $E_{\text{xc}}[n]$ is the main challenge in DFT. There are different approximations for this functional, but in this thesis we use the *local-density approximation* (LDA). LDA was first formulated by Kohn and Sham in 1965 [68]. This approximation is accurate for systems where the charge density is slowly varying, like the free-electron-like metal clusters consid-

ered in this work. In LDA the density functional of exchange-correlation energy is defined as

$$E_{\rm xc}^{LDA}[n] = \int n(\mathbf{r})\varepsilon_{\rm xc}[n]d\mathbf{r}, \tag{2.21}$$

where $\varepsilon_{\rm xc}[n]$ indicates the exchange-correlation energy per particle of a uniform electron gas of density n. The corresponding exchange-correlation potential becomes

$$V_{\rm xc}^{\rm LDA}(\mathbf{r}) = \frac{\delta E_{\rm xc}^{\rm LDA}[n]}{\delta n(\mathbf{r})} = \varepsilon_{\rm xc}(n(\mathbf{r})) + n(\mathbf{r})\frac{\delta\varepsilon_{\rm xc}(n)}{\delta n} \tag{2.22}$$

and the KS equations then read

$$\left\{-\frac{1}{2}\nabla^2 + V_{\rm ext}(\mathbf{r}) + \int d\mathbf{r}'\frac{n(\mathbf{r}')}{|\mathbf{r}-\mathbf{r}'|} + V_{\rm xc}^{\rm LDA}(\mathbf{r})\right\}\psi_i^{\rm KS}(\mathbf{r}) = \varepsilon_i\psi_i^{\rm KS}(\mathbf{r}). \tag{2.23}$$

Solving these equations we can obtain the density (2.16) and the total ground state energy of the system given by (2.14) with the KS kinetic energy

$$K_{\rm s}[n] = \langle\psi_i^{\rm KS}|\sum_i -\frac{1}{2}\nabla_i^2|\psi_i^{\rm KS}\rangle = \sum_i \varepsilon_i - \int V_{\rm eff}([n],\mathbf{r})n(\mathbf{r})d\mathbf{r}. \tag{2.24}$$

The KS kinetic energy $K_{\rm s}[n]$ is the kinetic energy of the system of non-interacting electrons and is different from the K of the system of interacting electrons. This difference should be taken into account and is also included in the exchange-correlation energy $E_{\rm xc}$.

Although the LDA is the simplest approximation, it is sufficiently accurate in many situations and is widely used. It works reasonably well in large clusters of simple metals, such as the ones used in this thesis.

2.4 Time-Dependent Density Functional Theory

TDDFT extends the basic ideas of the ground-state DFT to the treatment of excitations or more general time-dependent phenomena. TDDFT is based on the Runge-Gross (RG) theorem [69], the time-dependent analogue of the Hohenberg-Kohn theorem.

RG Theorem: *for a given initial wave function, there is a one-to-one correspondence between the time-dependent external potential of a system and its time-dependent density.*

In the time-dependent case the one-electron KS equations are

$$\mathrm{i}\frac{\partial}{\partial t}\psi_i^{\mathrm{KS}}(\mathbf{r},t) = \hat{H}_{\mathrm{KS}}\ \psi_i^{\mathrm{KS}}(\mathbf{r},t), \tag{2.25a}$$

$$\hat{H}_{\mathrm{KS}} = -\frac{1}{2}\nabla^2 + V_{\mathrm{eff}}([n],\mathbf{r},t), \tag{2.25b}$$

where $\hat{H}_{\mathrm{KS}}$ is the time-dependent KS Hamiltonian. At time $t = 0$, the wave functions $\psi_i^{\mathrm{KS}}(\mathbf{r}, t = 0) = \psi_i^{\mathrm{KS}}(\mathbf{r})$ are the ground state wave functions. The effective potential consists of three components, in a way similar to the ground state DFT, but in this case all the potentials are time-dependent:

$$V_{\mathrm{eff}}([n],\mathbf{r},t) = V_{\mathrm{ext}}(\mathbf{r},t) + V_{\mathrm{H}}([n],\mathbf{r},t) + V_{\mathrm{xc}}([n],\mathbf{r},t), \tag{2.26}$$

where $V_{\mathrm{ext}}(\mathbf{r},t)$ is the external potential, $V_{\mathrm{H}}([n],\mathbf{r},t)$ is the Hartree potential

$$V_{\mathrm{H}}([n],\mathbf{r},t) = \int d\mathbf{r}'\frac{n(\mathbf{r}',t)}{|\mathbf{r}-\mathbf{r}'|} \tag{2.27}$$

and $V_{\mathrm{xc}}([n],\mathbf{r},t)$ is the exchange-correlation potential, which is again unknown exactly and, as it was mentioned in the previous section, approximations are needed.

We can obtain the charge density of the interacting system from the time-dependent KS (TDKS) orbitals:

$$n(\mathbf{r},t) = \sum_{i=1}^{N} |\psi_i^{\mathrm{KS}}(\mathbf{r},t)|^2. \tag{2.28}$$

To solve TDKS equations various numerical algorithms are used. One of them is the WPP method. We can find the TDKS orbitals $\psi_i^{\mathrm{KS}}(\mathbf{r},t)$ by propagating the initial wave functions $\psi_i^{\mathrm{KS}}(\mathbf{r},t_0)$ in time until some final time t_f. We can rewrite the TDKS equations (2.25) in the integral form:

$$\psi_i^{\mathrm{KS}}(\mathbf{r},t_f) = \hat{U}(t_f,t_0)\psi_i^{\mathrm{KS}}(\mathbf{r},t_0), \tag{2.29}$$

where $\hat{U}$ is the time-evolution operator, a unitary operator, defined as

$$\hat{U}(t',t) = \hat{T}\exp\left[-i\int_t^{t'} d\tau \hat{H}_{\mathrm{KS}}(\tau)\right]. \tag{2.30}$$

Here $\hat{T}$ is the time-ordering propagator. The exponential in (2.30) is very complex and can not be applied directly. Instead, different numerical schemes have been proposed. The total time interval is normally split into smaller intervals of length Δt in order to reduce the error in propagation. There are a few approximations to the time-evolution operator such as, for example, the modified Crank-Nicolson scheme, the split-operator method [70], etc. The detailed description of the propagation method is done in Chapter 3, Section 3.2.

By analogy with the static DFT we use a time-dependent version of LDA in order to calculate the exchange-correlation potential. In TDDFT it is the so-called *adiabatic local-density approximation* (ALDA). Adiabatic means that the potential is local not only in space but also in time. The density at time t is inserted into a static functional, i.e.,

$$V_{\mathrm{xc}}^{\mathrm{ALDA}}[n](\mathbf{r},t) = V_{\mathrm{xc}}^{\mathrm{HEG}}[n(\mathbf{r},t)] = \frac{d}{dn}[n\varepsilon_{\mathrm{xc}}^{HEG}(n)]|_{n=n(\mathbf{r},t)}, \tag{2.31}$$

where $\varepsilon_{\mathrm{xc}}^{HEG}$ is the exchange-correlation energy of the static homogeneous electron gas (HEG) of density $n(\mathbf{r},t)$ [71]. It thus does not include any memory-dependence.

Although it is a simple approximation, the ALDA is the most used approximation in TDDFT calculations and has been proved to work reasonably well in many cases.

Chapter 3

Numerical implementation of DFT and TDDFT

3.1 DFT and Spherical Jellium model for ground state calculations

3.1.1 Spherical Jellium model

We represent metal clusters in the framework of the *Spherical Jellium Model* (SJM) [20, 72–74]. The SJM is a quantum mechanical model in which the ionic structure is completely disregarded. The attractive ionic potential is replaced by a uniform background of positive charge. The SJM can be used to determine the properties of metal clusters with up to several thousands of atoms. Despite the simplicity of this model, it has been successfully applied for the description of the electronic properties of metal clusters and surfaces with weakly bound valence electrons, such as alkali metals. The SJM is a reasonable approximation for electronically closed-shell clusters.

Thus, in the SJM a metal cluster is modelled by a uniform positively charged sphere filled with an electron gas. Electrons move inside the sphere in a featureless external potential, that represents the nuclei and the core electrons. The density of the positive background is defined as

$$n_0^+(\mathbf{r}) = n_0(r_\mathrm{s})\Theta(R_\mathrm{cl} - r), \tag{3.1}$$

where R_{cl} is the radius of the cluster, $\Theta(x)$ is the step-function and $n_0(r_{\mathrm{s}})$ is the constant bulk electronic density, which is a function of only one parameter, the Wigner-Seitz radius (r_{s}) [75]:

$$\frac{1}{n_0} = \frac{4\pi}{3} r_{\mathrm{s}}^3. \tag{3.2}$$

By definition r_{s} is the average radius of a sphere containing one electron in the bulk. This parameter is characteristic for each metal. The number of valence electrons in a neutral cluster is

$$N = \left(\frac{R_{\mathrm{cl}}}{r_{\mathrm{s}}}\right)^3. \tag{3.3}$$

The potential created by the positive background is the integral of the positive density n_0^+:

$$V_{\mathrm{ext}}^+(\mathbf{r}) = -\int d\mathbf{r}' \frac{n_0^+(\mathbf{r}')}{|\mathbf{r}-\mathbf{r}'|}, \tag{3.4}$$

Taking into account equations (3.1) and (3.2), the potential (3.4) has the following form:

$$V_{\mathrm{ext}}^+(\mathbf{r}) = \begin{cases} -\frac{1}{2}\frac{N}{R_{\mathrm{cl}}}\left(3 - \frac{r^2}{R_{\mathrm{cl}}^2}\right), & r < R_{\mathrm{cl}} \\ -\frac{N}{r}, & r \geq R_{\mathrm{cl}} \end{cases} \tag{3.5}$$

With this external potential and using DFT and the KS scheme we calculate the ground state of spherical metallic clusters.

3.1.2 Kohn-Sham scheme

In order to obtain the ground state density of a jellium cluster, we solve the KS equations iteratively. Due to the central symmetry of the problem we use spherical coordinates ($\mathbf{r} = r, \theta, \phi$) in the ground state calculations. The KS orbitals $\Psi^{\mathrm{KS}}(\mathbf{r})$ are represented in a radial grid of equidistant points and are expanded in the spherical harmonics basis set [20]:

$$\Psi_{\mathrm{n,l,m}}^{\mathrm{KS}}(\mathbf{r}) = \frac{1}{r}\psi_{\mathrm{n,l}}^{\mathrm{KS}}(r) Y_{\mathrm{l,m}}(\theta, \phi), \tag{3.6}$$

where n, l and m are the principal, angular and magnetic quantum numbers, respectively. The grid representation of the wave functions makes the results more intuitive and simplifies their analysis. The radial part of the wave function

is multiplied by $1/r$ in order to simplify the wave equation. Since the spherical harmonic functions are known, in order to find the function $\Psi^{\mathrm{KS}}_{\mathrm{n,l,m}}(\mathbf{r})$ we need to solve only radial KS equations for the electronic orbitals $\psi^{\mathrm{KS}}_{\mathrm{n,l}}(r)$:

$$\left[-\frac{1}{2}\frac{\partial^2}{\partial r^2} + \frac{l(l+1)}{2r^2} + V_{\mathrm{eff}}([n], r)\right] \psi^{\mathrm{KS}}_{\mathrm{n,l}}(r) = E_{\mathrm{n,l}}\ \psi^{\mathrm{KS}}_{\mathrm{n,l}}(r), \tag{3.7}$$

$$V_{\mathrm{eff}}([n], r) = V^{+}_{\mathrm{ext}}(r) + V_{\mathrm{H}}(r) + V_{\mathrm{xc}}(r). \tag{3.8}$$

Here $l(l+1)$ comes from the angular part of the Laplace operator in spherical coordinates, which is nothing but the square of the angular momentum operator $\hat{L}^2$. The exchange-correlation potential $V_{\mathrm{xc}}(r)$ is calculated within the LDA approximation using either the Perdew-Zunger parametrization of Ceperley-Alder exchange and correlation potential [76] or Gunnarson-Lundqvist functional [77].

The parameters of the radial grid are the length R, the step Δr and the number of points N_{r} in the grid.

KS equations (3.7) are solved self-consistently by the **diagonalization** of the Hamiltonian matrix. At the first iteration there is an initial guess for the effective potential:

$$V_{\mathrm{eff}}(r) = U\frac{e^{-(r-R_{\mathrm{cl}}-1)}}{1+e^{-(r-R_{\mathrm{cl}}-1)}}, \tag{3.9}$$

where R_{cl} is the radius of the cluster and U is a parameter, which defines the depth of the potential. After each iteration, when the energy eigenvalues $E_{\mathrm{n,l}}$ and wave functions are calculated, the density is obtained as a sum of the squares of the wave functions:

$$n(r) = 2\sum_{(\mathrm{n,l})\in\mathrm{occ}} \frac{2l+1}{r^2}|\psi^{\mathrm{KS}}_{\mathrm{n,l}}(r)|^2, \tag{3.10}$$

where 2 stands for the spin degeneracy and $(2l+1)$ is for the m degeneracy of the electronic energy levels due to the spherical symmetry of the problem. The sum in (3.10) is over the occupied electronic orbitals, for which the eigenvalues are lower than the Fermi level of the system, $E_{\mathrm{n,l}} < E_{\mathrm{F}}$. After calculating the electronic density the effective potential is updated:

$$(V_{\mathrm{eff}}[n])_{\mathrm{new}} = \gamma(V^{+}_{\mathrm{ext}} + V_{\mathrm{H}} + V_{\mathrm{xc}}) + (1-\gamma)(V_{\mathrm{eff}}[n])_{\mathrm{old}}. \tag{3.11}$$

In order to obtain convergence, a *mixing parameter* γ is used in the calculation of the potential. The mixing parameter is a coefficient weighting old and new

potentials at each iteration step. We usually employ values of γ in the range from 0.001 to 0.1. The convergence of the self-consistent calculation is determined by looking at the last occupied eigenvalue (work function). When the calculation is converged the old and new work functions are the same within the predefined accuracy, which in our calculations is equal to 10^{-7}.

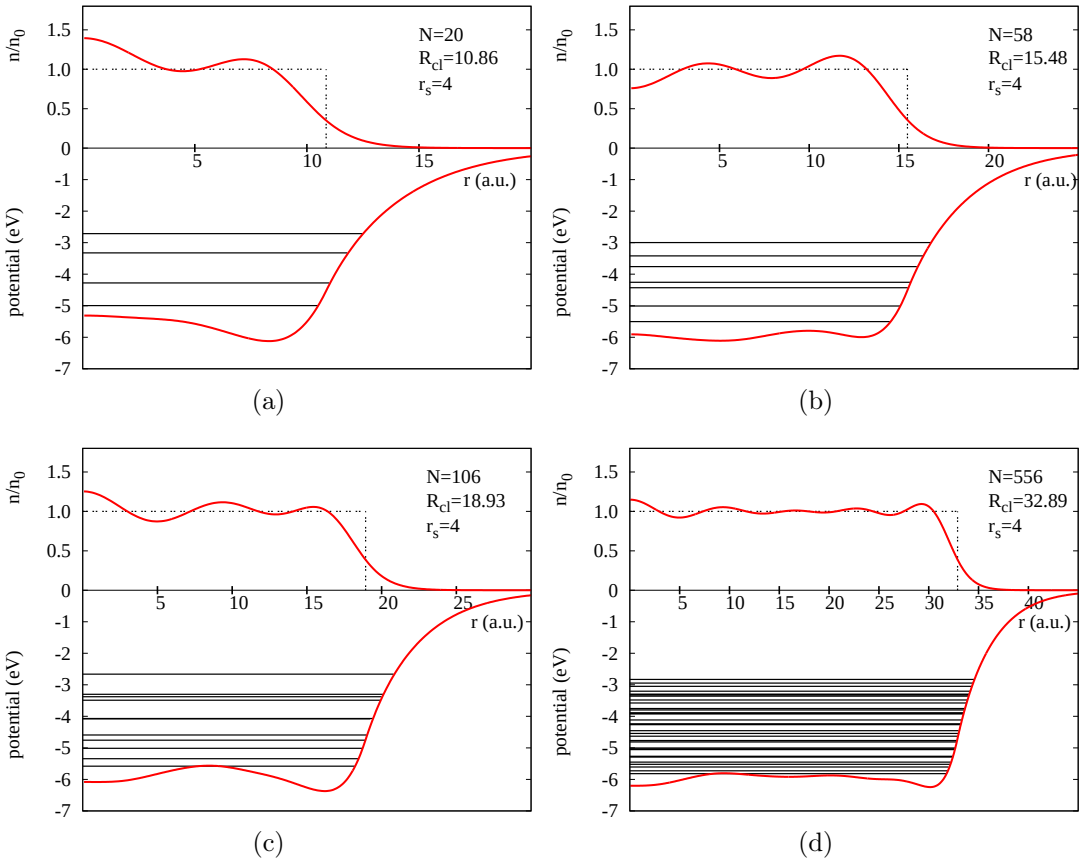

Figure 3.1: Upper part of figures shows the charge density of Na clusters ($r_s = 4$) in units of the background density as a function of radial coordinate. The area limited with dashed lines corresponds to the density of the positive background. Lower part of figures shows the effective potential and the occupied energy levels. a) $N = 20$, b) $N = 58$, c) $N = 106$, d) $N = 556$, where N is the number of electrons in the cluster.

After the calculation is converged, the ground state density of the cluster and the effective potential are obtained. Results for the ground state of small metal clusters have been thoroughly discussed in the literature [19, 20, 22]. In Fig. 3.1 we show the ground state electronic density and the total potential for Na clusters with 20, 58, 106 and 556 electrons.

As it is seen from Fig. 3.1, the electronic energy levels of small clusters are well separated and look similar to atomic energy levels. For this reason, such small clusters are frequently referred to as "artificial atoms". As the size of the cluster increases, the energy difference between the levels decreases. In the Na_{556} cluster, the energy levels show almost a continuum of states (once the finite lifetime and associated broadening are taken into account), which is very similar to the bulk metal. Thus, the jellium clusters can serve as a good model for studying both quantum size effects as well as the bulk metallic properties.

The ground state KS wave functions of the system, obtained with DFT, are used as a starting point for the TDDFT calculations, described in detail in the next section.

3.2 Wave packet propagation method

In order to study the interaction of a cluster with a moving projectile we use the WPP method. The WPP method is a powerful tool to evaluate the dynamics of one-electron wave packets in the time-dependent external potential of a moving projectile.

We solve the system of time-dependent KS equations

$$\mathrm{i}\frac{\partial}{\partial t}\psi_i^{\mathrm{KS}}(\mathbf{r},t) = \hat{H}_{\mathrm{KS}}\psi_i^{\mathrm{KS}}(\mathbf{r},t), \tag{3.12}$$

with the KS Hamiltonian

$$\hat{H}_{\mathrm{KS}} = -\frac{1}{2}\nabla^2 + V_{\mathrm{eff}}([n],\mathbf{r},t). \tag{3.13}$$

The effective potential is

$$V_{\mathrm{eff}}([n],\mathbf{r},t) = V_{\mathrm{ext}}^{+}(\mathbf{r}) + V_{\mathrm{H}}([n],\mathbf{r},t) + V_{\mathrm{xc}}([n],\mathbf{r},t) + V_{\mathrm{P}}(\mathbf{r},t) \tag{3.14}$$

and in this case, besides the Hartree $V_{\mathrm{H}}([n],\mathbf{r},t)$, the exchange-correlation $V_{\mathrm{xc}}([n],\mathbf{r},t)$ potentials and the potential of the positive background $V_{\mathrm{ext}}^{+}(\mathbf{r})$ of the cluster, also includes the external potential of the projectile $V_{\mathrm{P}}(\mathbf{r},t)$. The exchange-correlation potential $V_{\mathrm{xc}}([n],\mathbf{r},t)$ is calculated in the standard ALDA with either the Perdew-Zunger parametrization of Ceperley-Alder exchange and correlation potential [76]

or Gunnarson-Lundqvist functional [77].

Initial conditions are given by the KS orbitals of the cluster in the ground state $\psi_i^{\mathrm{KS}}(\mathbf{r}, t_0)$. As it was mentioned in Section 2.4, we can propagate the ground state wave functions in time by using the time-evolution operator. The propagation from time t_0 to final time t_f is done by dividing the total time interval in short time intervals Δt:

$$\psi_i^{\mathrm{KS}}(\mathbf{r}, t + \Delta t) = \psi_i^{\mathrm{KS}}(\mathbf{r}, t) \exp[-\mathrm{i}\hat{H}_{\mathrm{KS}}\Delta t]. \tag{3.15}$$

Depending on the particular problem, we use in our calculations a time step Δt in the range [0.01 - 0.1] a.u.

The time-dependent KS electronic orbitals $\psi_i^{\mathrm{KS}}(\mathbf{r}, t)$ are represented in a two-dimensional grid (ρ, z) in cylindrical coordinates $\mathbf{r} = (\rho, z, \phi)$. Cylindrical coordinates are well adapted to the axial symmetry of the problems considered in this thesis. Due to the symmetry, the angular $\phi-$dependence of the electronic orbitals is trivial for each value of the projection of the angular momentum along the symmetry axis. Thus, the KS orbitals follow the expression:

$$\Psi_i(\rho, z, t) = \psi_i^{\mathrm{KS}}(\rho, z, t)\frac{e^{\mathrm{i}m_i\phi}}{2\pi}, \tag{3.16}$$

where m_i is a magnetic quantum number. The projectile is moving along the $z-$axis and crosses the cluster through the center. Thus the projectile-cluster system is invariant under rotation around the $z-$axis and the projection of the electron angular momentum on the z-axis m is a good quantum number. The $\pm m$ electronic states are degenerate and we only have to calculate states with $m \geqslant 0$.

We can improve the efficiency of the time propagation by expanding more accurately the wave packet in the region where this is more necessary, i.e., close to the center of the cluster. The ρ coordinate is redefined by a change of variables introduced in order to densify the grid close to the origin of coordinates. We use a new variable x, defined from $\rho = f(x)$, where $f(x) = x - b/\sqrt{a}\arctan(x/\sqrt{a})$, where a and b are new parameters, which in our case are equal to 400 and 392 respectively. According to this change of variables, the wave functions are also modified:

$$\Psi_i(x, z, t) = \psi_i^{\mathrm{KS}}(x, z, t)[f(x)f'(x)]^{1/2}, \tag{3.17}$$

where $f'(x) = df/dx$.

The time-evolution operator in our case is

$$\hat{S} = \exp\left[-\mathrm{i}\hat{H}_{\mathrm{KS}}(t)\Delta t\right] = \exp\left[-\mathrm{i}(\hat{K}_{\mathrm{KS}} + \hat{V}_{\mathrm{eff}})\Delta t\right]. \tag{3.18}$$

The real-time propagation is done using the **split-operator method**, separating the kinetic and the potential energy terms. The split-operator method was first introduced by Feit in 1982 [78, 79]. This is one of the most popular methods for time propagation of wave packets and explicitly preserves unitarity. In the split-operator method, the exponential (3.18) is factorized in terms of exponentials containing either the kinetic energy operator, or the potential. Notice that this is an approximation, since these two operators do not commute, i.e., $[\hat{K}_{\mathrm{KS}}, \hat{V}_{\mathrm{eff}}] \neq 0$. In our case, we use the following factorization to approximate the evolution operator:

$$\hat{S} = \exp\left[-\mathrm{i}\frac{\Delta t}{2}\hat{V}_{\mathrm{eff}}\right] \exp\left[-\mathrm{i}\Delta t\hat{K}_{\mathrm{KS}}\right] \exp\left[-\mathrm{i}\frac{\Delta t}{2}\hat{V}_{\mathrm{eff}}\right]. \tag{3.19}$$

The half-step symmetric product of the potential factor allows us to eliminate the error proportional to the commutator $[\hat{K}_{\mathrm{KS}}, \hat{V}_{\mathrm{eff}}]$ [80]. This method allows us to efficiently evaluate each split component in (3.19) in the space in which it is diagonal, i.e., the kinetic energy operator $\hat{K}_{\mathrm{KS}}$ in momentum space and the potential operator $\hat{V}_{\mathrm{eff}}$ in real space.

The kinetic energy operator in cylindrical coordinates is defined as

$$\hat{K}_{\mathrm{KS}} = -\frac{1}{2}\frac{\partial^2}{\partial z^2} - \frac{1}{2\rho}\frac{\partial}{\partial\rho}\rho\frac{\partial}{\partial\rho} + \frac{m_i^2}{2\rho^2}, \tag{3.20}$$

or taking into account the change of variables on ρ:

$$\hat{K}_{\mathrm{KS}} = \underbrace{-\frac{1}{2}\frac{\partial^2}{\partial z^2}}_{\hat{K}_z} \underbrace{-\frac{1}{2}\frac{1}{(ff')^{1/2}}\frac{\partial}{\partial x}\frac{f}{f'}\frac{\partial}{\partial x}\frac{1}{(ff')^{1/2}} + \frac{m_i^2}{2f^2}}_{\hat{K}_\rho} = \hat{K}_z + \hat{K}_\rho(m_i), \tag{3.21}$$

We further separate the action of the kinetic energy operator on the wave functions along z and ρ axes and thus the final form of the time-evolution operator is the following:

$$\hat{S} = \exp\left[-\mathrm{i}\frac{\Delta t}{2}\hat{V}_{\mathrm{eff}}\right] \exp\left[-\mathrm{i}\Delta t\hat{K}_z\right] \exp\left[-\mathrm{i}\Delta t\hat{K}_\rho(m_i)\right] \exp\left[-\mathrm{i}\frac{\Delta t}{2}\hat{V}_{\mathrm{eff}}\right] \tag{3.22}$$

The time-propagation of $\Psi_i(x,z,t)$ is done using (3.22):

$$\Psi_i(x,z,t+\Delta t) = \hat{S}\ \Psi_i(x,z,t). \tag{3.23}$$

The potential energy operator is local in coordinate space and therefore it is applied by the direct product $\exp\left[-\mathrm{i}\frac{\Delta t}{2}\hat{V}_{\text{eff}}\right]\Psi_i(x,z,t)$ at each grid point.

The action of the kinetic energy operator along the $z-$axis can be also calculated locally transforming the wave functions to momentum space. The $\hat{K}_z$ is applied using the **Dynamic Fourier method** [81]. The kinetic energy operator $\hat{K}_z$ in momentum space is just $K(k_i) = k_i^2/2$. Using Fast Fourier Transform (FFT) we transform $\Psi_i(x,z,t)$ to momentum space and multiply directly by $K(k_i)$ at each k_i point. Then the wave functions are transformed back to real space by inverse FFT.

The action of the kinetic energy operator along the $\rho-$axis is calculated in real space. The exponential with the kinetic energy operator $K_\rho(m_i)$ is approximated by means of the Cayley transform [82]:

$$e^{-\mathrm{i}\Delta t K_\rho(m_i)} = \frac{1-\mathrm{i}\frac{\Delta t}{2}K_\rho(m_i)}{1+\mathrm{i}\frac{\Delta t}{2}K_\rho(m_i)} + O(\Delta t^3). \tag{3.24}$$

This transform is unitary and second order accurate. Thus we obtain

$$\left(1-\mathrm{i}\frac{\Delta t}{2}K_\rho(m_i)\right)\Psi_i(x,z,t+\Delta t) = \left(1+\mathrm{i}\frac{\Delta t}{2}K_\rho(m_i)\right)\Psi_i(x,z,t). \tag{3.25}$$

The second derivative with respect to x in K_ρ (Eq.(3.21)) is approximated using finite differences [80, 82]:

$$\frac{\partial}{\partial x}D(x)\frac{\partial \Psi_i}{\partial x} = \frac{D(x_{i+1/2})(\Psi_{i+1}-\Psi_i) - D(x_{i-1/2})(\Psi_i - \Psi_{i-1})}{(\Delta x)^2}, \tag{3.26}$$

where $D(x) = \dfrac{f(x)}{f'(x)}$ and $\Psi_i = \dfrac{1}{(ff')}\Psi_i$. Substituting (3.26) into (3.25) we obtain a system of three-diagonal linear equations connecting $\Psi_i(x,z,t+\Delta t)$ and $\Psi_i(x,z,t)$ at each grid point.

Using Eq.(3.23) we evaluate the KS states in time. The time-dependent electronic density $n(\mathbf{r},t)$ is then calculated at every time step as a sum over occupied

electronic states:

$$n(x,z,t) = s_i \sum_{i\in occ} |\Psi_i(x,z,t)|^2, \tag{3.27}$$

where s_i stands for the spin and m degeneracy ($s_i = 2$ for $m = 0$ and $s_i = 4$ otherwise).

The scheme of the time propagation of the electronic orbitals is thus the following:

1. Read the ground state wave functions of the unperturbed cluster $\psi_i^{\mathrm{KS}}(\mathbf{r}, t_0)$ and the corresponding magnetic quantum numbers m_i from the input file.

2. Transform the ground state wave functions from spherical to cylindrical coordinates and change the variables on ρ, i.e., obtain $\Psi_i(x, z, t_0)$.

3. Calculate the ground state electronic density, Eq.(3.27) and the effective potential, Eq.(3.14).

4. Multiply the wave functions by the exponent of the half-step potential energy operator, $\exp\left[-\mathrm{i}\frac{\Delta t}{2}\hat{V}_{\mathrm{eff}}\right]\Psi_i(x,z,t)$.

5. Transform the wave functions to momentum space by FFT and multiply by $k_i^2/2$.

6. Transform the wave functions back to real space and multiply by the exponent of the $\hat{K}_\rho(m_i)$ using Cayley transform, Eq.(3.25), i.e., solve the system of three-diagonal equations.

7. Again multiply the wave functions by the exponent of the half-step potential energy operator, $\exp\left[-\mathrm{i}\frac{\Delta t}{2}\hat{V}_{\mathrm{eff}}\right]\Psi_i(x,z,t)$.

8. From the wave functions calculate the electronic density at this time step, $n(\mathbf{r}, t)$ (Eq.(3.27)).

9. Recalculate the effective potential from the new density and go back to step 4. The steps 4–9 are repeated every time step of the propagation until the final time t_{f} is reached.

During propagation, we calculate all interesting quantities, such as the total energy of the system, the dipole moment, or the force acting on the projectile.

Chapter 4

Dynamic screening of a localized hole and the emitted electron during photoemission from metal clusters

In this chapter we focus on the study of the dynamic screening and the energy loss of an electron photoemitted from a metal cluster and from an atom adsorbed on the surface of a metal cluster. The problem addressed here has a long history in condensed matter physics. The dynamic relaxation of the Fermi sea after creation of a hole was analyzed in the context of X-ray photoemission by several authors [26, 83]. Within the framework of linear response theory, Noguera *et al.* showed that the effective interaction between the core-hole and the photoemitted electron changes continuously from a statically screened potential for low-energy electrons to a completely unscreened potential for high-energy electrons [26]. They also showed that the double screening of hole and electron can occur with or without creation of plasmons according to the kinetic energy of the emitted electron. In this work we go beyond linear theory in the description of the dynamic screening of charges in the photoemission process by using propagation of electronic wave packets with TDDFT to compute the response of the valence electrons. The main aim of this chapter is to show that the dynamic screening of the core hole can lead to the reduction of the energy loss of the photoemitted electron moving away from the hole.

4.1 Dynamic screening of a localized hole during photoemission from a metal cluster

We use a semi-classical model for the description of the photoemission process. The motion of the photoemitted electron is described classically. This approximation is justified, provided that typical energies of the photons are relatively high, and give rise to high kinetic energies of the photoemitted electrons. In parallel, valence electron dynamics in the cluster is investigated by means of TDDFT.

In our model, we do not consider explicitly the interaction of the metal cluster with the external electromagnetic field. Thus, an electron with high kinetic energy and a static hole are created at $t = 0$ at the center of the spherical cluster. The scheme of the process is shown in Fig. 4.1. The photoemitted electron (el) is

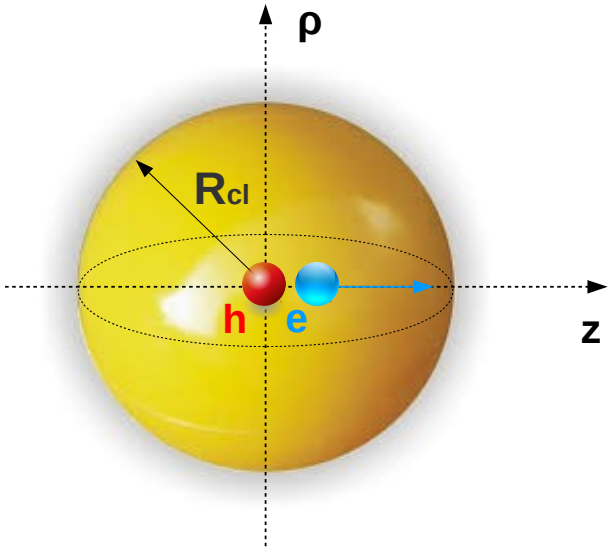

Figure 4.1: Sketch of the photoemission process. An electron and a hole are created at the center of the spherical cluster at $t = 0$. Both are represented by classical point particles and the electron starts to move along the z-axis with velocity v_0.

modeled as a negative point charge that moves along the z-axis $[\rho_{\mathrm{el}} = 0,\ z_{\mathrm{el}}(t)]$. It is worth noting that this photoemitted electron is not one of the cluster valence electrons, but an extra electron coming from the inner shell of a hypothetical atom sited in the center of the cluster. The electron motion is calculated in two different approximations as described in detail below. The hole (h) is represented

by a positive point charge at a fixed position [$\rho_{\rm h} = 0,\ z_{\rm h} = 0$]. The potential created by these charges and acting on the electrons of the cluster is:

$$\triangle V(\rho, z, t) = V_{\rm el}(\rho, z, t) + V_{\rm h}(\rho, z, t), \tag{4.1}$$

where

$$V_{\rm el}(\rho, z, t) = \frac{1}{[(z_{\rm el}(t) - z)^2 + \rho^2]^{1/2}}\Theta(t), \tag{4.2}$$

and

$$V_{\rm h}(\rho, z, t) = -\frac{1}{[z^2 + \rho^2]^{1/2}}\Theta(t). \tag{4.3}$$

The potential $\triangle V(\rho, z, t)$ replaces the external potential of the projectile $V_{\rm P}(\mathbf{r}, t)$ in the system of TDKS equations (3.12)–(3.14). Using the algorithm described in the Section 3.2 we propagate in time the cluster KS wave functions under the perturbation of the static hole and the moving electron. At every time step of the propagation we calculate the time-dependent electronic density (3.27), from which we can calculate the cluster induced force acting on the photoemitted electron along the $z-$axis:

$$F_z^{\rm cls}(t) = 2\pi \int \rho d\rho dz \frac{n(\rho, z, t) - n_0^+(\rho, z)}{[(z_{\rm el} - z)^2 + \rho^2]^{3/2}}(z_{\rm el} - z), \tag{4.4}$$

which also includes the effect of the positive background density (n_0^+).

To address the effect of the many-body dynamics in the cluster on the energy loss experienced by the ejected electron under well-defined conditions, we first study a simplified case in which the photoemitted electron is assumed to move with constant velocity υ, i.e., $z_{\rm el}(t) = \upsilon t$. This allows us to isolate the effects related to the dynamics of the screening processes from other possible effects associated with the details of the trajectory. Here, υ corresponds to the final velocity of the electron if the photoemission process would take place in vacuum, which is considered as a good approximation for the average electron velocity during its movement through the cluster. Thus, the direct interaction between the electron and the hole is not taken into account in this case. However, as we will see below, the screening of the hole still has an important influence on the energy loss by the photoemitted electron. In this case the energy loss is calculated from the integral:

$$E_{\rm loss} = -\upsilon \int_0^\infty F_z^{\rm cls}(t) dt. \tag{4.5}$$

It is important to note that $E_{\rm loss}$ includes the energy necessary to eject the electron from the cluster (an adiabatic contribution), as well as non-adiabatic contributions due to the creation of electronic excitations in the cluster during the emission process.

In a second step, we perform a more refined treatment in which the direct electron-hole interaction is included and the trajectory $z_{\rm el}(t)$ is calculated using the classical equations of motion:

$$dz_{\rm el}/dt = v(t), \qquad z_{\rm el}(t=0) = 0 \tag{4.6}$$

$$dv/dt = F_z^{\rm tot}(t), \qquad v(t=0) = v_0. \tag{4.7}$$

In Eq. (4.7), $F_z^{\rm tot}$ is the total force felt by the moving electron:

$$F_z^{\rm tot}(t) = F_z^{\rm cls}(t) - \frac{z_{\rm el}(t)}{[z_{\rm el}(t)^2 + \alpha^2]^{3/2}}. \tag{4.8}$$

The first term on the right side of Eq.(4.8) corresponds to the interaction with the cluster given by Eq.(4.4). The second term stands for the force due to the interaction between the photoemitted electron and the core hole left behind. The electron-hole interaction in our study is given by the regularized Coulomb potential $V_{\rm el-h}$:

$$V_{\rm el-h} = -\frac{1}{\sqrt{z_{\rm el}(t)^2 + \alpha^2}}, \tag{4.9}$$

We use the cutoff parameter $\alpha^2 = 0.5$ to avoid divergence at time $t = 0$.

The second approximation might be closer to the real photoemission process. In this case we also find an important influence of the hole-screening dynamics on the force experienced by the emitted electron and, thus, on the energy loss during the photoemission process.

4.1.1 Constant velocity approximation

In the constant velocity approximation, we calculate the cluster induced force in two different cases, namely with a localized hole at the center of the cluster (potentials in Eqs. (4.2) and (4.3) are included in the calculations) and without the hole (only the potential in Eq. (4.2) is included). In the first case, the direct

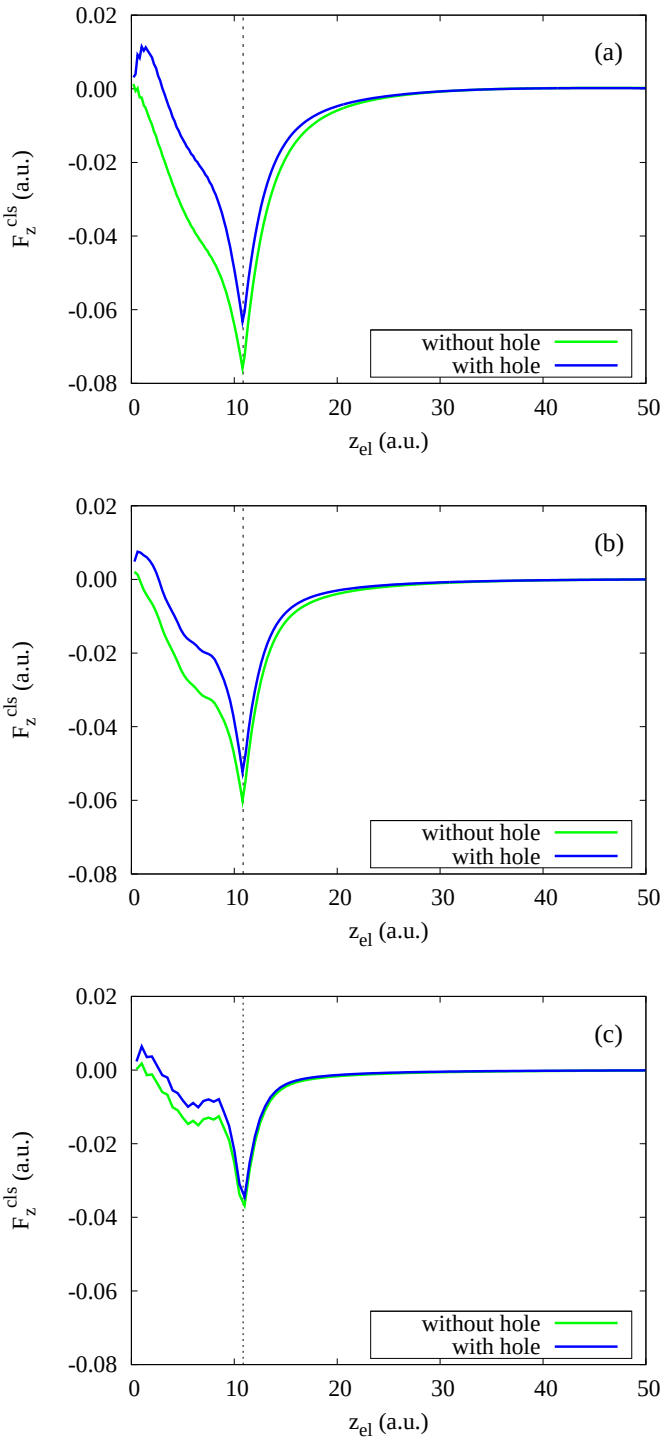

Figure 4.2: Cluster induced force, F_z^{cls}, acting on the electron moving away from the center of the Na_{20} cluster as a function of the electron position. The electron moves with a constant velocity: a) $v = 1$, b) $v = 1.5$, and c) $v = 2.5$. Vertical dashed lines show the border of the cluster.

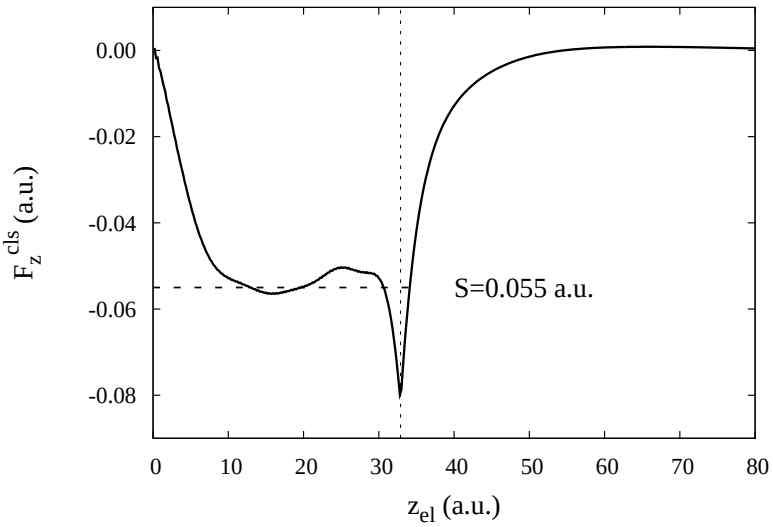

Figure 4.3: Cluster induced force acting on the electron moving away from the center of the Na_{556} cluster as a function of the electron position. The hole is not included. The electron moves with velocity $v = 1$. Horizontal dashed line corresponds to the stopping power in an homogeneous electron gas with r_s=4.

interaction between hole and electron is not included. In spite of this, we find that the presence of the hole modifies the electron dynamics in the cluster because there are two different charges to be screened. We have studied four Na clusters ($r_s = 4$) with 20, 58, 106 and 556 electrons. We consider three different velocities of the photoemitted electron: 1, 1.5 and 2.5 a.u.

Figure 4.2 shows the cluster induced force F_z^{cls} acting on the photoemitted electron as a function of the electron position for all three velocities considered and for the smallest cluster, with 20 electrons. From the present results it follows that, in the case of the presence of the hole, the cluster induced force on the photoemitted electron has positive value at short times. This indicates that the cluster response tends to accelerate the electron at the very beginning of its movement. The repulsive cluster induced force is related to the screening of the hole. More precisely, at the beginning of its movement, when close to the hole, the electron is repelled from the hole vicinity by the cluster electrons that arrive to screen the hole. When the hole is not included in the calculation, the above effect is not observed and the emitted electron is mainly decelerated all along its trajectory. This deceleration is due to two effects. First, within the cluster, the electron suffers the stopping characteristic of any charged particle moving in an electron gas [6]. Second, as the electron approaches the cluster surface, we can clearly see the contribution of the forces associated with overcoming the surface

potential step.

These two decelerating contributions are difficult to disentangle for very small clusters, like that shown in Fig. 4.2. However, the force experienced by a particle moving inside a large jellium cluster reaches a sort of stationary regime and oscillates around a mean value. This can be seen in Fig. 4.3 for a cluster containing 556 electrons. The mean value of the force is similar to the stopping power in an infinite medium, which only depends on the electron density. In our case, for $r_s = 4$, the stopping power is around 0.055 a.u. for a negatively charged particle moving with velocity $v = 1$ a.u. in an infinite electron gas [5].

We can further analyze the influence of the hole screening on the moving electron if we look at the difference of forces (Fig. 4.2): $F_h^{cls}(z) = F_{h,el}^{cls}(z) - F_{el}^{cls}(z)$. Here, $F_{h,el}^{cls}(z)$ (F_{el}^{cls}) is the cluster induced force on the photoemitted electron calculated with (without) explicit inclusion of the positive point charge at the center of the cluster. With this definition, $F_h^{cls}(z)$ is the force felt by the photoemitted electron due specifically to the cloud of electronic density that dynamically screens the hole. This quantity is shown in Fig. 4.4 for all clusters considered and for two different velocities.

As it is seen from the graphs, the effect of the screening of the hole is larger in the case of the smallest electron velocity (Fig. 4.4(a)). This is related to the time that the photoelectron spends in the neighborhood of the hole and to the characteristic time of the hole screening. The slow photoelectron stays near the hole long enough for the screening of the hole to be performed. Therefore, it experiences a large force due to the piling up of electronic charge around the hole. The fast electron, however, leaves the hole at short times, which are not enough for a significant piling up of screening charge. Hence, the effect associated with the hole screening becomes smaller the higher the electron velocity. It is worth noting that, for the slow electron, $F_h^{cls}(z)$ is almost identical for the two largest clusters considered here and it is very small for $z_{el} > 25$. Both observations indicate that the screening of the hole is well established and basically reaches its stationary value at the corresponding time scale. For the faster electron, however, the value of $F_h^{cls}(z)$ at large z_{el} is different for different cluster radii (Fig. 4.4(b)). This is linked to the time-evolution of the screening density which still goes on by the time the electron reaches the cluster boundary. These conclusions are corroborated by the induced electronic density dynamics plots (Fig. 4.6) discussed later on.

In order to quantify the effect of the hole screening, we calculate the electron

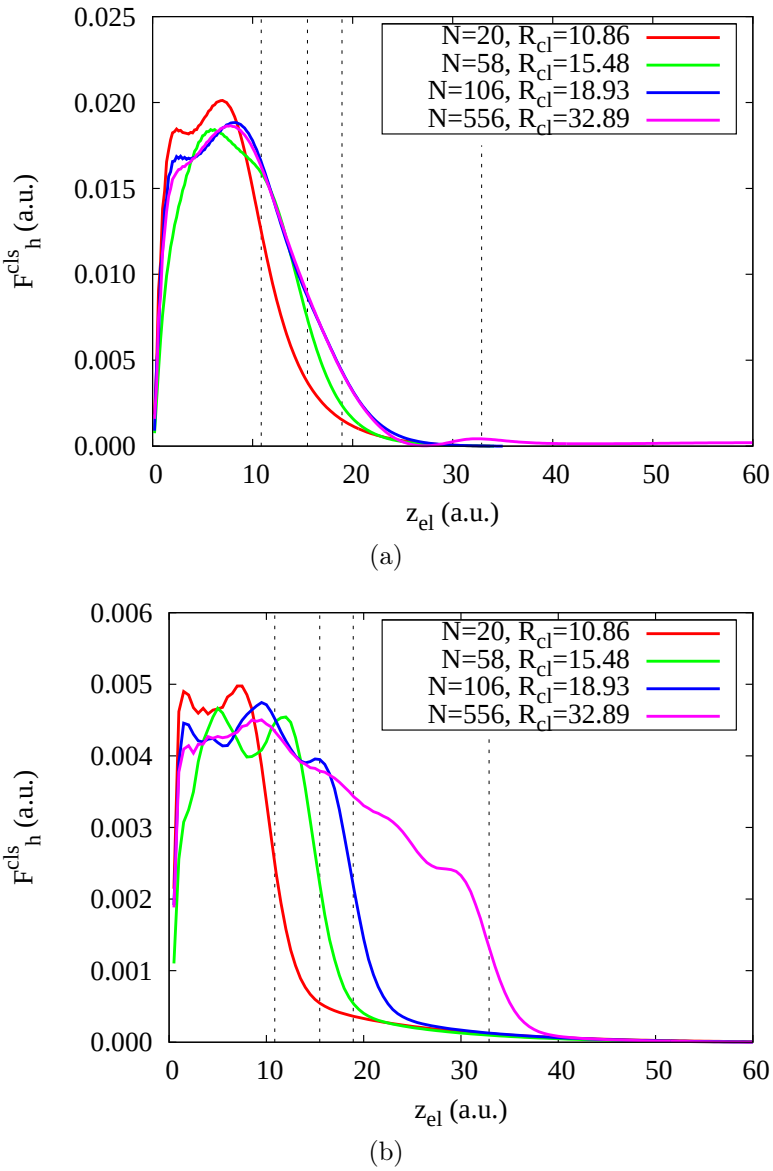

Figure 4.4: Component of the cluster induced force acting on the moving electron due to the dynamic screening of the hole by the electronic charge of the cluster, $F_{\mathrm{h}}^{\mathrm{cls}}(z)$. Results are shown as a function of the electron position for jellium clusters (r_{s}=4) of different size comprising $N = 20,\ 58,\ 106$, and 556 electrons. Electron velocities are: a) $v = 1$, b) $v = 2.5$. Vertical dashed lines correspond to the radii of the clusters.

energy loss due to the interaction with the cluster electrons for the case of $N = 20$ and for the velocities 1, 1.5, and 2.5 of the photoemitted electron. The energy loss E_{loss}, given by Eq. (4.5), is defined as the work performed by the cluster induced force acting on the moving electron. The results are summarized in Table 4.1, in

which the difference in the cluster induced energy loss ΔE_{loss}, with and without the hole, is also shown.

Table 4.1: Energy loss [Eq. (4.5)] of the photoemitted electron as a function of its velocity. The electron is assumed to follow a trajectory with constant velocity. The difference in energy loss ΔE_{loss} for the case of absence and presence of the hole in the center of the cluster is also given.

$N = 20$		$v = 1$ a.u.	$v = 1.5$ a.u.	$v = 2.5$ a.u.
E_{loss}, a.u.	without hole	0.60	0.44	0.22
	with hole	0.37	0.30	0.16
ΔE_{loss}, a.u.		0.23	0.14	0.06

The presence of the hole reduces the cluster induced energy loss for all velocities. The value of ΔE_{loss} also shows that the effect of the hole screening is more significant the slower is the electron. The energy loss of the electron moving with $v = 1$ a.u. decreases almost by a factor of 2 when we include the hole screening in the process. An interesting consequence is that, at low velocities, the effects associated with the hole screening might become crucial to determine if the photoemission process can indeed take place or not. For example, the kinetic energy of the slowest electron considered in Table 4.1 is 0.5 a.u.. Since the energy loss in the case without hole is 0.6 a.u., this electron cannot be photoemitted from the cluster. However, in the presence of the hole the photoemission becomes possible.

The study of the electron dynamics during photoemission in the constant velocity approximation leads us to two conclusions: 1) the screening of the hole by the cluster electrons leads to a repulsive (accelerating) force acting on the photoemitted electron at the beginning of its movement; 2) the effect of the hole screening is reduced for faster (more energetic) photoemitted electrons.

4.1.2 Varying velocity approximation

The results discussed so far are obtained using a simple model in which the photoemitted electron moves with a constant velocity. In a real photoemission process, however, the velocity varies due to the different elastic and inelastic forces acting on the electron. In order to be sure that none of the effects discussed above

is an artifact of the model and to prove our conclusions, we simulate the photoemission process in a more realistic second approximation. In this approximation, the velocity and coordinate of the electron are dependent on time, according to equations (4.6), (4.7), and (4.8). Electron and hole interact via a regularized Coulomb potential (Eq. (4.9)).

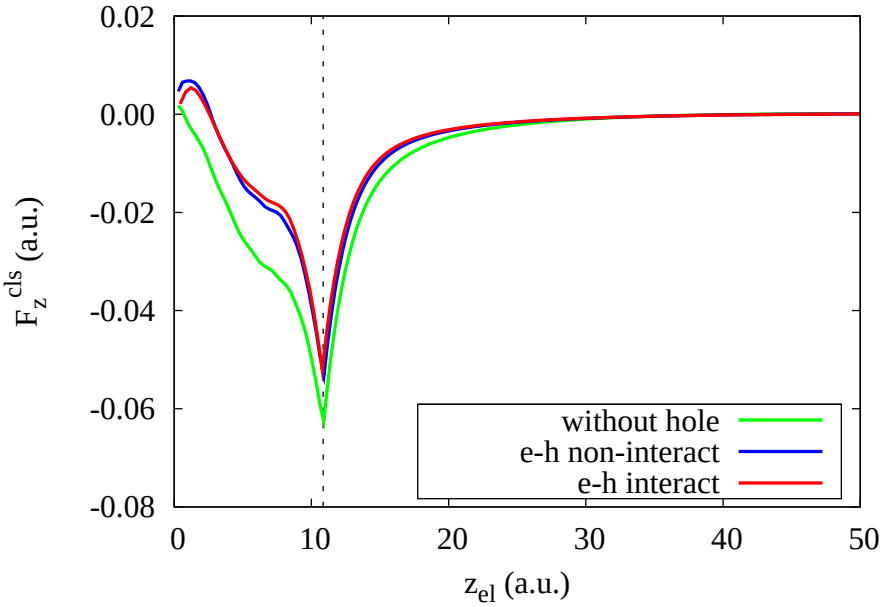

Figure 4.5: Cluster induced force [Eq. (4.4)] acting on the electron moving away from the center of the cluster ($N = 20$, $r_s = 4$), as a function of the electronic position in three cases: 1) There is no hole at the center of the cluster and the initial velocity of the electron is 1.5 a.u. (green line); 2) There is a hole at the center of the cluster, but the photoemitted electron does not interact directly with the hole. The initial velocity of the electron is 1.5 a.u. (blue line); 3) There is a hole at the center of the cluster and a direct electron-hole interaction (Eq. 4.9) is included. The initial velocity of the electron is 2.25 a.u. (red line). The vertical dashed line shows the radius of the cluster, $R_{cl} = 10.86$ a.u.

In Fig. 4.5 we show the results for the small cluster with 20 electrons in the varying velocity approximation. The force felt by the moving electron due to the interaction with the cluster electrons (Eq. (4.4)) is calculated for three different cases. In the first case, we do not include the hole in the cluster. In the second case, there is a hole to be screened, but we do not include the direct interaction between the hole and the photoelectron when performing the trajectory calculation. In the third case, the direct interaction between photoelectron and hole is additionally included. In the first two situations, the initial velocity of the electron is set to 1.5 a.u, while in the third situation is set to 2.25 a.u. This

difference in velocity corresponds to the energy of the electron-hole interaction. Indeed, with the parameter $\alpha^2 = 0.5$, used in Eq. (4.9), the "binding energy" (the interaction energy when both the electron and the hole are located at the center of the cluster) of the electron is around 1.4 a.u. Taking into account this binding energy, the initial velocity 2.25 a.u. for an electron interacting with the hole and eventually photoemitted in vacuum leads to a final velocity ~ 1.5 a.u. Therefore, our choice of initial velocities allows a direct comparison of the two cases, with and without direct electron-hole interaction in the case of photoemission inside the cluster.

We can see from Fig. 4.5 that the behavior of the cluster induced force in this more realistic model is similar to that of the simple model considered in the previous section (Fig. 4.2). Whenever the hole screening is taken into account, there is an accelerating force acting on the electron at the beginning of its trip. Similarly to the constant velocity approximation, performing calculations along a more realistic trajectory with different launch velocities, we also found that the effect of the hole screening decreases when the initial velocity of the electron increases.

Moreover, we found that the cluster induced force is very similar independently on whether electron and hole directly interact with each other or not. However, this is valid only if the final velocity of the photoemitted electron interacting with the hole is equal to the final velocity of the electron not interacting with the hole. This shows that, as far as the final energy of the photoemitted electron is the same, the cluster induced force acting on the photoemitted electron is mainly affected by the presence or absence of the hole screening and not by the details of the electron trajectory nearby the hole.

4.1.3 Time evolution of the electronic density

Continuing the discussion on the electron density dynamics in the cluster, we illustrate the effect of the coupling of both processes – dynamic screening of the hole and dynamic screening of the moving electron. Figure 4.6 shows the time evolution of the electronic density of the spherical cluster with $N = 106$ electrons. The hole and the electron are created at time $t = 0$ at the center of the cluster (z=0) and the electron is moving along the positive part of the z-axis with a constant velocity $v = 1$ a.u. The induced electronic density close to the

z-axis $\Delta n = n(\rho_0, z, t) - n(\rho_0, z, 0)$, where $\rho_0 = 0.02$ a.u, is plotted in units of the background density n_0.

Panel (a) shows the results of a direct TDDFT calculation of the induced electronic density for the cluster with a static hole at the center and a photoelectron moving away from the center of the cluster along the z-axis. Panel (b) shows the induced electronic density obtained as a sum of two different contributions:

$$\Delta n(t) = \delta n_{\mathrm{h}}(t) + \delta n_{\mathrm{el}}(t). \tag{4.10}$$

Here, $\delta n_{\mathrm{h}}(t)$ is the TDDFT result for the induced electron density due to the appearance of only a localized hole at the center of the cluster. Similarly, $\delta n_{\mathrm{el}}(t)$ is the TDDFT result for the induced electron density in response to a photoelectron moving from its center, where no hole is present. Therefore, panel (b) shows a linear superposition of the electronic charges screening the static hole and the moving photoelectron. In the inset of both graphs we show the time evolution of the electronic density at a given point (ρ=0.02 a.u., z=0.2 a.u.).

The white area in the main plots shows a depletion of the electronic density in the cluster that roughly follows the trajectory of the electron. It is due to the Coulomb repulsion between the moving electron and the rest of the electrons in the cluster. Black arrows indicate the time at which the screening of the hole is fully developed, i.e., the induced electron density in the close vicinity of the hole roughly integrates to one. This time is also shown in the inset of each plot and is equal to 11 a.u. and 8 a.u. for the cases (a) and (b), respectively. Thus, there is a delay in the TDDFT screening of the hole as compared to the linear superposition case. Moreover, comparing the charge distribution for negative and positive values of z, we can see that there is an asymmetry in the screening charge for the TDDFT calculation with both hole and electron simultaneously included. This asymmetry is absent in panel (b), corresponding to the linear superposition of electron and hole separate screenings, and clearly indicates that the dynamics of the hole screening is affected by the presence and movement of the emitted electron. Therefore, we can conclude that the TDDFT calculation, considering both the hole at the center and the electron photoemitted from the center of the cluster, includes a combined effect of the dynamic screening of both particles in the relaxation processes in the cluster. This combined effect is also visible in the oscillations of the electronic density, where the periods of these oscillations are slightly different for the two cases considered.

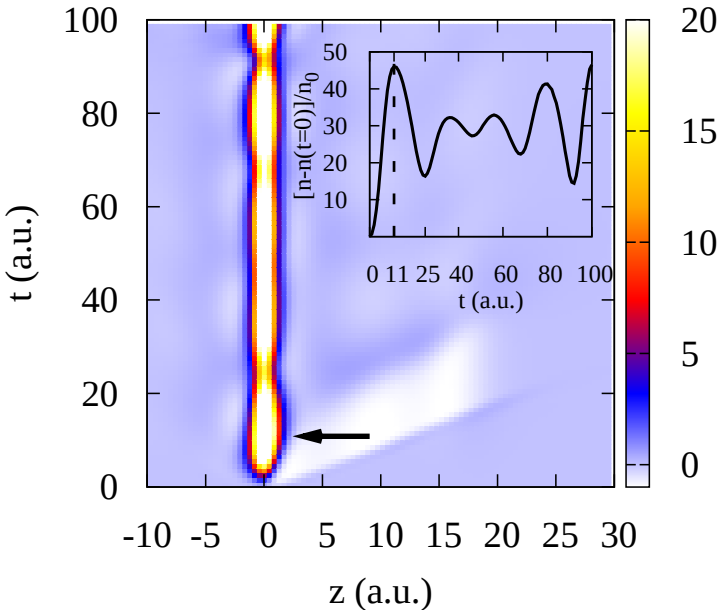

(a)

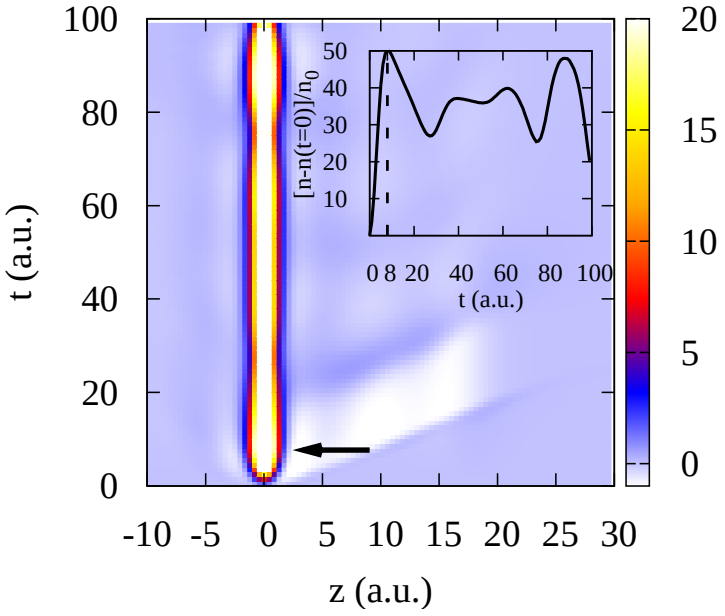

(b)

Figure 4.6: Time evolution of the electronic density of the Na_{106} cluster at the center of which the hole and the electron are created at time $t = 0$. The hole is static and the electron moves away along the positive part of the z-axis. The induced electronic density is shown close to the symmetry z-axis (ρ=0.02 a.u.,z). The time evolves along the vertical axis. Color map shows the change in density in units of the background density n_0. Panel (a) shows the results of the TDDFT calculation of the complete system. In panel (b) the induced density is calculated as a sum of two contributions (see the text for the explanation). The velocity of the electron is $v = 1$ a.u. Insets: Profile of the density plot along the time axis at (ρ=0.02 a.u., z=0.2 a.u.).

4.1.4 Conclusions

In this section a semi-classical model was used to describe the dynamic screening of a moving photoelectron and that of the localized core-hole left behind as a result of the interaction of XUV pulses with small metal clusters. The electron is emitted from the center of the cluster and the motion of the photoemitted electron is described classically.

We have shown that, when the hole is explicitly included in the calculation, the photoemitted electron is accelerated by the cluster electrons that pile up nearby the cluster center to dynamically screen the hole. This effect is observed by comparing the forces acting on the photoemitted electron due to the interaction with the cluster in which a hole is present or absent at the center. In order to quantify the effect of the hole screening we have calculated the energy loss of the photoelectron. We have shown that the presence of the hole reduces significantly the cluster induced energy loss and that this effect is velocity dependent. In the limit of very small velocities we should recover the adiabatic limit and the screening-induced acceleration of the emitted electron along its trajectory should reflect the decrease of the binding energy of the inner shell from which the electron is photoemitted due to the metallic screening provided by the cluster electrons. This change in the binding energy, in our simplified model, is given by the Coulomb interaction of a positive point-particle (the hole) with the screening electron cloud around it in a static calculation. Interestingly, however, we find here that the acceleration effect strongly depends on the velocity of the photoemitted electron. For sufficiently high energy photons, the measured binding energy of the inner shell (given by the energy position of the elastically photoemitted electrons) should increase due to the fact that the screening of the hole takes place in a characteristic, fixed time-scale. Although this effect should be observable experimentally, to the best of our knowledge we are not aware of a clear measurement of such photon-energy dependency of the binding energy of atomic core shells in metals.

These conclusions were obtained using a relatively simple approximation in which the photoemitted electron moves with constant velocity. The conclusions are proven to remain valid when the interaction between photoemitted electron and core-hole left behind is included in the calculation and the velocity of the electron is allowed to vary with time. We have illustrated the time evolution of

the electron density in the cluster during the photoemission process and we have shown that the TDDFT calculation allows us to see the coupled effect of the screening of both the hole and the electron in the relaxation processes inside the cluster.

4.2 Dynamic screening and charge transfer processes in the photoemission from an adsorbate on a metal cluster

The field of photoemission spectroscopy was pioneered in the early 1960's. In particular, core-level photoemission from molecular adsorbates has been the subject of experimental studies for several decades. It was observed that the photoemission spectrum of a molecule adsorbed on a metal surface is very different from that of the free molecule [84–86]. There are different features that can appear in the spectrum of the adsorbate: either additional peaks close to the main peak with lower intensity or the broadening or shifting of the main peak. Some of these new spectral features are the shake-up and shake-off satellites. The existence of satellite structures in core-level photoemission spectra of adsorbates have multiple origins, one of them being charge transfer processes from the metal surface to screen the core-hole left in the adsorbate. [84–89]. Therefore, the effect of the charge transfer (CT) is very important and it should be taken into account in the theoretical calculations of the photoemission spectra of adsorbates [90]. The adsorbate-substrate distance plays an important role in the process of CT to the adsorbate [89]. This is because the energies and widths of the atomic levels of the adsorbate vary depending on the distance from the metal surface [91–93].

In this section, we study the dynamic screening of an electron photoemitted from a core-level of an adsorbate weakly interacting with the surface of a metal cluster, e.g., a noble gas. We use a very simplified model to describe this process since our emphasis is on describing the dynamics of the cluster electrons. Noble gases interact weakly with metal surfaces and have relatively large adsorption heights, which justify our assumption of an unperturbed cluster as an initial description of our system. Once the photoemission process from a core-level of the adsorbed noble gas takes place, a localized hole is left and the excited

adsorbate can be approximated by a hydrogen-like or alkaline ion. Here, we will not attempt to improve the model using a specific pseudopotential to describe a particular adsorbed atom, but we will use the simplest possible model to reveal some basic phenomena related to the interplay of the different time-scales of the processes at play.

We show that, in the case of the photoemission from an adsorbate, the photoelectron also experiences an accelerating force due to the screening of the core hole by the cluster electronic charge, as it was observed in the case of the photoemission from the center of the cluster. To quantify this effect we calculate the energy change of the photoemitted electron and show that the energy of the electron increases due to the screening of the hole. This effect is studied in detail for different adsorbate-substrate separation distances and for a range of velocities of the photoemitted electron. By looking at the time evolution of the electronic density, we analyze the different CT processes depending on the parameters of the calculations, such as the distance from the adsorbate to the metal surface, the velocity of the photoelectron, and the type of substrate.

The system under study consists of a metallic cluster of spherical shape and an adsorbate at a distance d from the cluster surface. The metal cluster is represented in the framework of SJM. The core hole of the adsorbate and the photoemitted electron are modeled as classical positive and negative point charges respectively.

In this section, we use the same methodology as of section 4.1. We start the time evolution at $t = 0$, when the photoelectron (el) and the core hole (h) are created at the position of the adsorbate.

The scheme of the process under study is shown in Fig. 4.7. The photoelectron moves with a constant velocity along the z-axis $[\rho_{\rm el} = 0,\ z_{\rm el}(t)]$. The hole is fixed on the z-axis, at a given distance from the cluster surface $[\rho_{\rm h} = 0,\ z_{\rm h} = R_{\rm cl} + d]$.

The potential created by these charges and acting on the cluster electrons is:

$$\triangle V(\rho, z, t) = V_{\rm el}(\rho, z, t) + V_{\rm h}(\rho, z, t), \tag{4.11}$$

where

$$V_{\rm el}(\rho, z, t) = \frac{1}{[(z_{\rm el}(t) - z)^2 + \rho^2]^{1/2}}\Theta(t), \tag{4.12}$$

and

$$V_{\rm h}(\rho, z, t) = -\frac{1}{[(z_{\rm h} - z)^2 + \rho^2]^{1/2}}\Theta(t). \tag{4.13}$$

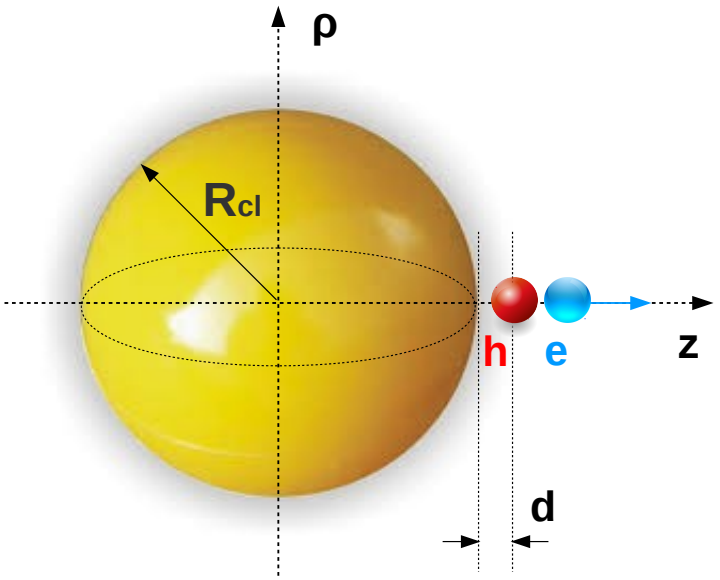

Figure 4.7: Sketch of the photoemission process. An electron and a hole are created at a given distance d from the surface of the spherical cluster, at $t = 0$. Both are represented by classical point particles. The electron starts to move along the z-axis with constant velocity v.

Since in the previous section we have observed that the Coulomb interaction between the hole and the photoelectron does not have a significant influence on the effect of the screening of the electron, the direct interaction of the photoemitted electron and the core hole is not included in this case.

In this section, we study two different metallic clusters: aluminum (Al) with $r_s = 2.07$, and sodium (Na) with $r_s = 4$, with 106 electrons in each cluster. The radii of these clusters are 18.93 and 9.8 a.u. respectively. The adsorbate-cluster distances d are chosen to be 3 a.u. and 6 a.u. Velocities of the photoemitted electron are chosen in the range from 0.02 a.u. up to 2 a.u. The change in the energy of the photoemitted electron due to the screening of the core hole is calculated from the time-dependent force (4.4):

$$\Delta E = v \int F_z^{\mathrm{cls}}(t) dt. \tag{4.14}$$

A schematic view of the system under study is shown in Fig. 4.8. Figure 4.8a shows the KS effective potential $V_{\mathrm{eff}}(\mathbf{r})$ of the Na_{106} cluster (blue curve) with the corresponding valence electronic energy levels (blue horizontal lines) and the potential created by the hole localized at a distance 3 a.u. from the cluster surface

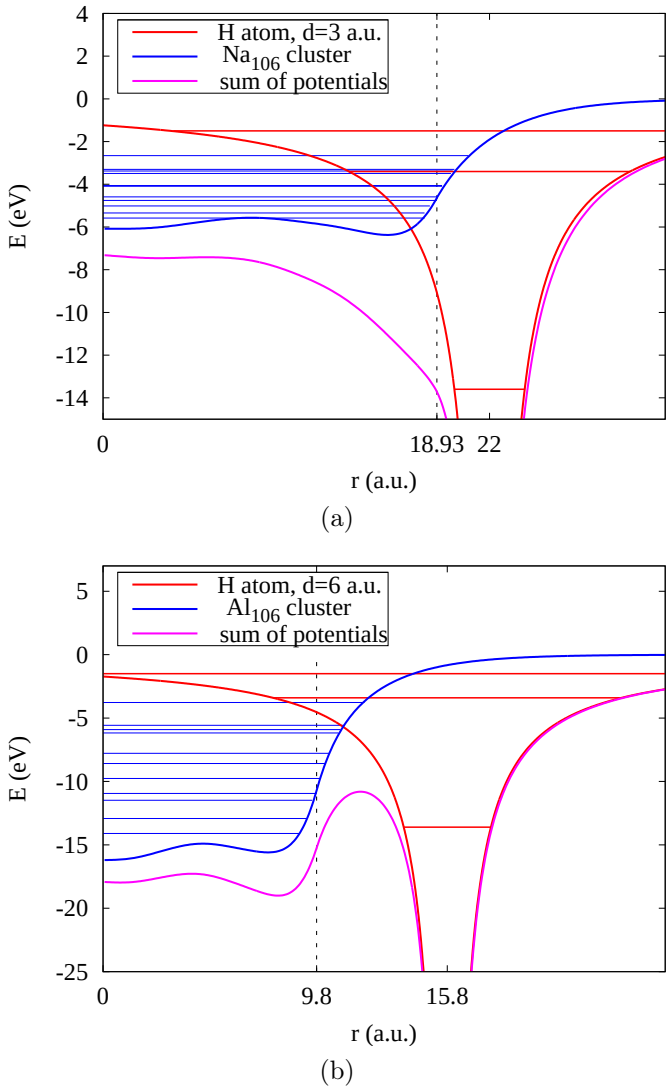

Figure 4.8: Simplified sketch of energy diagrams for the adsorbate on the surface of a cluster. Blue lines represent the occupied levels and the effective potential describing the ground state of a) a Na cluster and b) an Al cluster containing 106 electrons. The red lines represent the levels and $1/r$ potential created by a localized hole located at a distance $d = 3$ a.u. from the cluster surface in panel a), and $d = 6$ a.u. in panel b). Finally, the purple line represents the sums of both potentials and can be interpreted as the $t \to 0$ effective potential felt by the cluster electrons when the photoemitted electron has a very large kinetic energy (i.e., in the sudden creation approximation for the core-hole).

with the energy levels of that potential, corresponding to an H atom (shown in red). The sum of these potentials is plotted as well (purple), and can be thought as the initial potential in which the electrons evolve when the kinetic energy of the photoemitted electron tends to infinity, corresponding to the sudden creation

approximation of the hole. Fig. 4.8b is the same as Fig. 4.8a but for Al_{106} and the localized hole at a distance 6 a.u. from the cluster surface. For both clusters, the energy of the highest occupied level corresponds to the Fermi energy. The positions of hydrogen-like levels with respect to the cluster electronic levels and the height of the potential barrier between cluster and the attractive potential created by the hole determine the character of the charge transfer from the cluster to the adsorbate. The different CT processes are discussed later in the subsection "Time evolution of the electronic density".

4.2.1 Force and change in energy experienced by the emitted electron

When the core hole is created in the adsorbate on the surface of the cluster, the electronic charge of the cluster immediately starts to screen the positive charge of the hole. The screening of the hole in turn affects the movement of the photoemitted electron. We start our study from the analysis of the force experienced by the photoelectron due to the screening of the hole. The force along the z-axis is calculated using Eq. (4.4) and is shown in Fig. 4.9 and Fig. 4.10 as a function of the electron position $z_{\rm el}$ for the adsorbate/Na_{106} and the adsorbate/Al_{106} respectively, and for different velocities of the electron. The z-axis starts from the value corresponding to the position of the hole $z = (R_{\rm cl} + d)$. In the previous section we have already shown that the electron photoemitted from the center of the cluster experiences an accelerating force due to the screening of the hole. In the case of the photoemission from the adsorbate we also see (Fig. 4.9 and Fig. 4.10) that the force is positive all along the trajectory of the electron. This means that the electron is being accelerated. The reason for the acceleration is the repulsion of the electron from the hole vicinity by the cluster electronic charge that is displaced to screen the hole. The screening process is very fast. Therefore, it affects more to electrons moving with low velocity. This is seen from Figs. 4.9 and 4.10, where the force increases when the velocity of the photoemitted electron decreases.

Another observation is that for both systems adsorbate/Na_{106} and adsorbate/Al_{106}, in the case of the adsorbate-substrate distance equal to 6 a.u., the force has oscillations. The latter is not observed in the case of distance $d = 3$ a.u. and high

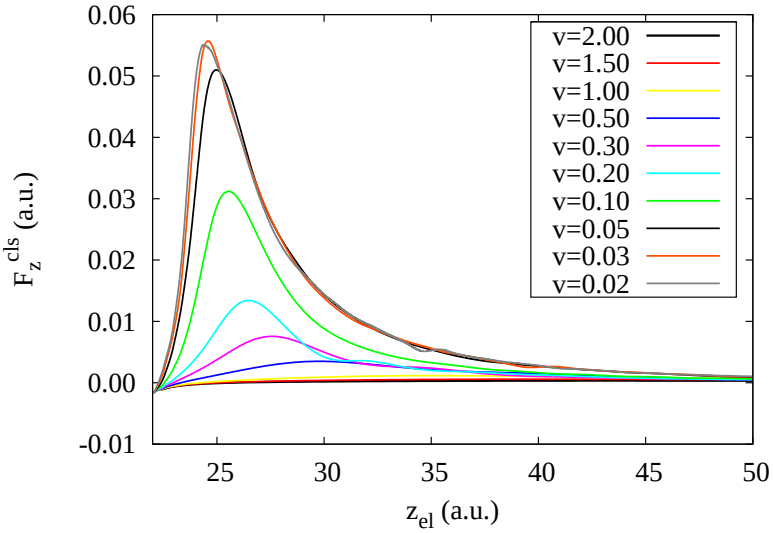

(a) $d = 3$ a.u.

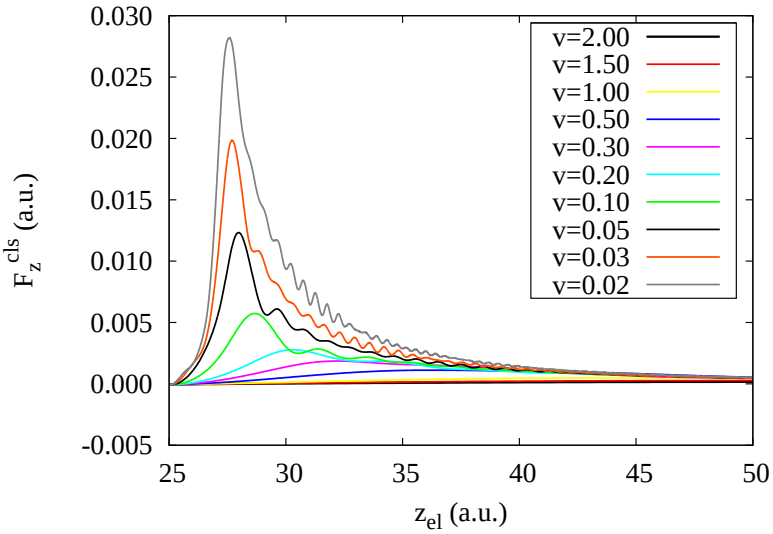

(b) $d = 6$ a.u.

Figure 4.9: Force felt by the electron photoemitted from a model adsorbate on the surface of the Na cluster due to the screening of the core hole as a function of the electronic position. Velocities are in atomic units.

electron velocities. We show (in the subsection "Time evolution of the electronic density") that the oscillations in the force are reflecting the oscillations of the electronic density in the clusters.

Since the photoelectron feels a repulsive force from the screening charge, the energy of the electron changes. The change in energy ΔE is calculated from the force using Eq. (4.14). This quantity is shown in Fig. 4.11 as a function of the electron velocity for both metals and for both distances d. We can see that

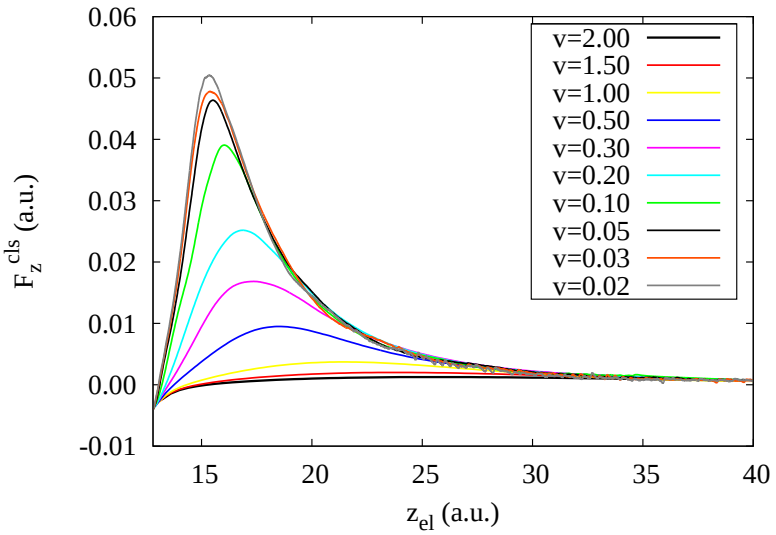

(a) $d = 3$ a.u.

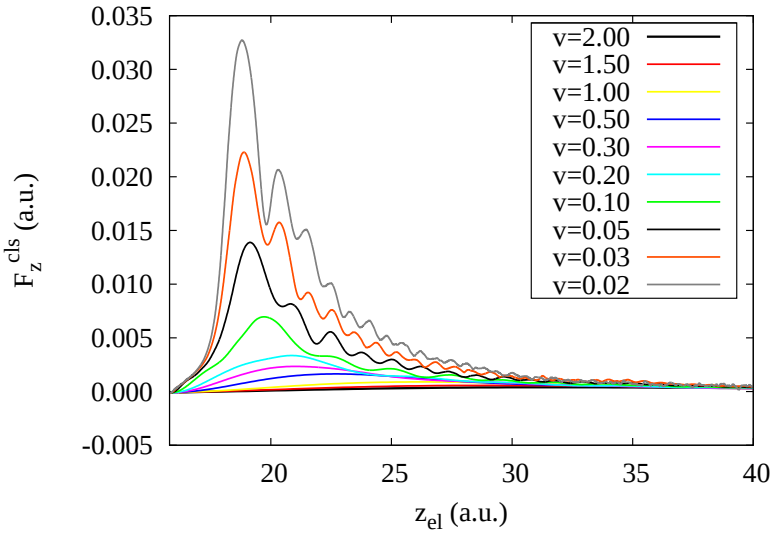

(b) $d = 6$ a.u.

Figure 4.10: Force felt by the electron photoemitted from a model adsorbate on the surface of the Al cluster due to the screening of the core hole as a function of the electronic position. Velocities are in atomic units.

values of ΔE are in the same range for both metals, but strongly depend on the adsorption distance and on the velocity of the photoemitted electron. The electron gains more energy when the distance between metal cluster and adsorbate is shorter.

From energy diagrams in Fig. 4.8 it becomes obvious that the CT processes must be strongly dependent on the distance and on the electron velocity. At shorter adsorbate-substrate distance the potential barrier between cluster and

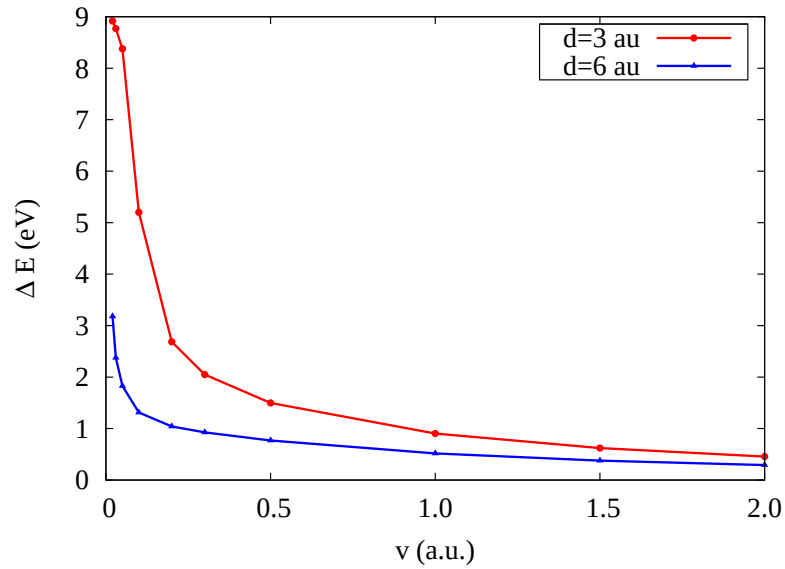

(a) Na cluster

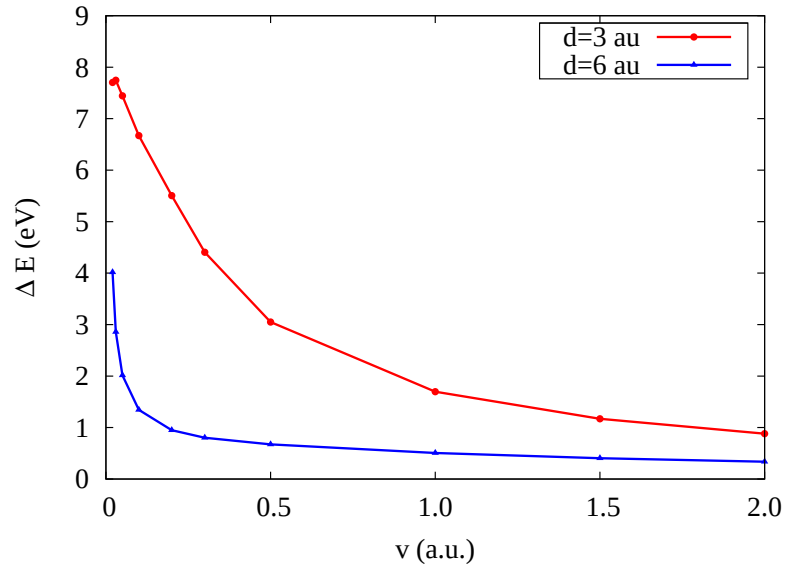

(b) Al cluster

Figure 4.11: Change in energy of the photoelectron due to the interaction with the cluster as a function of the electron velocity for a) adsorbate/Na_{106}, and b) adsorbate/Al_{106}.

the attractive potential created by the hole is small. Therefore more charge can get across the barrier to the adsorbate to screen the hole. This leads to a larger force acting on the photoemitted electron and therefore to a larger energy gain. At lower electron velocities the energy change is larger because slower electrons spend more time close to the core hole and thus are more affected by the hole

screening.

In order to understand better the influence of the core hole screening on the force that the photoemitted electron experiences, we analyze the time evolution of the electronic density in clusters after the sudden creation of a core hole and a photoelectron at the position $(R_{\rm cl} + d)$.

4.2.2 Time evolution of the electronic density

As we have seen in Fig. 4.9b and Fig. 4.10b, in the case of the adsorbate-cluster distance $d = 6$ a.u. the force felt by the moving electron has oscillations. The oscillations in the force are reflecting oscillations of the electronic density. Fig. 4.12 shows the time evolution of the electronic density along the $z-$axis in the Na_{106} cluster after the sudden creation of a core hole and an electron, which starts to move with velocity 0.1 a.u. We see in Fig. 4.12a (corresponding to the case of $d = 3$ a.u.) that the density change is roughly constant in time, with no oscillations. The same behavior is observed in the force, which does not have any oscillations at low velocities of the photoemitted electron for $d = 3$ a.u. (Fig. 4.9a). However, the density oscillates in Fig. 4.12b, corresponding to the case of $d = 6$ a.u. These oscillations are also seen in the force (Fig. 4.9b). A similar correspondence between force and density oscillations is observed for the adsorbate/Al_{106} system.

In the two cases shown in Fig. 4.12, the density accumulation is located at the position of the core hole. This means that electronic charge is transferred from the cluster to the adsorbate. However, in the case of $d = 6$ a.u. (Fig. 4.12b), there is also a small peak located near the border of the cluster besides the main peak. The different behavior of the electronic density is a consequence of the charge transfer occurring to different energy levels of the adsorbate, depending on the adsorption distance.

In Fig. 4.13 the time evolution of the electronic density is shown for the adsorbate/Na_{106} system and for electron velocity $v = 1$ a.u. We can see that in this case the picture is quite similar for both distances d. Namely, there are two peaks in the induced density and the density oscillates. This means that not only the adsorption distance affects the CT process, but the velocity of the photoemitted electron also determines to which level of the adsorbate the charge is being transferred. We can check the latter by calculating the projections, P,

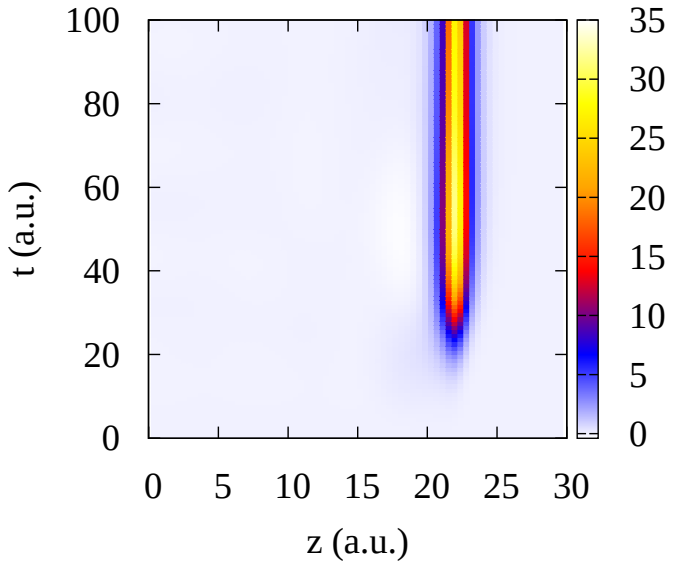

(a) $d = 3$ a.u.

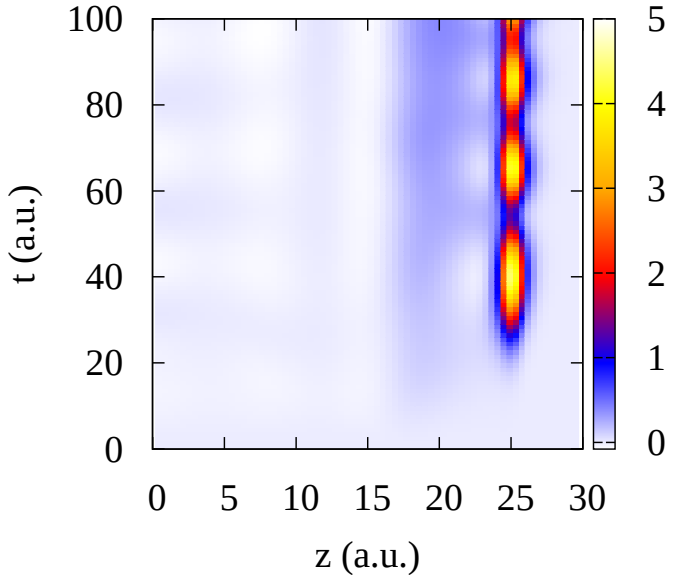

(b) $d = 6$ a.u.

Figure 4.12: Time evolution of the electronic density when a photoelectron is emitted from an adsorbate on the surface of a Na_{106} spherical cluster. The change in electronic density is shown in units of the background density n_0 as a function of time and distance from the center of the cluster. Velocity of the electron is $v = 0.1$ a.u. Radius of the cluster is $R_{cl} = 18.93$ a.u.

of the cluster wave functions onto the hydrogen-like states bound to the potential created by the localized hole. The results of these calculations are shown in Fig. 4.14 for velocity 0.1 a.u and are in agreement with the observations in Fig. 4.12 and also with similar results for the adsorbate/Al_{106} system, not shown

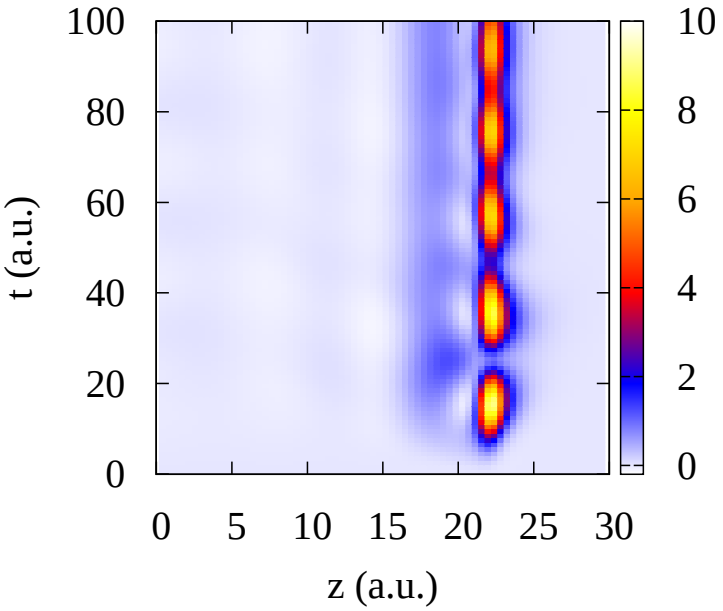

(a) $d = 3$ a.u.

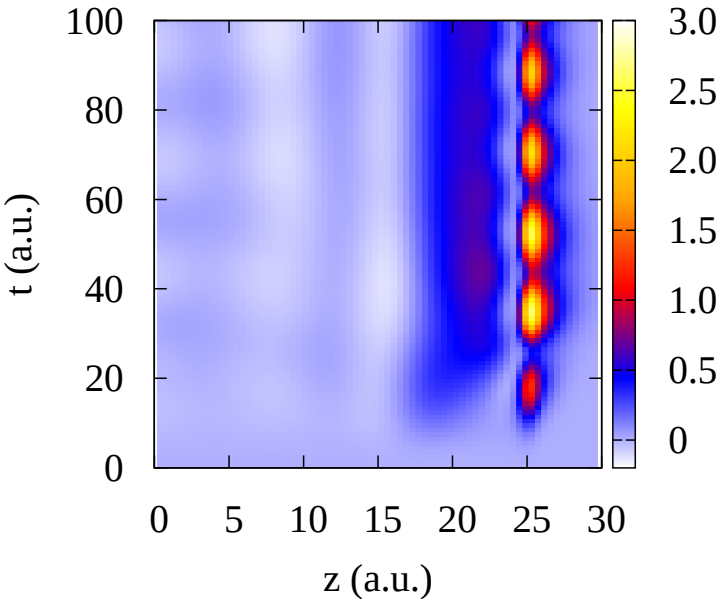

(b) $d = 6$ a.u.

Figure 4.13: Time evolution of the electronic density when a photoelectron is emitted from an adsorbate on the surface of a Na_{106} spherical cluster. The change in electronic density is shown in units of the background density n_0 as a function of time and distance from the center of the cluster. Velocity of the electron is $v = 1$ a.u. Radius of the cluster is $R_{cl} = 18.93$ a.u.

here.

We have calculated projections for both systems (Na and Al clusters), for two

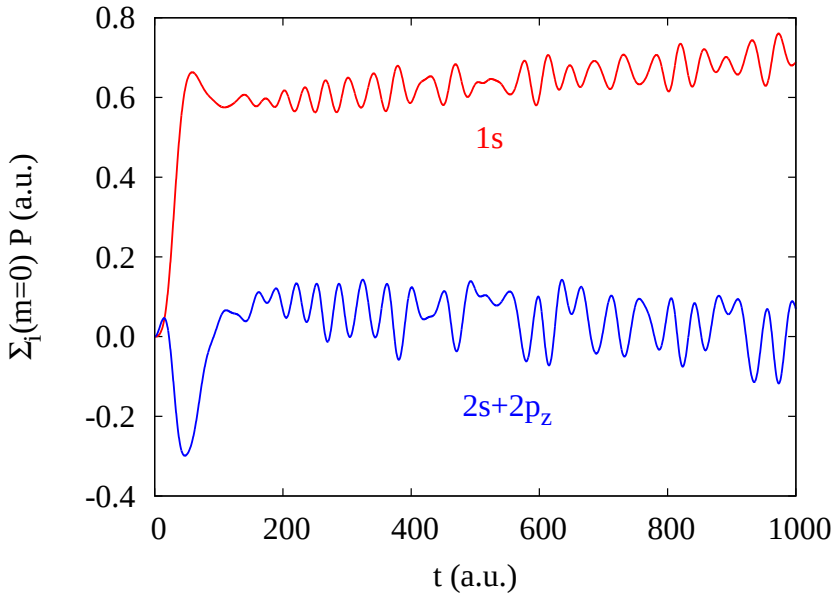

(a) $d = 3$ a.u.

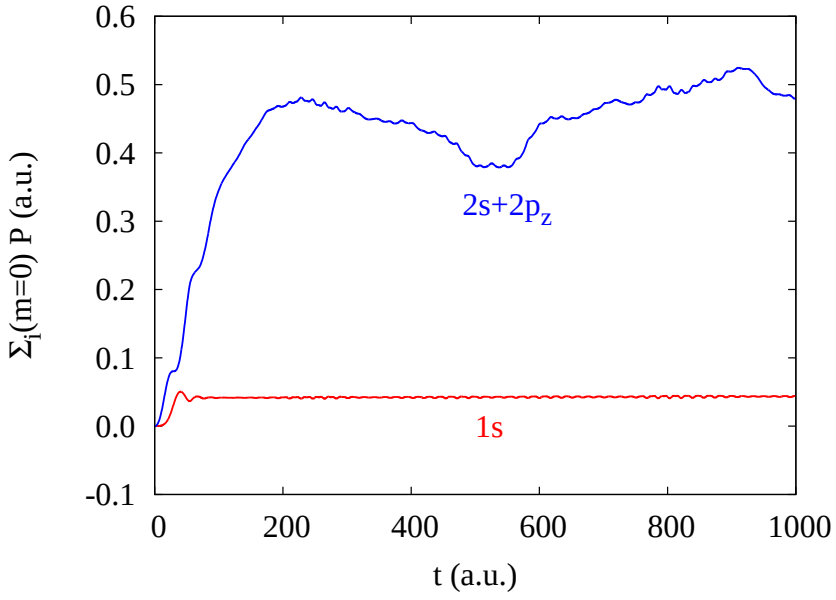

(b) $d = 6$ a.u.

Figure 4.14: Calculated projections of the electronic states of the Na cluster onto the hydrogen-like $1s$ and $(2s + 2p_z)$ states of the hole potential as a function of time. The adsorbate-surface distances are a) $d = 3$ a.u., b) $d = 6$ a.u. Velocity is $v = 0.1$ a.u.

distances d, and for two velocities of the electron, $v = 0.1$ and $v = 1$ a.u. We projected the cluster wave functions onto the hydrogen $1s$, $2s$, $2p_z$ states and onto two hybrid states: $(2s + 2p_z)$ and $(2s - 2p_z)$. Analytical expressions are

used for the hydrogen states. The quantity shown in Fig. 4.14 and Fig. 4.15, $\sum_i (m = 0)P$, is a sum of projections of the cluster states with $m = 0$. For the system adsorbate/Na_{106} with $d = 3$ a.u. and electron velocity $v = 0.1$ a.u. (Fig. 4.14a) the largest projection is onto the hydrogen 1s state. Indeed, if we look at the simplified energy diagram of Fig. 4.8a, we can see that at close adsorbate-cluster distance there is no potential barrier. Moreover, the low velocity allows the electron to perturb the adsorbate levels a longer period of time and, as a consequence, the levels go up in energy for a longer time as well. Therefore, the cluster electrons can occupy the deepest level of the potential created by the hole. This explains the density accumulation around the core hole shown in Fig. 4.12a. The cluster electrons are transferred to the hydrogen-like $1s$ state of the adsorbate and can not go back. An alternative way to understand this result is using the concept of the adiabatic transformation. If the photoemitted electron moves sufficiently slowly, we can eventually recover the adiabatic limit in which the system is always in its ground-state configuration. Thus, for short adsorbate-surface distances and in absence of large tunneling barriers to overcome, we start to approach this limit for the lowest velocities in our simulations, leaving a highly occupied $1s$ level. This is the reason for which there are no oscillations of the electronic density in this case.

In the rest of the calculations for the Na cluster ($d = 3$ a.u., $v = 1$ a.u., and $d = 6$ a.u., velocities $v = 0.1$ and $v = 1$ a.u.) the largest projection is onto the hydrogen $(2s + 2p_z)$ hybrid state. One of these cases ($d = 6$ a.u., $v = 0.1$ a.u.), is shown in Fig. 4.14b. This is consistent with the structure of the induced density in Fig. 4.12b and Fig. 4.13. In these cases the cluster electrons populate the $(2s + 2p_z)$ hydrogen state, which is resonant with the energy levels of the cluster. When the adsorbate-cluster distance is small ($d = 3$ a.u.), but the electron velocity is high ($v = 1$ a.u.), the levels of the adsorbate are almost not affected by the photoemitted electron. Therefore, the cluster electrons can not occupy the $1s$ level of the hole potential. At large distances ($d = 6$ a.u.), the potential barrier between the cluster and the adsorbate is high and it is impossible for the cluster electrons to populate the $1s$ level of the hole potential sufficiently fast to be influenced by the photoemitted electron. Thus, the main CT process takes place to those levels of the ionized adsorbate that are resonant with the cluster states and for which the effective tunneling barrier is smaller, i.e., the $2s$ and $2p$ levels. Furthermore, the interaction between $2s$ and $2p$ levels of the

ionized adsorbate and the cluster states gives rise to hybridization and translates into a coherent, oscillatory dynamics. This explains the oscillations in time of the change in electronic density (Fig. 4.12b and Fig. 4.13).

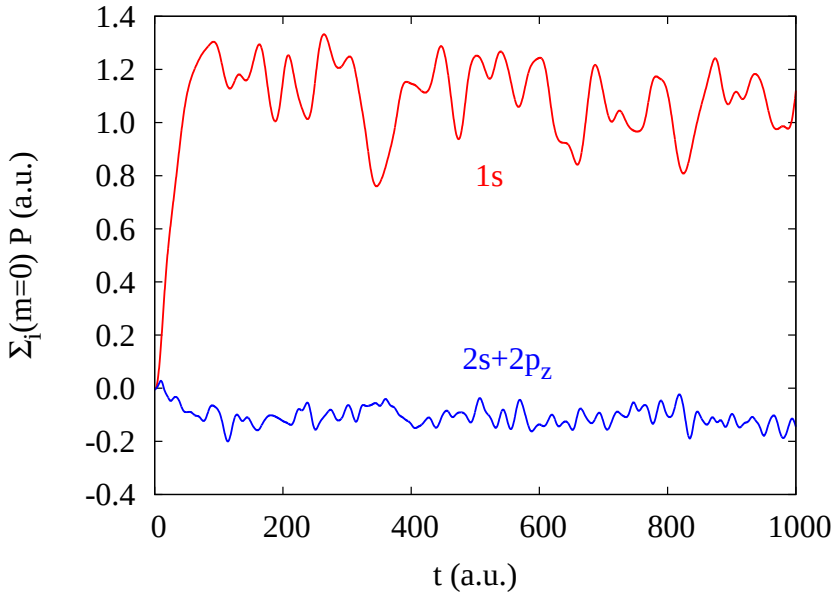

(a) Al cluster

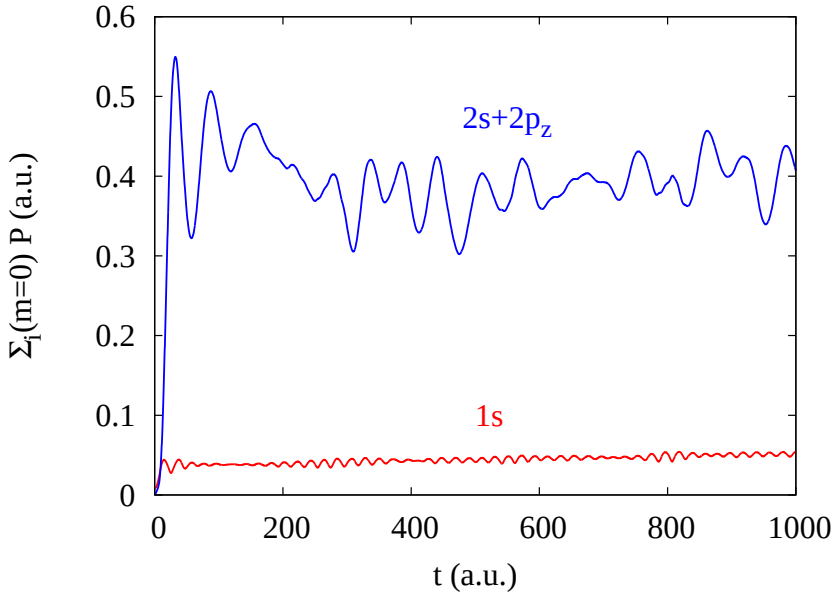

(b) Na cluster

Figure 4.15: Calculated projections of the electronic states of (a) Al cluster and (b) Na cluster onto the hydrogen-like $1s$ and $(2s+2p_z)$ states of the hole potential as a function of time. The adsorbate-surface distance is $d = 3$ a.u., velocity is $v = 1$ a.u.

For the adsorbate/Al_{106} system the picture is different. The aluminum occupied energy levels are resonant with the $1s$ state of the ionized adsorbate. At short distances ($d = 3$ a.u.) the potential barrier is low and the cluster electrons can populate the $1s$ level, even when the photoemitted electron is moving with high velocity. This is proved by the calculation of the projections. At $d = 3$ a.u. for both velocities the largest projection is onto the $1s$ level. Figure 4.15a shows the projections for Al_{106} and the hydrogen-like states at a distance $d = 3$ a.u. with the electron velocity $v = 1$ a.u. The largest projection is onto the $1s$ level of the ionized adsorbate, which is not the case for the Na cluster with the same parameters (Fig. 4.15b). When the distance is large ($d = 6$ a.u.), the barrier is higher (Fig. 4.8b) and the cluster electrons occupy the $(2s + 2p_z)$ state of the ionized adsorbate, similarly to the case of Na.

Concluding this subsection, we have shown that, depending on the adsorbate-surface distance and on the velocity of the photoemitted electron, the charge transfer from the cluster to the ionized adsorbate can be different. The height of the barrier and the action of the photoemitted electron define which level of the ion is going to be populated by the screening charge of the cluster. The character of the charge transfer in turn has an influence on the value of the energy gained by the photoemitted electron. Coming back to Fig. 4.11, we can see that, for the distance 6 a.u., the values of ΔE are very similar in both systems. This is because in both systems at $d = 6$ a.u. the CT occurs to the hydrogen-like $(2s + 2p_z)$ level. But if one looks at the values of ΔE when the distance is 3 a.u., one can see that the slopes of the curves are different in the two systems. Namely, in the case of adsorbate/Al_{106} the values of ΔE are much larger than in the case of adsorbate/Na_{106} at $d = 3$ a.u. This means that the charge transfer to the $1s$ level of the ionized adsorbate (as happens in adsorbate/Al_{106} at $d = 3$ a.u.) leads to a larger energy gain by the photoemitted electron than the charge transfer to the $(2s + 2p_z)$ state. This can be expected since, in the low velocity limit, the energy of the photoemitted electron should reflect the changes in the binding energy of the hole as it gets screened. The interaction with a more confined $1s$ charge distribution should produce a large change in the binding energy than that produced by the occupation of the $(2s + 2p_z)$ hybrid level.

4.2.3 Different contributions to the total force

As we have shown, the velocity of the photoemitted electron has an influence on the charge transfer from the cluster to the adsorbate. This is because in the time-dependent calculations we take into account the coupled dynamic screening of both the core hole and the photoelectron. Therefore, the screening of the core hole is affecting the screening of the electron, and vice versa. The presence of the electron close to the hole leads to the delay of the hole screening (and the charge transfer). Our method allows us to take into consideration the effect of both the charge transfer and the coupled screening of hole and electron when calculating the energy change of the photoemitted electron.

In order to point out the importance of taking into account these two effects, we show in Fig. 4.16 the force acting on the photoemitted electron in different approximations. The force is shown for the electron photoemitted from the adsorbate on the surface of a Na_{106} cluster at distances $d = 3$ a.u. (Fig. 4.16a) and $d = 6$ a.u. (Fig. 4.16b). In both figures the red curve corresponds to the force that includes the effect of both the charge transfer from the cluster and the coupled dynamic screening of the hole and the electron. This force is obtained from the density that is calculated by propagating the cluster wave functions in the presence of both the hole and the electron. For comparison the force experienced by the photoelectron is calculated as a sum of two different contributions. The blue curve corresponds to the force obtained as

$$F^{\mathrm{cls}}_{\mathrm{el+h}}(z) = F_{\mathrm{el}}(z) + F_{\mathrm{h}}(z_{\mathrm{h}}). \tag{4.15}$$

Here $F_{\mathrm{el}}(z)$ is the force acting on the moving electron in the case when there is no hole. $F_{\mathrm{h}}(z_{\mathrm{h}})$ is the force acting on the point in space corresponding to the electron position when a hole is created at the position $(R_{\mathrm{cl}} + d)$ at $t = 0$. Therefore, the force $F^{\mathrm{cls}}_{\mathrm{el+h}}$ includes the effect of the charge transfer, but does not include the coupled hole-electron screening.

The green curve is obtained as

$$F^{\mathrm{cls}}_{\mathrm{el+(-el)}}(z) = F_{\mathrm{el}}(z) + (-1)F_{\mathrm{el}}(z_{\mathrm{h}}). \tag{4.16}$$

Here $F_{\mathrm{el}}(z)$ is the same as in the previous case and $F_{\mathrm{el}}(z_{\mathrm{h}})$ is the force acting on the point in space corresponding to the electron position when there is an

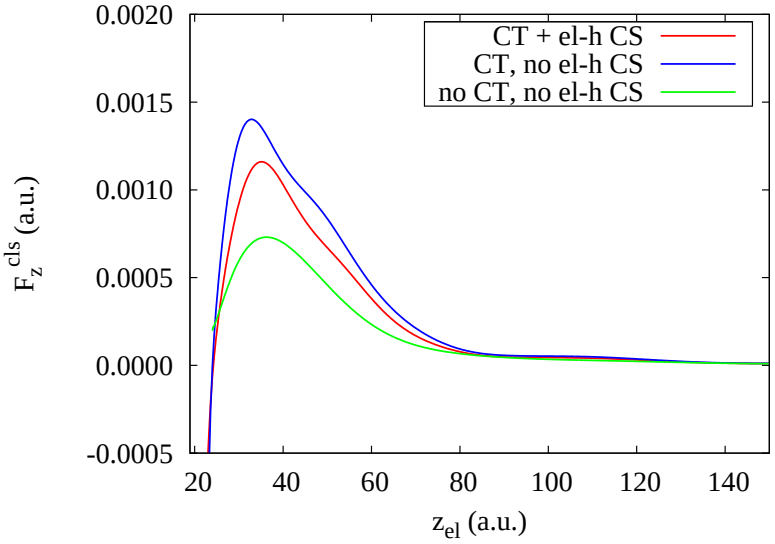

(a) $d = 3$ a.u.

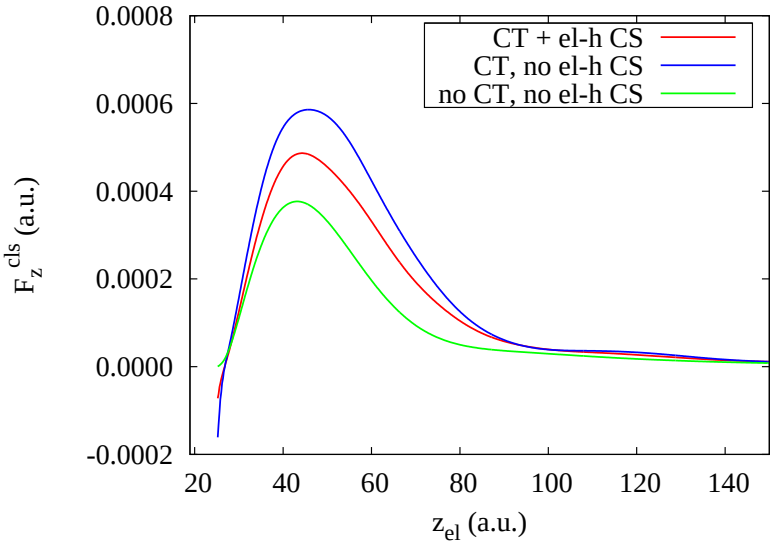

(b) $d = 6$ a.u.

Figure 4.16: Cluster induced force acting on the electron, calculated in different approximations. Red line shows the total dynamic force, including both the charge transfer and the coupled electron-hole screening effects; blue line shows the force that includes the effect of the charge transfer but does not include the coupled electron-hole screening; green line corresponds to the force that does not include neither the charge transfer nor the coupled electron-hole screening. All the forces are shown as a function of the electron position for the electron emitted from the adsorbate on the Na_{106} cluster at a distance a) $d = 3$ a.u., and b) $d = 6$ a.u. Electron velocity is 1 a.u. CT - charge transfer, CS - coupled screening.

electron at the position $(R_{\rm cl} + d)$ and then taken with the opposite sign. This second contribution is an approximation used to replace the hole that allows us to get rid of the effect of the charge transfer. Thus the force $F^{\rm cls}_{\rm el+(-el)}$ does not include neither the effect of the charge transfer nor the effect of the coupled hole-electron screening. However, it includes the effect of the long range screening of the hole by the cluster electrons (image charge).

In Fig. 4.16 (a) and (b) we see that, if the effect of the coupled dynamic screening of the core hole and the photoelectron is not taken into account, the force is overestimated (blue curve is higher than the red one). Since the blue line does not include the effect of the simultaneous presence of both hole and electron, it does not take into consideration the delay in the hole screening due to the presence of the electron close to the hole. The force shown by the green line is lower than the real force (red line). This is because the green line does not include the effect of the charge transfer which is very important and should be taken into account. With this we can conclude that the coupled dynamic screening of the hole and the electron is very important and has to be treated self-consistently, as we do in this work when calculating the force acting on the electron photoemitted from an adsorbate on the surface of a metal cluster.

4.2.4 Image force

It is known that any charged particle in front of a polarizable surface creates an image charge in the surface. Therefore, the charged particle feels the attractive force of the image charge induced in the material. The image potential outside a flat surface is inversely proportional to the distance r from the charge to the surface $(-1/4r)$, with $r = z - Z_{\rm surf}$ in our system of coordinates and $Z_{\rm surf}$ being the location of the surface image plane on the z-axis. In our case there are two charges: the electron moving away from the surface and the hole fixed at a distance d from the surface. For such a combination in front of a flat surface, the image potential on the moving electron is:

$$V^{\rm surf}_{\rm im}(z) = -\frac{1}{4(z - Z_{\rm surf})} + \frac{1}{z - Z_{\rm surf} + d}. \tag{4.17}$$

We find the image force as a derivative of the potential, $F_{\rm im}(z) = -\dfrac{d}{dz}V_{\rm im}(z)$,

and therefore it is represented by the expression:

$$F_{\rm im}^{\rm surf}(z) = -\frac{1}{4(z - Z_{\rm surf})^2} + \frac{1}{(z - Z_{\rm surf} + d)^2}, \tag{4.18}$$

for $z > Z_{\rm surf}$. This force is shown in Fig. 4.17 as a black line for $Z_{\rm surf} = R_{\rm cl}$, where $R_{\rm cl}$ is the radius of the cluster. However, in our case we deal with a spherical cluster and the image potential (and hence the image force) outside a small sphere is different from that of the flat surface. The classical image potential for one charge outside a neutral sphere with radius $R_{\rm cl}$ has the following form [94]:

$$V_{\rm im}(z) = \frac{-R_{\rm cl}^3}{2z^2(z^2 - R_{\rm cl}^2)}. \tag{4.19}$$

Taking into account the image potential due to the presence of the hole near the surface of the sphere this expression is modified:

$$V_{\rm im}^{\rm sphr}(z) = -\frac{R_{\rm cl}^3}{2z^2(z^2 - R_{\rm cl}^2)} - \frac{R_{\rm cl}}{z(R_{\rm cl} + d)} + \frac{R_{\rm cl}}{z(R_{\rm cl} + d) - R_{\rm cl}^2}. \tag{4.20}$$

Therefore, the classical image force outside a sphere in our case is:

$$F_{\rm im}^{\rm sphr}(z) = -\frac{R_{\rm cl}^3(2z^2 - R_{\rm cl}^2)}{z^3(z^2 - R_{\rm cl}^2)^2} - \frac{R_{\rm cl}(R_{\rm cl} + d)}{z^2(R_{\rm cl} + d)^2} + \frac{R_{\rm cl}(R_{\rm cl} + d)}{(z(R_{\rm cl} + d) - R_{\rm cl}^2)^2}, \tag{4.21}$$

and is shown in Fig. 4.17 as a red line. The two other curves in Fig. 4.17 correspond to the dynamic force experienced by the electron outside a spherical cluster in the presence of the hole near the surface of the cluster. The dynamic forces are obtained using Eq. (4.16) in order to exclude the effect of the charge transfer and to be able to compare these forces with the classical ones. The dynamic forces are shown for the case of electron velocities 0.05 a.u. (blue line) and 0.1 a.u. (purple line). All the forces are shown for the Na_{106} cluster with the adsorbate at a distance $d = 3$ a.u. from the cluster surface. We can see that for both velocities the dynamic forces are very similar. This means that for such low velocities the dynamic force roughly reaches a stationary value (adiabatic limit).

From Fig. 4.17 we can see that the classical image force outside a flat surface is not a good approximation for the dynamic force. The classical image force outside a neutral sphere is a better approximation, but it can represent the dynamic force only at large distances from the cluster surface. At close distances, we see that

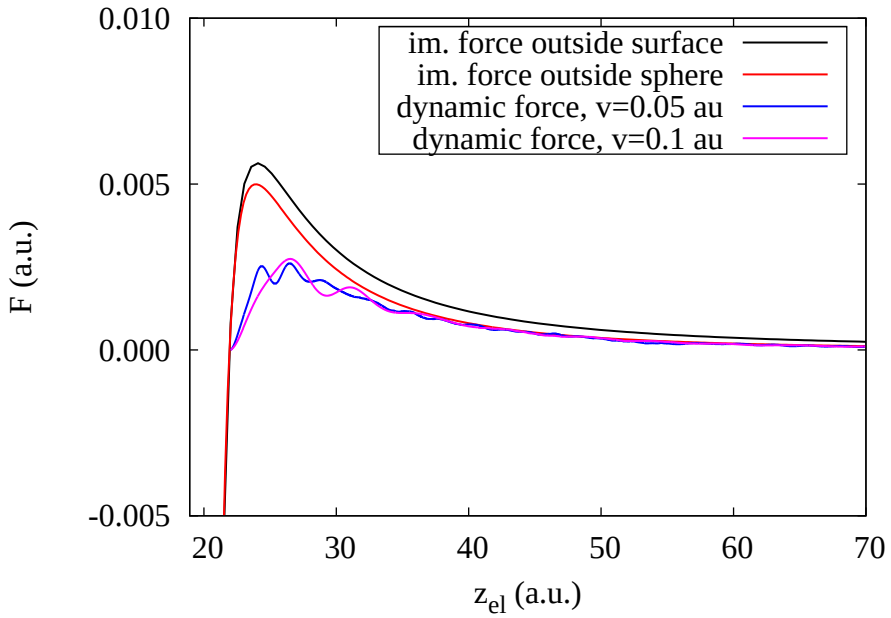

Figure 4.17: Classical image force felt by the electron outside the flat surface in the presence of a hole near the surface $F_{\rm im}^{\rm surf}$ (black line). Classical image force felt by the electron outside of a sphere in the presence of a hole near the surface of the sphere, $F_{\rm im}^{\rm sphr}$ (Eq. (4.21)) (red line). Dynamic force as a superposition of different contributions (Eq. (4.16)) is shown for electron velocities 0.05 a.u. (blue line) and 0.1 a.u. (purple line). The force is shown as a function of the electron position. The distance between the surface and the hole is $d = 3$ a.u. The Na_{106} cluster radius is 18.93 a.u.

the dynamic force differs from the classical values. For small values of z, when the photoemitted electron is close to the cluster surface, quantum effects as well as the finite time of the dynamics in the system are important.

4.2.5 Conclusions

We have presented in this subsection a semiclassical study of the photoemission from the core level of a model adsorbate on the surface of Na and Al clusters. The core hole and the photoelectron are modeled as classical point charges. The response of the cluster electronic density to the presence of the hole and the electron is studied by means of TDDFT. From the time-dependent density we have calculated the force acting on the photoemitted electron and the change in energy of the photoelectron. We have analyzed different charge transfer processes depending on the adsorbate-substrate distance, on the electron velocity, and on

the type of substrate.

We have shown that the electron is accelerated due to the repulsive force originated by the electronic charge of the cluster that dynamically screens the hole. Because of this, the electron gains an amount of energy which is different depending on the character of the charge transfer. The latter depends on the adsorbate-substrate distance, on the velocity of the photoemitted electron, and on the substrate material. Slow electrons gain more energy because they spend a longer time at close distance from the hole and therefore are more affected by the charge transfer. In the case of small adsorbate-substrate distance ($d = 3$ a.u.), the change in energy is larger than in the case of larger distance ($d = 6$ a.u.). For the same distance $d = 3$ a.u. and for the same electron velocities, the change in energy is larger in the photoemission from an adsorbate on the surface of the Al_{106}, at least for our simple model adsorbate. This is not only due to the higher electronic density of Al, which provides a more efficient screening, but also due to the different nature of the charge transfer processes involved. While at high and moderate velocities, for the adsorbate/Na_{106} system the charge transfer takes place to the higher energy $2s$ and $2p$ levels of the ionized adsorbate, in the case of the Al_{106} cluster, at short adsorption distances, the $1s$ level gets significantly populated even at large velocities.

By comparing real dynamic forces with different approximations for the force, we have shown that the influence of the charge transfer as well as the effect of the coupled electron-hole dynamic screening are very important for a correct calculation of the force experienced by the photoemitted electron.

Finally, we compared the dynamic force felt by the photoelectron moving away from the cluster with the classical image force outside a flat surface and outside a neutral sphere. We have shown that at large distances the classical image force outside a neutral sphere is a good approximation for the dynamic force, but at close distances from the surface of the cluster quantum effects and a proper account of the dynamical response of the cluster become important.

4.3 Summary

In summary, in this chapter we used a semi-classical model to study the screening of an electron photoemitted from the center of a metal cluster and from an adsorbate on the surface of the cluster. The screening of the hole is studied as well. The hole and the electron are modeled as point charges moving classically and the dynamics of the electrons in the cluster is studied *ab-initio* using real-time TDDFT.

We have shown that the screening of the hole can affect very much the dynamics of the photoemitted electron. The electron can experience an accelerating force due to the piling up of electronic charge around the hole. As a result, the energy loss of the electron decreases. This effect is velocity dependent and it is larger for lower velocities of the electron. The reason for that is the local character of the hole screening which affects more when the electron spends longer times close to the hole vicinity.

In the case of the photoemission from the center of the cluster, the important conclusion is that the observed acceleration of the photoemitted electron remains even in a more realistic calculation in which the velocity of the electron is allowed to vary according to Newton's equations of motion, including the Coulomb attraction between hole and electron. Since this acceleration is due to the screening of the hole, it should reflect the change of the binding energy of the core-level due to the screening. In the limit of very low propagation velocities of photoelectrons this equivalence will be, in principle, guaranteed by the adiabatic character of the system evolution (under the appropriate constraints). However, for large photon energies, our simulations indicate that it should be possible to detect an apparent increase in the binding energy of the core-level as the energy of the photons is increased.

In the case of the photoemission from an adsorbate, the same effect is observed. The electron, photoemitted from the core level of the adsorbate, is accelerated by the electronic charge transferred from the cluster to the adsorbate. We have shown that the amount of energy gained by the photoemitted electron due to the hole screening depends not only on the velocity of the electron, but also on the adsorbate-substrate distance. The reason for that is the different charge transfer processes from the cluster to the adsorbate. We have shown that, depending on the distance between the cluster and the adsorbed atom, the electrons from the

cluster can transfer to the core level of the atom and remain there or resonantly transfer to the $(2s+2p_z)$ level and back leading to the oscillations of the electronic density in time.

Chapter 5

Energy loss processes in the interaction of charged and neutral projectiles with metal clusters

The slowing down of particles travelling through metallic media is an important problem both from fundamental and practical points of view. As it was mentioned in the introduction, the energy loss of heavy projectiles slowly moving ($v << v_{\mathrm{Fermi}}$) through electronic media can be calculated in the framework of the quasistatic scattering theory using screened potentials obtained from static self-consistent DFT calculations [36, 37, 95, 96]. For fast projectiles ($v > v_{\mathrm{Fermi}}$) the linear theory can be used to calculate the energy loss. Recent calculations using TDDFT improve these results and widen the range of velocities that can be treated [5, 6].

A representative result of the velocity dependent stopping power for an antiproton travelling through Na clusters of different sizes, calculated using TDDFT, is shown in Fig. 5.1. The average stopping power $S = \Delta E/L$ is the average energy loss per unit path length inside the cluster. The characteristic features of the velocity dependent stopping are the following: 1) the stopping power does not strongly depend on the size of the cluster, i.e., it is characteristic for the particular metal density; 2) at low velocities the stopping is linear with velocity; 3) at a certain velocity the stopping power reaches a maximum, after which it decreases approaching zero at high velocities. The two limits of zero stopping are the velocities $v \to 0$ and $v \to \infty$. When the particle moves with velocity approaching zero the process is adiabatic. This means that the typical velocities

of the medium electrons are much higher than the projectile velocity and thus the electronic density of the cluster has always enough time to rearrange to respond to the change of position of the projectile. In the adiabatic limit and in a homogeneous infinite electron gas, the screening cloud surrounding the projectile is symmetric. In a finite system, as the clusters we use in this work, this is not the case. However, the effect of the surfaces for the particle moving towards the cluster and away from the cluster cancels when we calculate the average energy loss, integrating the force over the whole trajectory. Therefore the average energy loss of the particle is approaching zero for velocities $\upsilon \to 0$.

In the limit of a very high velocity the stopping is approaching zero as well. In this case the projectile moves much faster than the electrons of the system, which thus have no time to respond to the movement of the projectile and therefore do not cause any force.

In this chapter we study how the stopping power (or the energy loss) of the projectile as a function of velocity can change depending on different initial conditions, such as the initial state of the cluster (ground or excited state) and the presence of another particle in close proximity to the moving projectile.

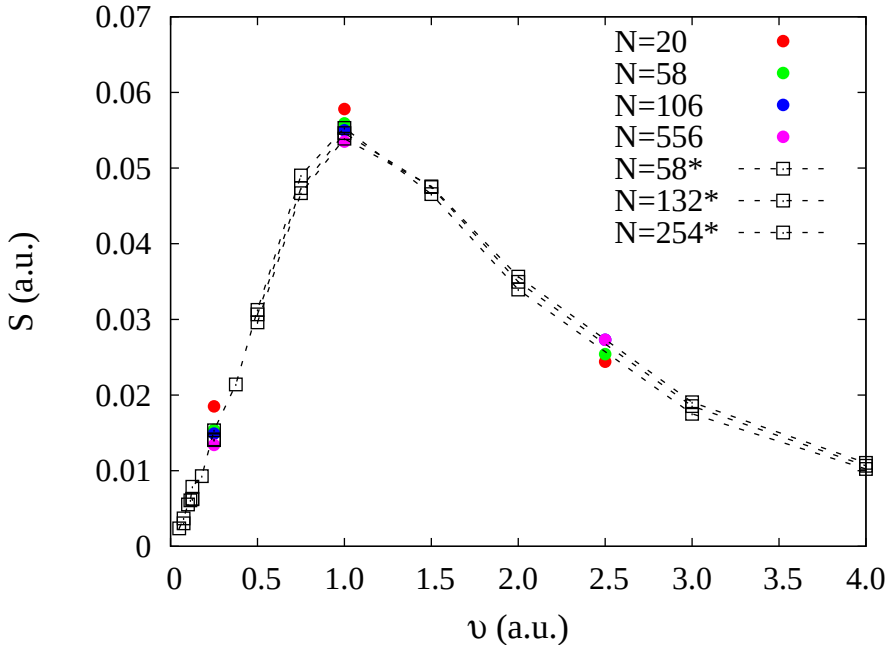

Figure 5.1: Stopping power of Na clusters for an antiproton as a function of velocity. The number of electrons in different clusters is indicated in the figure. The colored dots are the results of the present work. The results marked with a star (*) are taken from [5].

5.1 Dynamic screening and energy loss of antiprotons colliding with excited Al clusters

The achievements of TDDFT in the non-linear description of electronic excitations pave the way to answer new and challenging questions in the interaction of charged particles with condensed matter. In the traditional description of energy loss processes, the target is always considered as initially in its ground state. However, the energy lost by a travelling charge in a metallic medium should be affected by the electronic state in which the target is. Otherwise said, if electronic excitations have been already created in the system, the electronic response to the incident perturbation, and consequently the energy loss, will be different. In this section we try to quantify this difference for the particular case of a point charge crossing a metallic cluster of a few Å size.

We study the collision of a slow negative point charge (an antiproton) with an Al cluster. The choice of the antiproton as a projectile allows us to avoid complications related to the electron capture by the projectile if the latter is an ion. Our goal is to identify the distinct effects that arise in the dynamic screening and the projectile energy loss when the metallic target has been previously excited by a preceding projectile. In spite of the fact that our model is simplified, the results of our study can contribute to the understanding of the fundamentals of the dynamical processes during collision of charged particles with metallic systems.

We perform an explicit time propagation of the electronic state of the system and evaluate the energy lost by the charge when crossing ground-state clusters. We compare this quantity with the amount of energy lost when the projectile crosses a cluster excited from a previous collision. We show that the difference is appreciable and explain this change as a consequence of the excited state of the cluster as well as of the emission of electronic charge from the excited cluster.

Non-linear effects in the excitation of metal clusters have been previously analyzed with TDDFT. In particular, electron dynamics in clusters under intense laser fields is an active hot topic of research [97] because of the possibilities offered to explore and control ultrafast processes. The resonance energy of collective excitations (plasmons) in these systems has been shown to depend on the intensity of the perturbation [98]. Here we focus on a different type of external perturbation, namely, that derived from a point Coulomb charge crossing the system. We

will show, nevertheless, that similar shifts in the position of the plasmon peaks are found.

We study the energy loss in two different motion cycles. In the first cycle, the antiproton moves towards the cluster with a constant velocity v, crosses it following a symmetry axis through the cluster center, and eventually moves away until it reaches a turning point arbitrarily defined. The turning point is at a distance from the cluster far enough not to have any residual interaction. The cluster is then left in an excited state. The electronic energy transferred to the cluster during the collision is calculated. In the second cycle, the antiproton turns back from the turning point and starts to approach the excited cluster with the same constant velocity v. In the second crossing of the cluster, the latter now in an excited state, energy is again transferred to the cluster. We calculate the energy lost in this second cycle and compare the obtained value with that of the first cycle.

5.1.1 Results

We have chosen a small Al ($r_s = 2.07$) cluster with $N = 18$ electrons and with radius $R_{cl} = 5.43$ a.u. (≈ 0.29 nm). The projectile velocity is $v = 0.5$ a.u. The ALDA-TDDFT method used here predicts very well the energy loss of antiprotons in Al targets. The method gives very good agreement with measurements in Al bulk for antiproton velocities up to 1.8 a.u. Above this velocity the excitations of the inner shells in Al start to contribute to the energy loss and results deviate from the experimental ones [6].

The antiproton starts its motion at time $t = 0$ from the position $z_0 = -50$ a.u. After the first collision, the projectile continues to move until $t = 1000$ a.u. At this time the second cycle starts and the antiproton takes the way back to collide again with the cluster (see scheme in Fig. 5.2). In both cycles we calculate the force $F_z(t)$ experienced by the projectile due to the interaction with the cluster:

$$F_z(t) = 2\pi \int \rho d\rho dz \frac{n(\rho, z, t) - n_0^+(\rho, z)}{[(z_{ap} - z)^2 + \rho^2]^{3/2}} (z_{ap} - z). \tag{5.1}$$

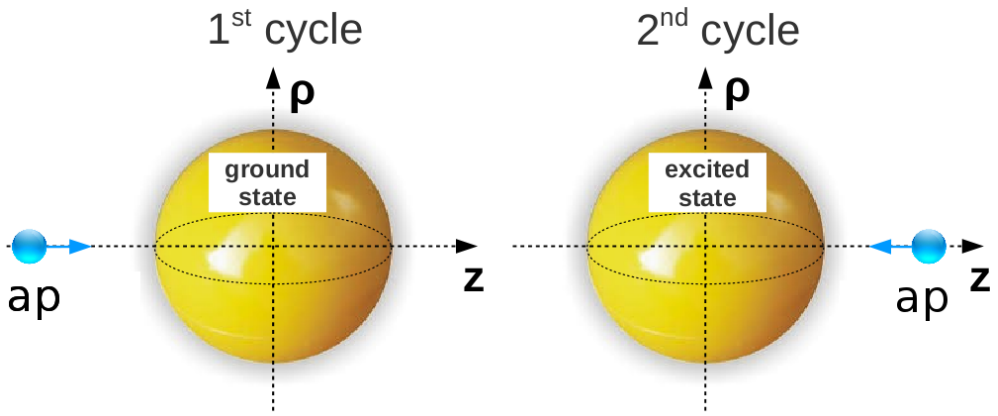

Figure 5.2: Schematic view of the collision process for an antiproton traversing an Al cluster in the ground state in the first cycle and then turning back and traversing again the cluster, now excited, in the second cycle.

From $F_z(t)$ we obtain the value of the energy lost by the antiproton E_{loss}:

$$E_{\text{loss}} = -v \int_0^{\infty} F_z(t) dt. \tag{5.2}$$

In these equations, we follow the notation of Chapter 3. In addition, we consider three other different time spots τ for the second cycle to start: 1003.5, 1005, and 1010 a.u. The purpose of using different time delays is to check the sensitivity of the final result to the dynamics followed by the electron density in the cluster excited state. With our choice of time delays, the antiproton reaches the excited cluster respectively $\Delta\tau = 7$, 10 and 20 a.u. of time later than in the reference calculation. Depending on the value of $\Delta\tau$, the antiproton will start to cross the surface of the excited cluster meeting a minimum or a maximum in the electronic density oscillations, or an intermediate state. The density oscillations will be discussed later. The results for the energy loss are summarized in Table 5.1.

Table 5.1: Energy loss E_{loss} (in a.u.) of an antiproton crossing the spherical Al cluster in the ground state or in an excited state.

	1st collision	2nd collision $\Delta\tau = 0$	2nd collision, $\Delta\tau = 7$ au	2nd collision, $\Delta\tau = 10$ au	2nd collision, $\Delta\tau = 20$ au
E_{loss}	0.8527	0.7583	0.8318	0.8099	0.7554

The first interesting conclusion of the results of Table 5.1 is that the energy loss of the antiproton crossing the excited cluster is consistently lower than the

corresponding value for the antiproton colliding with the cluster in the ground state. There are two reasons for the decrease of the energy loss. One reason is that, after the first collision, the cluster has emitted an amount of electronic charge that roughly corresponds to one electron. This means that during the second collision the antiproton is interacting with a smaller number of electrons and therefore loses less energy. In order to check the relevance of the change in the electronic charge of the cluster, we performed an additional calculation, namely that of the energy loss in a positively charged cluster which contains 17 electrons and is in its ground state. The obtained value of 0.8211 a.u. is lower than the value of the energy loss in the neutral cluster, which is given in the Table 5.1 and is equal to 0.8527 a.u. The difference between these two results is around 4%. However, the difference is not as big as in the case of time delays $\Delta\tau = 0$ and 20 a.u. given in the table, which is up to 11% of the value of the energy loss in the first collision. This allows us to conclude that the emission of one electron from the cluster only partially explains the observed decrease of energy loss in the second collision.

Another reason for the lowering of the energy loss is that the cluster has been excited after the first collision with the antiproton. Namely, the electronic density of the cluster is starting to oscillate in time with a given frequency. As we mentioned before, depending on the value of the time delay $\Delta\tau$, the antiproton meets different spacial locations of the electronic density oscillations at the surface of the cluster in the second collision.

The total forces F_{z} experienced by the antiproton during the first collision and during the second collision at different time delays $\Delta\tau$ are shown in Fig. 5.3 as a function of the projectile position. Large negative values of z_{ap} correspond to positions of the antiproton before each collision with the cluster. The two strong features in F_z correspond to the antiproton crossing the cluster surface. Away from the cluster, the antiproton is attracted by the induced dipole. Inside the cluster, the electronic density rearranges in order to screen the strong perturbation created by the moving antiproton. The force inside the cluster oscillates about a mean value that roughly corresponds to the effective stopping power for this particular velocity of the projectile ($v = 0.5$ a.u.) [5].

For different time delays $\Delta\tau$ of the second collision, the values of the energy loss slightly vary. These differences are due to the different forces experienced by the antiproton (Fig. 5.3). In order to illustrate this, we show the difference

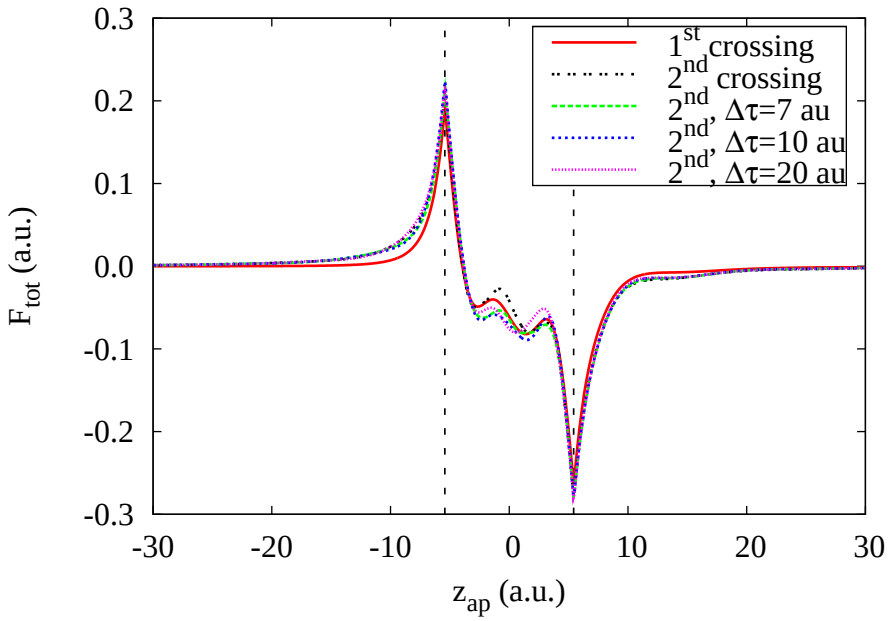

Figure 5.3: Force on the antiproton colliding with the cluster, F_z, in the first cycle and in the second cycle for different time delays τ between collisions as a function of the projectile position z_{ap}. Dashed lines show the borders of the cluster (R_{cl} = 5.43 a.u.).

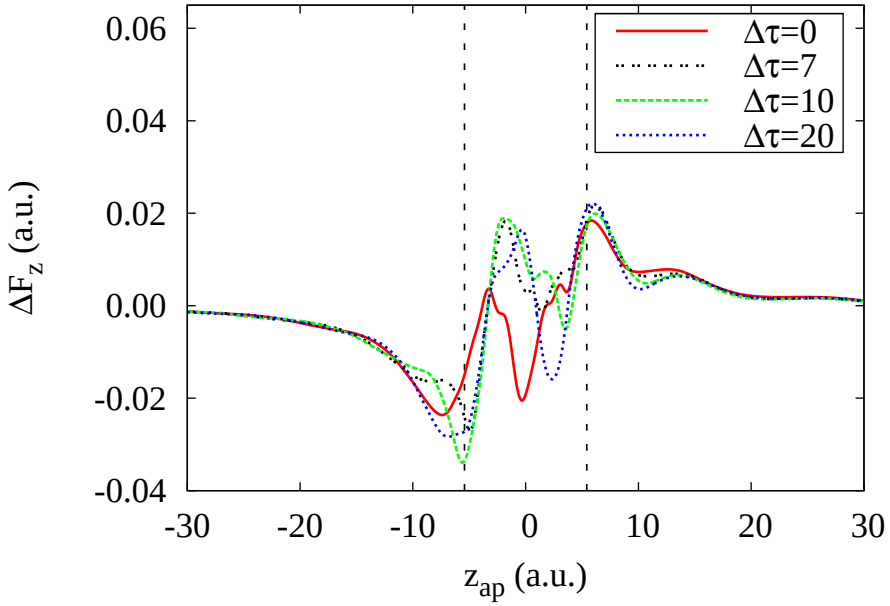

Figure 5.4: Difference in the force between the first and second collision of the antiproton with the cluster, ΔF_z, for different time delays τ between collisions as a function of the projectile position z_{ap}. Dashed lines show the borders of the cluster (R_{cl} = 5.43 a.u.).

in the force between the first and the second collision $\Delta F_z = F_z^{1st} - F_z^{2nd}$ for different values of $\Delta\tau$. Here F_z^{1st} is the force felt by the moving charge colliding with the non-excited metal cluster, which is equal for all τ; F_z^{2nd} is the force felt by the antiproton colliding with the excited cluster. ΔF_z is shown in Fig. 5.4 as a function of the antiproton position. The curves in Fig. 5.4 show how the force felt by the antiproton changes depending on the time at which the second collision starts.

We can also analyze the different values of the energy loss at different time delays $\Delta\tau$ looking at the total energy of the cluster. We show the energy in Fig. 5.5 as a function of the antiproton position. From Fig. 5.5 we can see that the total energy of the cluster is increased by the collision. This increase in energy is the value of the energy transferred by the antiproton to the cluster or, in other words, the energy lost by the antiproton. We can see as well that, in all cases, the energy loss after the second collision is lower than after the first collision. The curves for $\Delta\tau = 0$ and for $\Delta\tau = 20$ a.u. are similar. This is consistent with the values of the energy loss given in Table 5.1 for these two cases. We can also see the longer range of the cluster-antiproton interaction during the second collision. This is due to the net positive charge of the excited cluster.

We can understand the dependence of the energy loss on the time delay between collisions by looking at the time evolution of the induced electronic density. Figure 5.6a shows the change in electronic density $\Delta n(z, \rho = 0, t) = [n(z, \rho = 0, t) - n(z, \rho = 0, t = 0)]$ inside the cluster in units of the background density n_0, along the $z-$axis and as a function of time. The results are shown for the calculation with $\Delta\tau$ =0. The time interval in Fig. 5.6a is chosen to include the moment at which the second collision of the antiproton with the cluster takes place. In the figure, the projectile moves from the right to the left. The second collision starts at $t \approx 1890$ a.u. We clearly see the negative change in density, originated by the Coulomb repulsion between the incident antiproton and the cluster electrons. From Fig. 5.6a we can see that the excitation created by the moving charge in the cluster after the first collision leads to oscillations in the induced electronic density: minima and maxima in the induced density are observed before the second collision. Depending on the time delay between collisions $\Delta\tau$, the impact of the incoming antiproton with the previously excited cluster can bump into a minimum or a maximum of the electronic density oscillations. In the first calculation ($\Delta\tau = 0$) and when the time delay is $\Delta\tau = 20$ a.u., the antiproton starts to cross

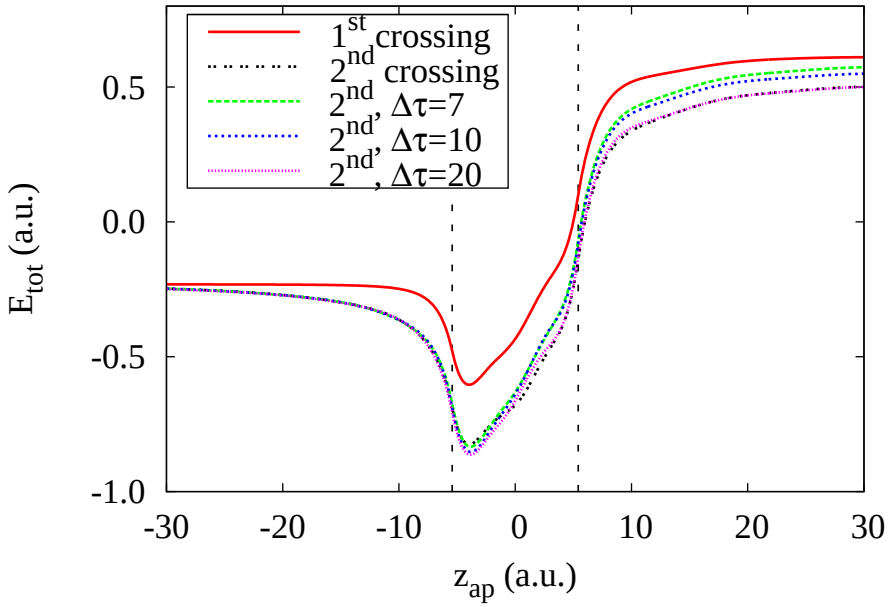

Figure 5.5: Total energy of the cluster E_{tot} for different collisions and for different time delays $\Delta\tau$, as a function of the antiproton position z_{ap}. All the energy curves corresponding to the second crossing are referred to the value of the energy prior to the first crossing when antiproton is far from the cluster. Dashed lines show the borders of the cluster ($R_{\text{cl}} = 5.43$ a.u.).

the excited cluster when there is a maximum in the electronic density oscillations at the surface of the cluster (the change in density in Fig. 5.6a is positive). In the case of $\Delta\tau = 10$ a.u. the second crossing finds a minimum of the electronic density oscillations at the cluster surface. The time delay $\Delta\tau = 7$ a.u. is chosen to have a case in which the second crossing falls neither on the minimum nor on the maximum of the change of the electronic density but in-between these two situations. Depending on this circumstance, the value of the energy lost by the antiproton varies.

From Fig. 5.6a, we can also see that the minima and maxima in the induced electronic density become more pronounced after the second collision, indicating that the cluster is further excited by the second collision. This can also be seen in Fig. 5.6b where the change in density is shown as a function of time for the particular value of $z = 4$ a.u., marked with a dashed line in Fig. 5.6a. The amplitude of the electronic density oscillations increases after the second collision. This is also observed in Fig. 5.6c and Fig. 5.6d where we illustrate the density distribution in the cluster before ($t = 1812$ a.u.) and after ($t = 1992$ a.u.) the second collision. The change in density is plotted in a plane in

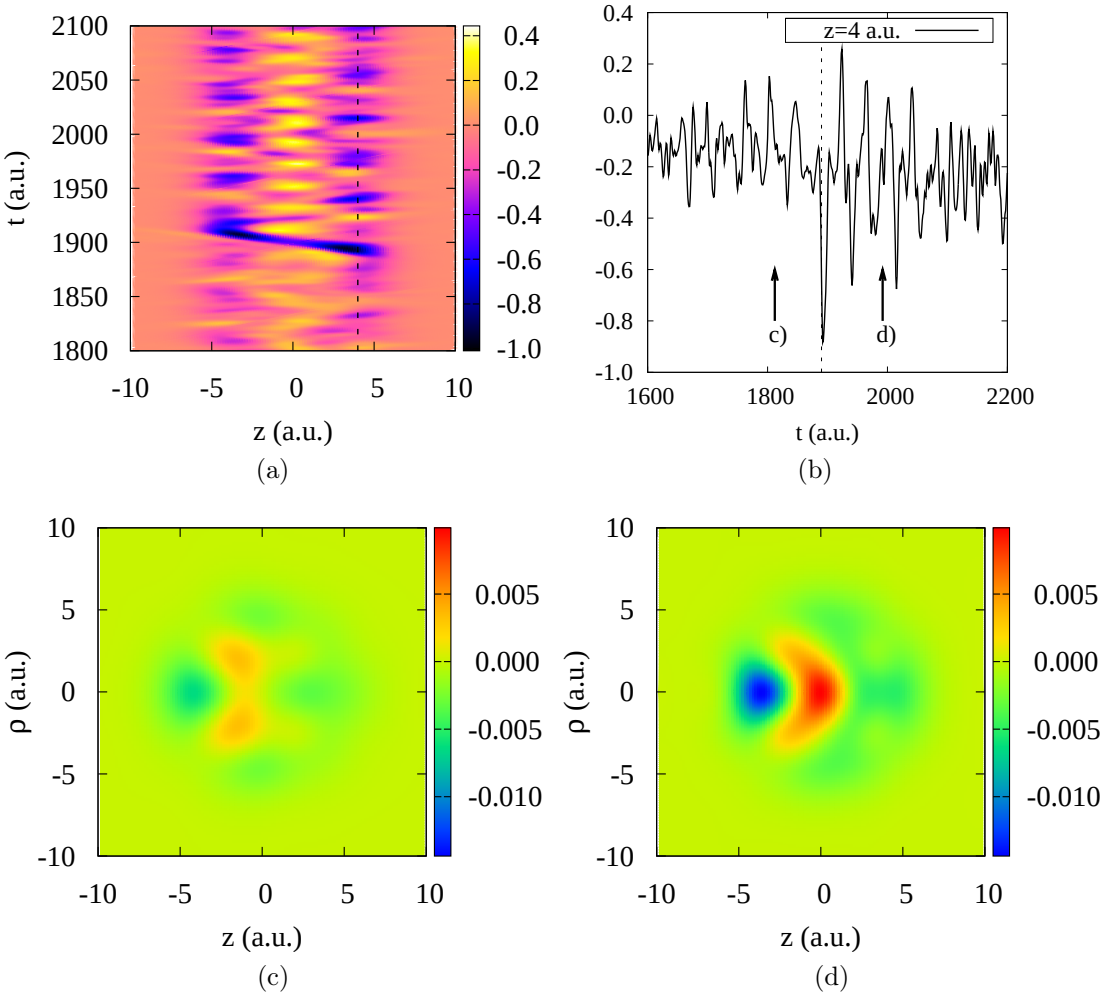

Figure 5.6: (a) Time evolution of the induced electronic density inside the cluster along the $z-$axis ($\rho = 0.02$ a.u.) including the time at which the antiproton crosses the excited cluster. The color code shows the change in density $[n(z, \rho = 0, t) - n(z, \rho = 0, t = 0)]$ in units of the background density n_0. The dashed line in panel (a) indicates the position $z = 4$ a.u., for which, in panel (b), we show the change in density as a function of time. Dashed line in panel (b) indicates the moment when the second collision starts. (c) and (d) show the change in the electronic density $[n(\mathbf{r}, t) - n(\mathbf{r}, 0)]$ of the spherical cluster (color codes) in (ρ, z) coordinates at times $t = 1812$ a.u. and $t = 1992$ a.u. respectively.

(ρ, z) coordinates with the center of the cluster at $(\rho = 0, z =0)$. The negative and positive peaks in the right panel (Fig. 5.6d) are much more intense than in the left panel (Fig. 5.6c). These pronounced oscillations show that, after the second collision, the oscillations of the induced electronic density are stronger. The excitation created by the second antiproton enhances that created during

the first collision. However, the similar distribution of the induced charge seems to indicate that similar electronic modes are excited in both events.

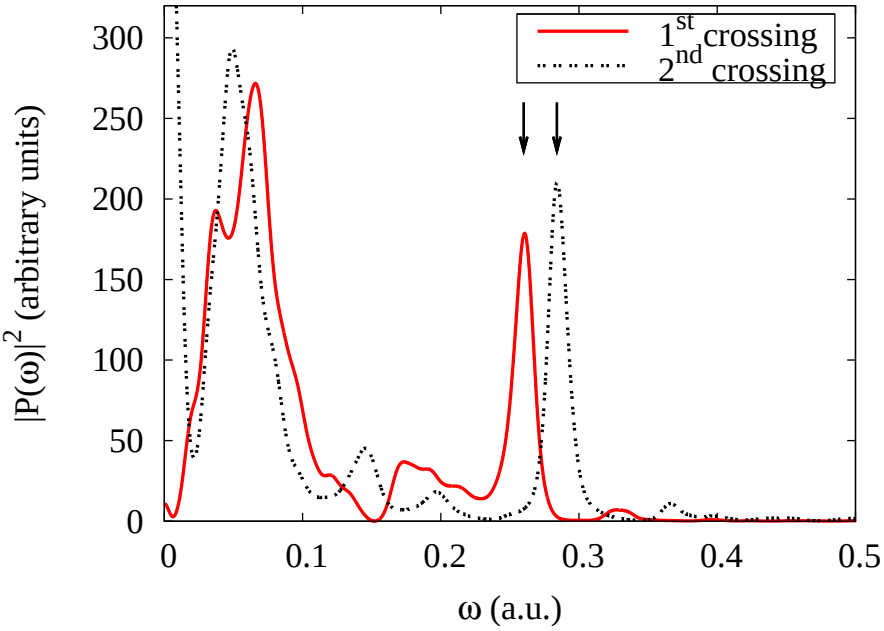

Figure 5.7: Dipole power spectra $|P(\omega)|^2$ (arbitrary units) for the excited cluster after one collision (red solid line) and after two collisions (black dashed line). Frequency is shown in a.u.

In order to calculate the frequency of the density oscillations we perform a Fourier analysis of the time evolution of the dipole moment $P(t) \rightarrow P(\omega)$ created by the electronic density in the excited cluster. The Fourier transform is done for two different cases: a) after one single collision and without including the second collision, and b) after the two collisions. In this analysis we use the time evolution of the dipole during ∼1200 a.u after each collision and an exponential mask function (centered in the middle of such interval) to avoid spurious effects due to the use of finite time interval. The results for the respective dipole power spectra $|P(\omega)|^2$ are shown in Fig. 5.7. Two peaks are shown by arrows at frequencies $\omega =$ 0.261 and 0.284 a.u. (corresponding periods of these frequencies are $T \approx 24.1$ and 22.1 a.u.). They roughly correspond to the expected value of the plasmon energy in the cluster: We calculate the plasmon frequency for a perfect metal sphere from the value of the density n_0 as $\omega_s = \omega_p/\sqrt{3} = \sqrt{4\pi n_0/3}$ (Mie resonance frequency), which is generally referred to as a surface plasmon [74]. For an Al cluster ($r_s = 2.07$) this value is $\omega_s = 0.34$ a.u. In our calculations the obtained frequency is lower than the frequency given by the classical Mie theory. This

is due to the small size of the cluster and because we use quantum theory for the calculation of the frequency. A red shift with respect to its classical Mie value is frequently observed in clusters of simple metals [22, 72, 99, 100]. In Fig. 5.7 we also see that the plasmon peak is shifted to higher frequencies after the second collision. This behavior is consistent with the non-linear shift of the plasmon frequency under non-perturbative conditions [98]. The blue shift of the frequency after the second collision is in part related to the emission of electronic charge from the cluster due to the interaction with the antiprotons. It was observed that the resonance position moves to higher frequencies when increasing the positive charge of the cluster [100]. Both the non-perturbative effect and the charged-cluster effect hence contribute to the blue shift of the plasmon frequency. Lower-energy excitations are also present in the spectra and can be attributed to excitations of electron-hole pair character [98].

5.1.2 Conclusions

In summary, we have calculated the energy loss of an antiproton colliding with a small Al cluster, both when the cluster is in the ground state and when the cluster is in an excited electronic state. We have shown that the antiproton loses less energy when penetrating a cluster previously excited. The lowering of the energy loss is related not only to the fact that the cluster is transferred to an excited state, but also to the fact that the cluster loses one electron during the first collision with the antiproton.

We have also shown that the projectile creates a plasmon in the cluster and that the plasmon peak shifts to higher frequencies in the second collision. This corresponds to the observed larger amplitude of the electron density oscillations in the cluster after the second collision of the antiproton with the cluster. The shift of the plasmon peak to higher frequencies is partially due to the emission of one electron from the cluster, which thus becomes positively charged.

5.2 Vicinage effect in the energy loss of antiprotons traversing Na and Al clusters of different sizes

Until now we considered only the interaction of a single projectile with a target. Indeed, if, in a given experiment, the projectiles are sufficiently separated among each other, each collision can be treated separately. Under such conditions there is no interference between the interactions of different particles with matter. However, if the projectiles move through the solid in close proximity to each other, they will interact in a combined way with the target electrons. In this case new physical phenomena can appear.

The difference between twice the energy loss of a single particle interacting with a target and the energy loss of two particles, traveling in close proximity to each other, is usually called in this context the *vicinage effect*. In this section, we use TDDFT to study the vicinage effect in the energy loss of two antiprotons. We analyze in detail the energy loss of each antiproton individually and we show that under certain conditions the second antiproton is accelerated while the first one is slowed down. This leads to an effective attraction between the antiprotons due to the dynamic screening of the antiprotons inside the cluster.

One interesting phenomenon arising from the correlated motion of charges through the solid is the pairing of particles. This is in a way related to the formation of the so-called Cooper pairs in superconductivity – pairs of electrons bound together due to attractive forces originated by the dynamic polarization of the solid. In our study the pair of antiprotons is formed because of a similar reason. The antiprotons moving inside the metal cluster polarize the metallic medium. As a result the Coulomb potentials of the antiprotons are completely screened at long distances. The polarization leads to the appearance of an oscillating effective potential between the antiprotons with attractive regions. The difference between our system and the Cooper pairing of electrons is that our particles are external to the metallic target. Additionally, for standard superconductors, the mechanism for pairing is related to the excitation of phonons in the solid, while here we only consider the effect of the screening by the valence electrons of the metal. An additional difference is the mass of the particles, since the antiprotons are almost 2000 times heavier than the electrons.

Another interesting analogy is the formation of dust clusters in plasma physics. Clusters of dust particles of the same charge can be formed due to the effective attractive forces in plasmas [101, 102]. The origin of the dust-dust attraction is the wake behind the dust originated by the ion flow over the dust grain. In our case, at high velocities of the antiproton inside the cluster, the screening cloud has the form of a wake, since the cluster electrons are too slow to be able to rearrange in response to the antiproton's movement. The dust-dust interaction is a complex phenomenon, which is very important in the physics of dusty plasmas. Our study may be therefore useful to understand how the dynamic screening of massive particles in electronic media can influence the correlated motion of these particles under different conditions.

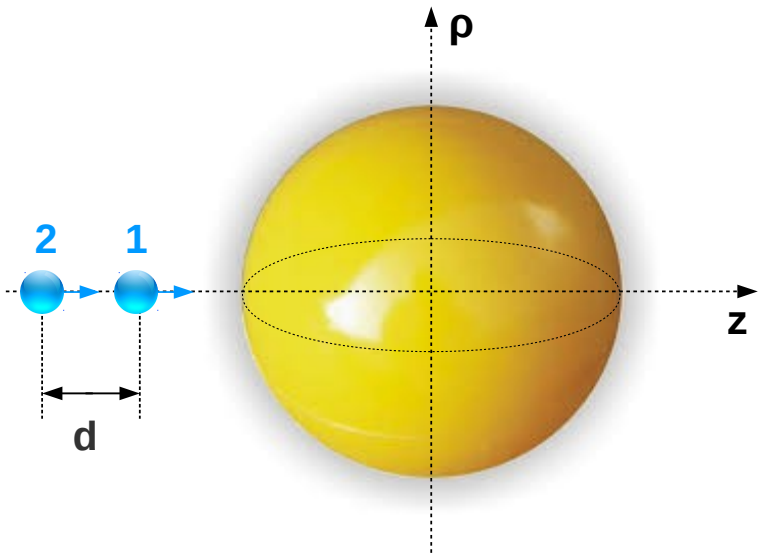

Figure 5.8: Sketch of the process treated in this section. Two antiprotons move at a distance d from each other and cross the spherical cluster through the geometrical center.

Here we consider as targets three sodium clusters with 20, 106 and 1074 valence electrons, and two aluminum clusters with 18 and 556 electrons. The antiprotons are chosen as projectiles and are modeled as negative (Q $= -1$) point charges. Initial positions of the projectiles are at distances z_0 and $(z_0 + d)$ from the cluster center, such that the interaction with the cluster is negligible. The antiprotons move along the $z-$axis at a distance d from each other and cross the cluster through the geometrical center (see scheme in Fig. 5.8).

We perform our calculations in two different approximations. In the first

approximation, we consider that the two charges move with constant velocity v at a constant distance d from each other. We calculate the force on each antiproton F_z from the equation (5.1) at every time step of the propagation. From the force we obtain the energy loss of each antiproton using equation (5.2). The average energy loss per unit path length inside the cluster is the average stopping power of the material:

$$S = \frac{E_{\text{loss}}}{2R_{\text{cl}}}. \tag{5.3}$$

The constant velocity approximation allows for the analysis of the velocity dependence of the energy loss.

In the second approximation, we perform the real dynamics of two antiprotons in the cluster. In this case we allow for the velocity to change according to Newton's equations of motion, including the Coulomb repulsion between the projectiles. The antiprotons start to move with initial velocity v_0 at a distance d_0 between them. Then we look at how velocities of both particles and the distance between them evolve in time, depending on the initial conditions.

5.2.1 Induced density and forces

When two antiprotons move through the cluster, the electronic density of the cluster starts to rearrange in order to screen the negative charges of projectiles. To illustrate the process under study, we show in Fig. 5.9 the snapshots of the change in electronic density of the cluster perturbed by one or two antiprotons. In Fig. 5.9a the change in the density is induced by one antiproton moving with velocity $v = 1$ a.u. In Fig. 5.9b the change in the density is induced by two antiprotons moving with velocity $v = 1$ a.u. at a distance $d = 22$ a.u. between them. From both plots we can see that the antiprotons moving with velocity 1 a.u. (twice the Fermi velocity for Na, $v_{\text{F}} = 0.48$ a.u.) create a wake pattern behind them. From Fig. 5.9b we can see that, in this particular case, the second antiproton will experience a larger stopping force than the first one, because of the large accumulation of electrons on its' way. This is conspicuous as well if we compare the forces acting on both antiprotons.

In Fig. 5.10 we show the total force acting on the moving antiprotons during the collision process as a function of time. As it was previously mentioned, the up and down peaks correspond to the crossing the surface in and out of the cluster,

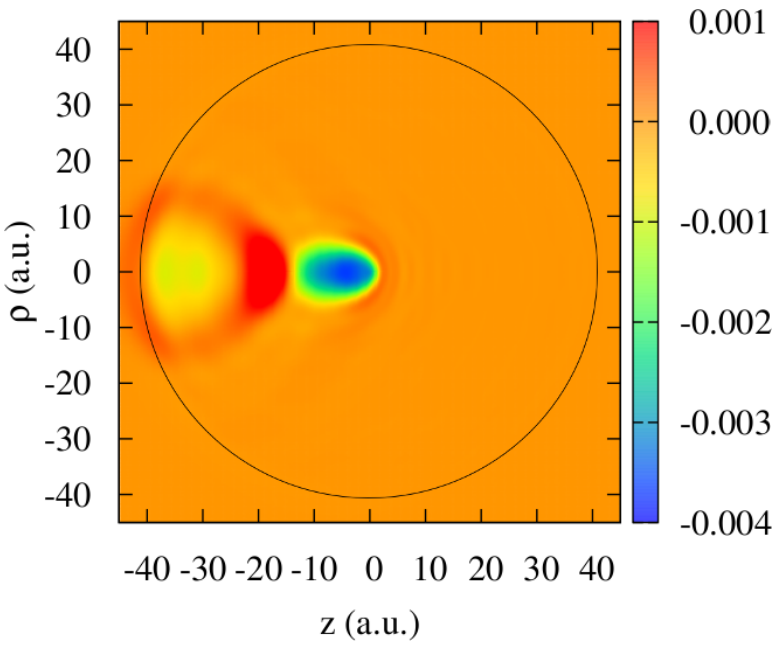

(a)

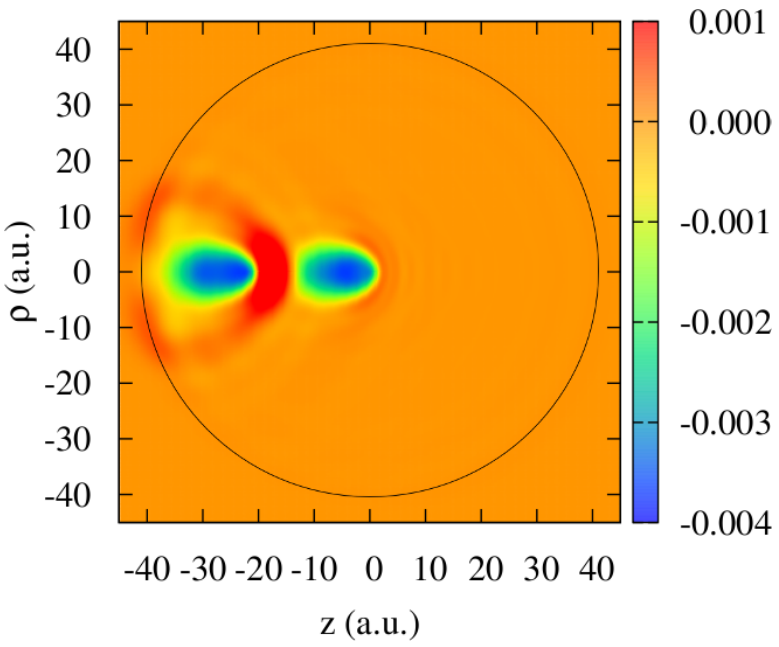

(b)

Figure 5.9: Snapshots of the induced electronic density inside the Na_{1074} cluster in response to the movement of a) one antiproton and b) two antiprotons ($d = 22$ a.u.), in (z, ρ) coordinates. Velocity of antiprotons is 1 a.u. Black line shows the cluster border.

because we include the effect of the positive background in the force. Inside the cluster the force is roughly constant and corresponds to the average stopping power of the metal.

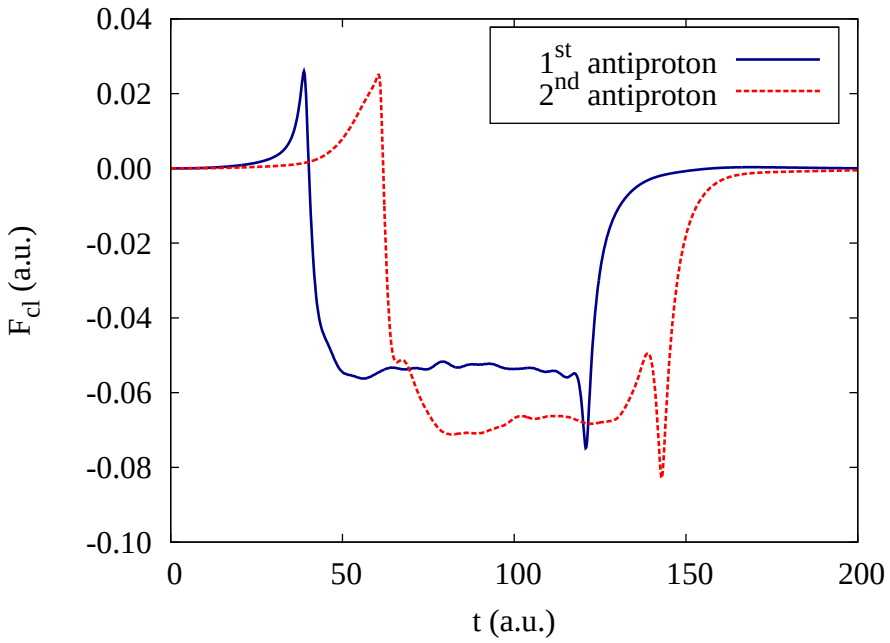

Figure 5.10: Cluster-induced force acting on the antiprotons traversing a Na_{1074} cluster as a function of time. Distance between the antiprotons is $d = 22$ a.u, velocity is $v = 1$ a.u. Radius of the cluster is 40.96 a.u.

As was expected, the antiprotons experience different forces. The first antiproton enters the cluster when the cluster is in the ground state and creates electronic excitations in the cluster which in turn have an influence on the second antiproton. This influence strongly depends on the time delay between the entrance of the first antiproton and the entrance of the second antiproton in the cluster, or in other words, on the distance between them. The velocity of the moving particles is also an important parameter. In the particular case of the distance $d = 22$ a.u. between the antiprotons, moving with velocity $v = 1$ a.u. (Fig. 5.10), the second one experiences a larger stopping force than the first one. This results in a larger energy loss of the second antiproton. We will show that, depending on the inter-particle distance, the energy loss of the first antiproton can be larger or smaller than the energy loss of the second one.

In the next subsection, we analyze in detail the vicinage effect in the energy loss of two antiprotons travelling at different distances from each other through Na clusters of different sizes. The influence of the velocity is investigated. For

the sake of comparison we show the results for the vicinage effect in Al as well, for one particular velocity.

5.2.2 Vicinage effect in the constant velocity approximation

The quantity of interest to measure the vicinage effect in the energy loss of two particles is the *stopping power ratio*. In our particular system, the stopping power ratio is the ratio between the total stopping power of the cluster for two antiprotons S_{1+2} and twice the stopping power for a single antiproton S_{single}:

$$R = \frac{S_{1+2}}{2S_{\text{single}}}. \tag{5.4}$$

In Fig. 5.11 we show the stopping ratio as a function of the inter-particle distance for two antiprotons moving through Na clusters with 20, 106 and 1074 electrons. We consider three different velocities of the antiprotons to explore: a) the low velocity regime ($v = 0.5$ a.u.), in which the stopping power in metallic media is linear with velocity; b) the intermediate regime ($v = 1$ a.u.), in which the maximum of the stopping power in Na appears, and c) the high velocity regime ($v = 2$ a.u.), for which linear theory should be applicable.

In all the results presented in Fig. 5.11 the stopping ratio has a similar behavior as a function of d. Starting from $R > 1$ at $d = 0$, it then decreases and has a minimum, which is different for different velocities. After the minimum, the stopping ratio increases and at large d is approaching (or is oscillating around) the value of $R = 1$.

In the analysis of the stopping power ratio we have to take into account two limits for the distance d between the antiprotons. When the distance $d \to 0$, the two particles move as one particle with charge $Z = -2$. In linear theory the stopping power scales as Z^2. This means that in the limit of high velocity (linear regime) the stopping ratio R for $d = 0$ should converge to $R \approx 2$. In Fig. 5.11(c) we see that at velocity 2 a.u. and at distance $d = 0$ the stopping ratio almost reaches the limit of the linear theory. However, at lower velocities, where non-linear effects are important, the value of R at $d = 0$ is different.

When the distance is very large ($d \to \infty$), there is no interference in the interactions of the antiprotons with the electronic medium of the cluster. Therefore

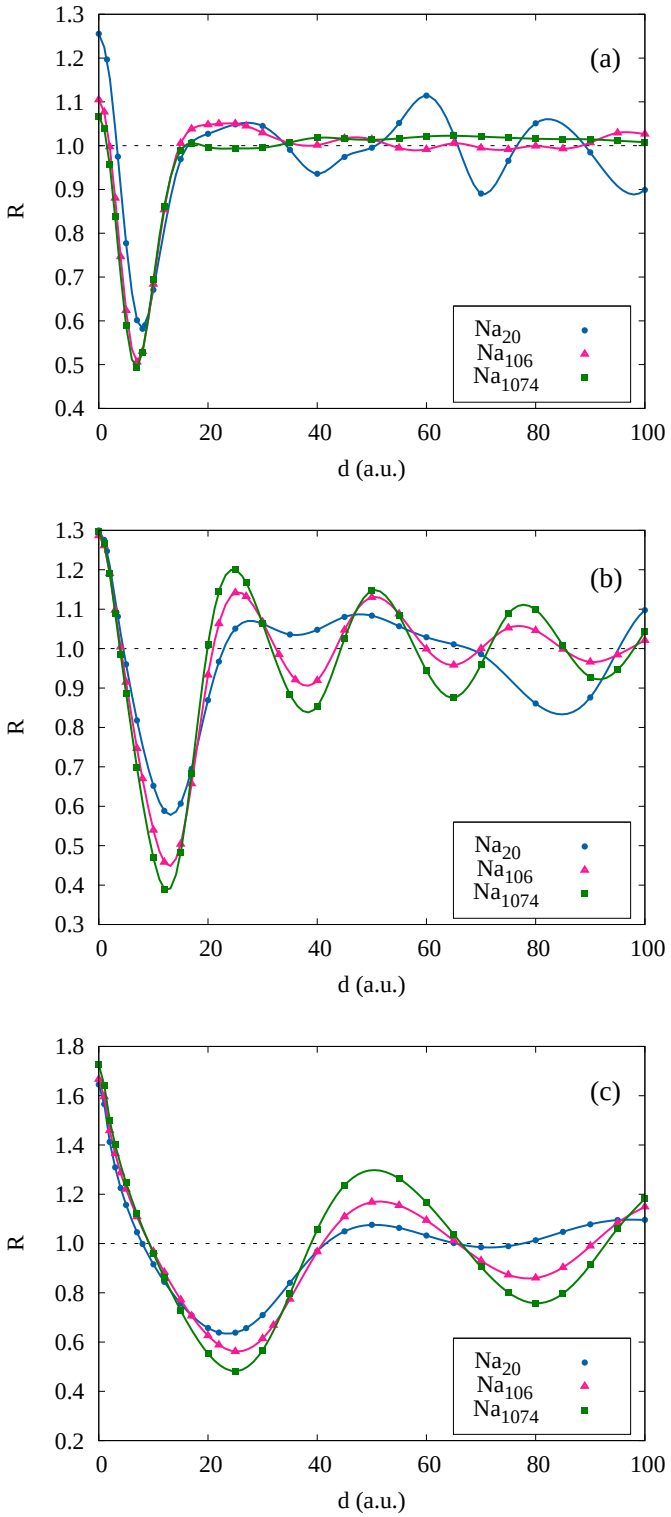

Figure 5.11: Stopping power ratio, R, in Na clusters as a function of the interparticle distance d. Velocities of the antiprotons are: (a) 0.5 a.u, (b) 1 a.u., and (c) 2 a.u. Points show the calculated data and solid lines show the numerical interpolation.

the stopping power of each antiproton should be equal to that of the single antiproton and the stopping ratio should converge to 1. We see that at velocity 0.5 a.u. (Fig. 5.11(a)), at large distances between the projectiles, the stopping ratio is roughly equal to 1, except for the case of the smallest Na_{20} cluster. In such a small jellium cluster the quantum size effects play an important role. For a small Na_{20} cluster, the dynamics after collisions always corresponds, even at low velocities, to the creation of a few excitations with well-defined energies (frequencies). For larger clusters, however, we excite many more different transitions and there is not a well-defined oscillatory behavior until we are able to excite the plasmon, which is a well-defined collective excitation of the whole cluster.

At larger velocities $v > v_F$ (Fermi velocity in Na is 0.5 a.u.) the stopping ratio oscillates around one. The oscillations have the same amplitude for the clusters Na_{106} and Na_{1074}, and the amplitude is twice larger in the case of $v = 2$ a.u, as compared with the case of $v = 1$ a.u. This means that the oscillations are characteristic for this particular metal, and are not determined by the finite size of the cluster. The frequency of the oscillations is the same as the frequency of the collective charge density oscillations (discussed later, Fig. 5.14). This allows us to conclude that the origin of the oscillations of the stopping power ratio is the excitation of the plasmon mode created in the cluster by the moving antiprotons. The bulk plasmon frequency of an electron gas with a given r_s is calculated as $\omega_p = \sqrt{3/r_s^3}$. In the case of Na ($r_s = 4$ a.u.) this nominal value is equal to $\omega_p \approx 0.22$ a.u. Similarly, the frequency of the oscillations in our case is $\omega \approx 0.23$ a.u.

In Fig. 5.12 we compare the stopping power ratio, R, for two antiprotons moving through the Na_{1074} cluster with different velocities. The stopping ratio is shown as a function of the unitless parameter $d/v(T_p)$, where inter-particle distance d is divided by the velocity of the antiprotons v and by the period of plasmon oscillations $T_p = 2\pi/\omega_p$. For distances $d > 100$ a.u. the stopping power ratio is obtained by the fitting to an analytical function

$$R_{\text{fit}} = a_1 \exp(-a_2 d) \cos(\omega d + D_{\text{shift}}), \tag{5.5}$$

where ω is the frequency of the plasmon oscillations created in the cluster, d is the distance between the antiprotons, and the parameters a_1, a_2, and D_{shift} are chosen numerically to fit the calculated stopping ratio. Figure 5.12 better illustrates that at high velocities $v > v_F$ the frequency of the stopping power

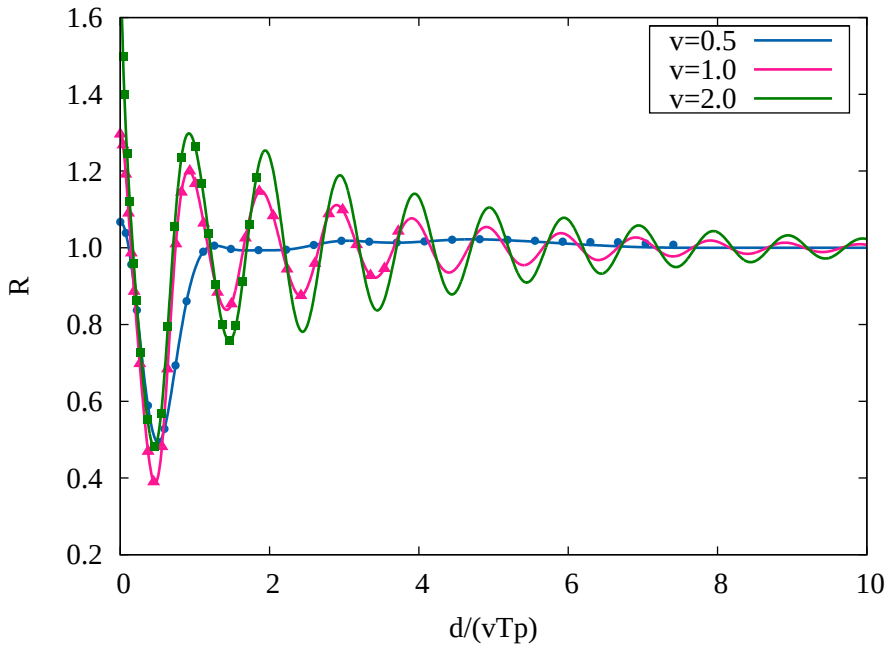

Figure 5.12: Stopping power ratio, R, for antiprotons in Na_{1074} cluster as a function of the parameter $d/(vT_p)$. Velocities of the antiprotons are 0.5, 1, and 2 a.u. Points show the calculated data and solid lines show the numerical interpolation for $d < 100$ and the fitting function for $d > 100$.

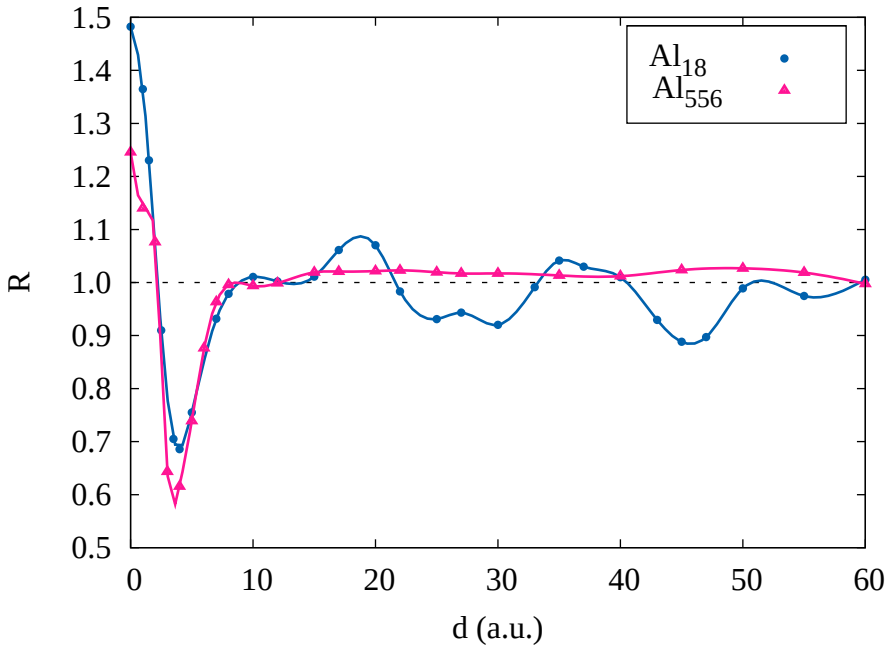

Figure 5.13: Stopping power ratio, R, for antiprotons in Al clusters as a function of the inter-particle distance d. Velocity of the antiprotons is 0.5 a.u. Points show the calculated data and solid lines show the numerical interpolation.

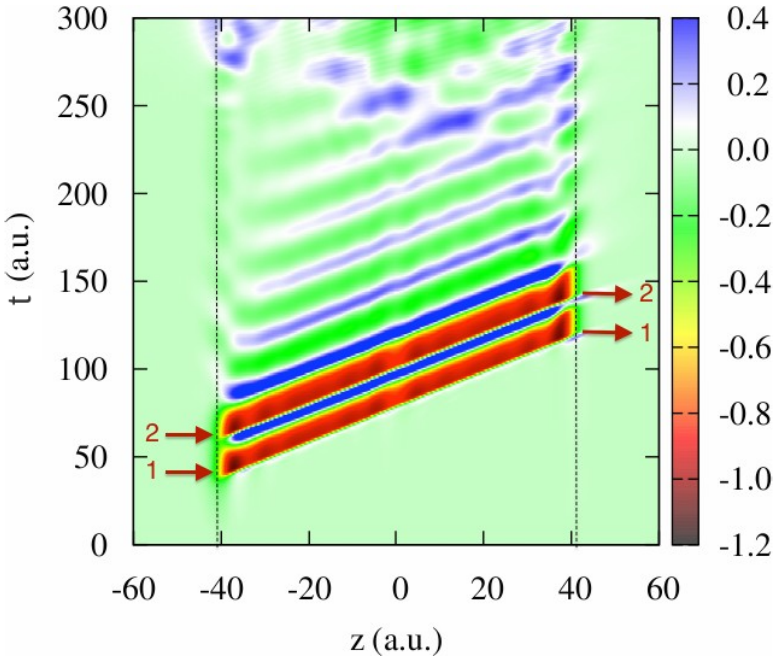

(a)

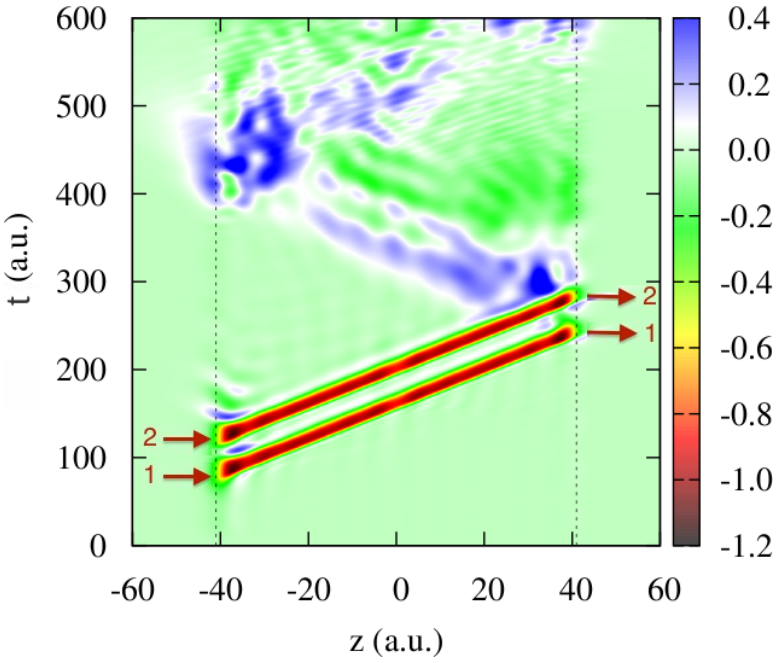

(b)

Figure 5.14: Change in electronic density, $\Delta n(z,t)$, of the Na_{1074} cluster along the $z-$axis induced by the moving antiprotons as a function of time. a) $d = 22$ a.u, $v = 1$ a.u. b) $d = 20$ a.u, $v = 0.5$ a.u. Radius of the cluster is 40.96 a.u. Arrows indicate when the first and the second antiprotons enter and leave the cluster.

ratio oscillations do not depend on the velocity of antiprotons.

We have also studied the vicinage effect in the energy loss of two antiprotons moving through Al clusters of two sizes: Al_{18} and Al_{556}. In Fig. 5.13 we show the stopping power ratio R for two antiprotons moving with velocity 0.5 a.u. The behavior is very similar to the one in Na clusters for the same velocity. Again, in the smallest cluster, we see some oscillations at large d due to the quantum size effects, but in the Al_{556} cluster the stopping ratio has almost no oscillations and it roughly equals $R \approx 1$.

The plasmon oscillations can be seen in Fig. 5.14(a), in which we show the time evolution of the electronic density along the $z-$axis. The time evolves along the vertical axis. The color code shows the change in electronic density normalized to the density of the positive background (3.2) and calculated at $\rho = 0.02$ a.u., i.e., the quantity $\Delta n(z,t) = [n(z,t) - n(z,t=0)]/n_0$. The two antiprotons move with constant velocity at a distance $d = 22$ a.u. from each other. The trajectories of both antiprotons inside the cluster are clearly seen in Fig. 5.14(a) as a large negative change in density. After both particles leave the cluster the latter is left in an excited state. The oscillations of the electronic density inside the cluster after the collision are the plasmon oscillations. If we look at panel (b) of Fig. 5.14, which corresponds to a velocity 0.5 a.u. ($\approx v_F$) of the antiprotons and a similar inter-particle distance $d = 20$ a.u., we can see that the plasmon oscillations do not appear. In this case we only find the creation of charge wave-front that is reflected back and forth between the cluster boundaries and moves roughly with the Fermi velocity of the system.

5.2.3 Particle-resolved analysis of the energy loss

We can analyze in further details the stopping power for each particle individually. In Fig. 5.15 we show the stopping power of the Na_{1074} cluster for the first (S_1) and for the second (S_2) antiprotons moving with velocity $v = 1$ a.u. as a function of the inter-particle distance d.

At short distances d, the stopping power for the first antiproton is larger, as compared with a single antiproton crossing the cluster. This is because the second antiproton, moving behind, pushes ahead electronic density, towards the first antiproton. The latter finds then a higher electronic density in its way and therefore is stopped more. As the distance between the antiprotons increases, the

difference between the stopping power for the first antiproton and for a single antiproton diminishes and at $d > D$ ($D = 82$ a.u. in this case) these quantities are equal.

The motion of the second antiproton is affected by the plasmon created in the cluster by the first antiproton. From Fig. 5.15 it is clear that the oscillations observed in the total stopping ratio (Fig. 5.11 (b) and (c)) are due to the stopping of the second antiproton. At large d the stopping power for the second antiproton S_2 oscillates with the plasmon frequency around S_1. At short distances d, the stopping power for the second antiproton is smaller than for the first one and at some d it even becomes negative. This means that, at some distances from the first antiproton, the second one can be accelerated instead of being slowed down. In the particular case of the velocity 1 a.u, shown in Fig. 5.15, the minimum of the stopping power is around $d = 12$ a.u. The second antiproton is accelerated because the first antiproton repels the electrons of the cluster from its path, leaving behind an area of positive charge that attracts the second antiproton. Otherwise said, the second antiproton is affected by the attractive part of the wake created by the first antiproton.

We have shown in Fig. 5.14 the change in the electronic density of the cluster

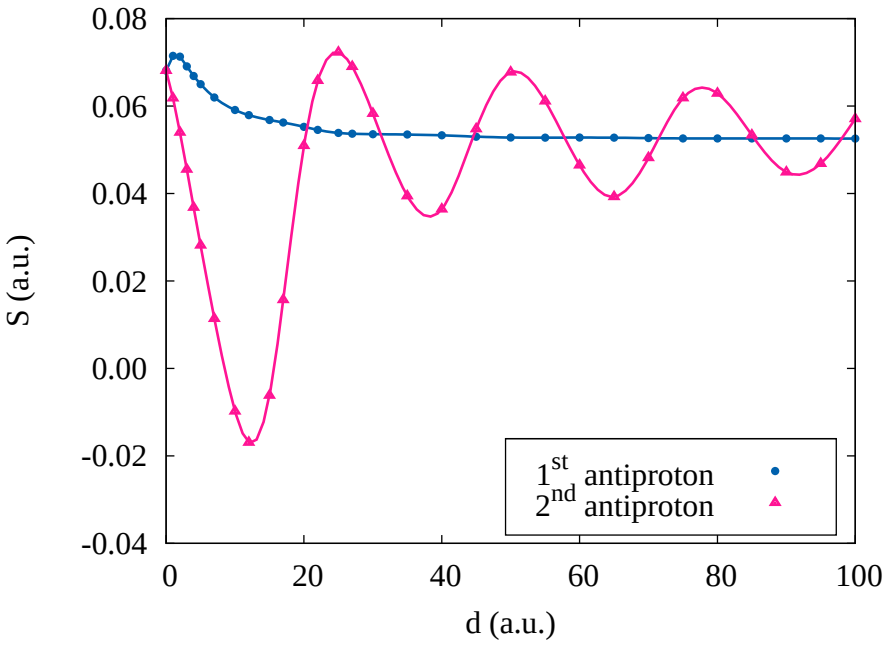

Figure 5.15: Stopping power of the Na_{1074} cluster for the first and the second antiproton moving with velocity $v = 1$ a.u. as a function of the inter-particle distance d.

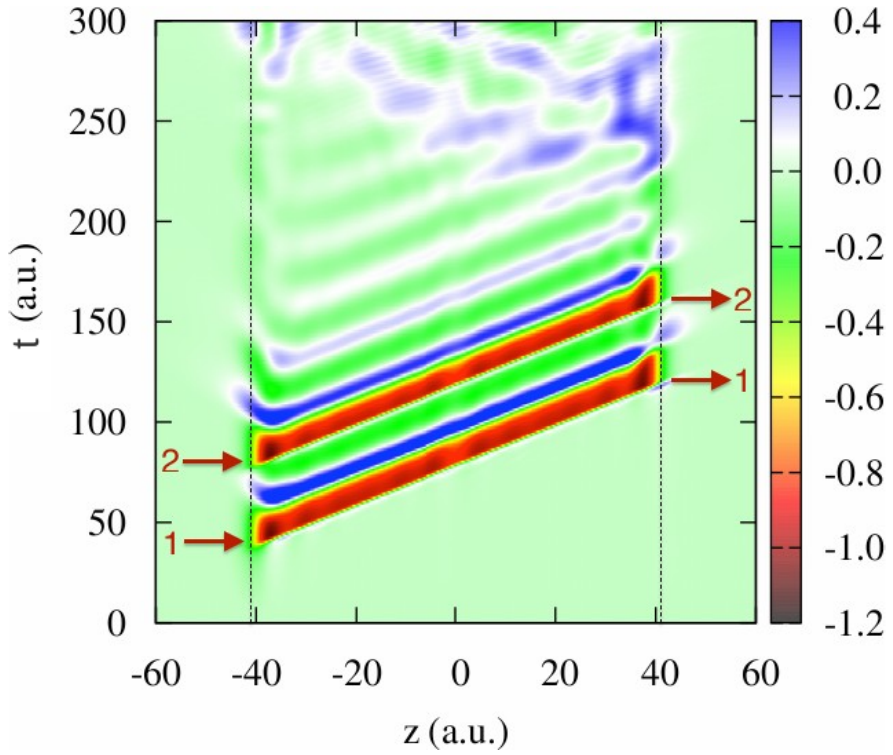

Figure 5.16: Change in electronic density $\Delta n(\rho = 0, z, t)$ of the Na_{1074} cluster along the $z-$axis induced by the moving antiprotons as a function of time. The induced density is normalized to the positive background density. The distance between the antiprotons is 40 a.u. Velocity of the antiprotons is 1 a.u. Radius of the cluster is 40.96 a.u. Arrows indicate when the first and the second antiprotons enter and leave the cluster.

in response to the movement of two antiprotons at a distance $d = 22$ a.u. At this distance, as can be seen in Fig. 5.15, the stopping power for the second antiproton is larger than the stopping power for the first one ($S_2 > S_1$). This can be well understood from Fig. 5.14, in which we see that when the second antiproton enters the cluster it passes through an area with excess of negative charge. Therefore, it experiences a larger stopping force than the first antiproton. In Fig. 5.16 we also show the change in electronic density of the cluster, but in this case the antiprotons move at a distance $d = 40$ a.u. At this distance $S_2 < S_1$. As we can see in Fig. 5.16, in this case the second antiproton enters the cluster when there is less negative charge (negative change of the electronic density). Thus, depending on the delay between the passage of the two particles through the cluster, the second particle finds a minimum or a maximum (or an intermediate state) of the plasmon oscillations and therefore the stopping power for the second particle is

smaller or larger than (or equal to) the one of the first particle.

5.2.4 Real dynamics

In the case of two charges moving through the Na cluster with velocity 1 a.u, the minimum of the stopping power for the second antiproton is at $d = 12$ a.u. (Fig. 5.15). At this value of d the stopping is negative, which means that the second antiproton is accelerated. This result is obtained in the constant velocity approximation where the Coulomb repulsion between the two antiprotons is not included in the dynamics. In this subsection we consider the case of the real dynamics of the antiprotons. The antiprotons start to move with velocity $v_0 = 1$ a.u. at a distance $d_0 = 12$ a.u. from each other. And then we allow for the velocities of both particles to change according to Newton's equations of motion, in which we include the cluster induced force $F_{\rm cl}$ on each antiproton as well as the repulsive Coulomb force between them $F_{\rm int}$. The mass of the antiprotons is $m = 1836$ a.u. We will show in the following that the effect of the acceleration of the second antiproton remains, because the Coulomb forces created by both antiprotons on each other are screened inside the cluster.

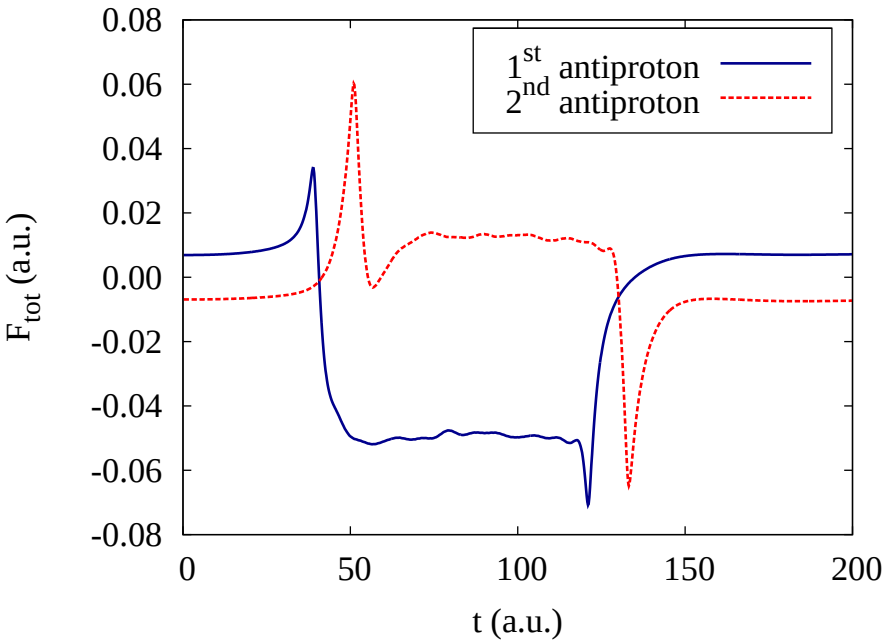

Figure 5.17: Total force, $F_{\rm tot}$, acting on the antiprotons traversing a Na_{1074} cluster as a function of time. Initial velocity of both antiprotons is $v_0 = 1$ a.u. Initial distance between antiprotons is $d_0 = 12$ a.u.

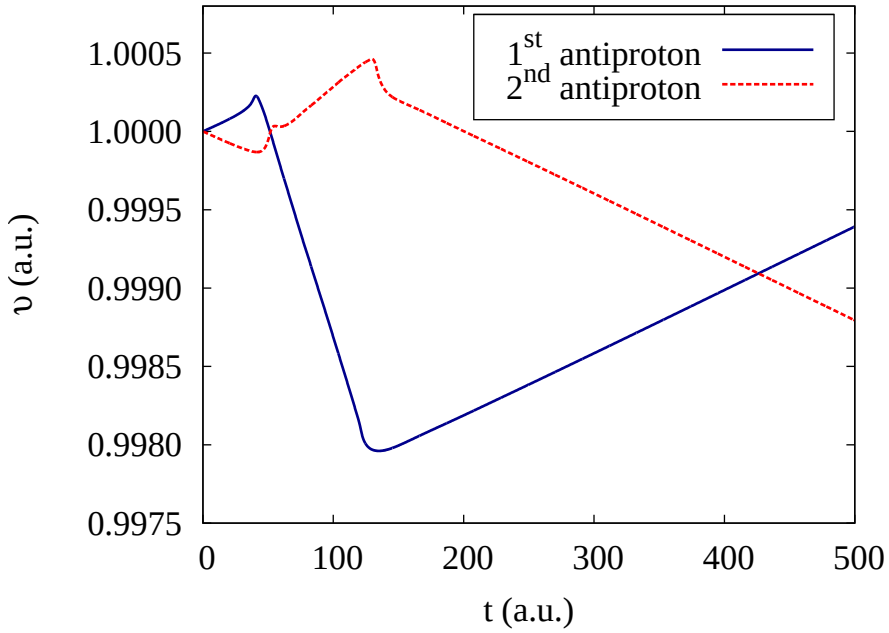

Figure 5.18: Velocity of the antiprotons traversing a Na_{1074} cluster as a function of time. Initial distance between antiprotons is $d_0 = 12$ a.u.

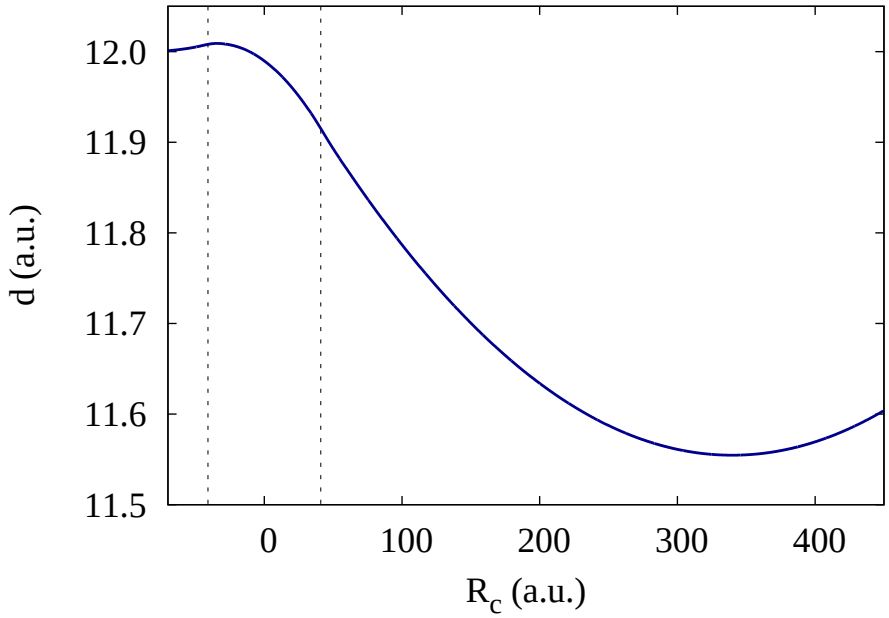

Figure 5.19: Distance between two antiprotons traversing a Na_{1074} cluster as a function of the position of the center of mass. Dashed lines show the borders of the cluster.

In Fig. 5.17 we show the total force acting on each antiproton $F_{\text{tot}} = F_{\text{cl}} + F_{\text{int}}$ as a function of time. Far from the cluster, the only non-zero component of the

force is the Coulomb repulsion between the antiprotons. Inside the cluster, the force on the first antiproton is negative, and the antiproton is slowed down. However, the force acting on the second antiproton is positive, i.e., it is an accelerating force. The plot of the velocity as a function of time confirms that (Fig. 5.18). At the beginning, when the antiprotons move towards the cluster the first antiproton is accelerated, while the one behind is slowed down, as a consequence of the Coulomb repulsion between them. When the particles approach the cluster surface and further move inside the cluster, the situation is reversed. Now the second antiproton is accelerated, while the first one is slowed down. As a result, the distance between the two particles decreases.

The distance d as a function of the position of the center of mass of the two antiprotons is shown in Fig. 5.19. We can see that inside the cluster the distance between the antiprotons starts to decrease and it continues to decrease even outside the cluster. Although outside the cluster the velocity of the first particle grows and the velocity of the second particle drops, the first particle is slower than the second one still for a long time (Fig. 5.18). Thus, we can conclude that the force due to the interference between the dynamic screening of the antiprotons inside the cluster leads to an effective attraction between these two negatively charged particles.

5.2.5 Model calculation in an extended system

We have shown that the screening of two antiprotons inside the cluster leads to attraction between them. In the particular case considered in the previous subsection, the distance between the antiprotons is reduced by almost 0.5 a.u. But the size of the cluster is relatively small (the diameter of the Na_{1074} cluster is 82 a.u.) and therefore the reduction of the distance is also small. One would expect that in a large metallic system (thin film or metal surface) this effect should be much stronger. Since it is complicated to treat such a large systems with our method, we resort to the help of classical dynamics using effective inter-particle potentials obtained from our quantum mechanical results. Using Velocity Verlet algorithm we investigate how the distance between two particles would change if they move in an extended metallic system. We consider that the dynamics of the antiprotons is ruled by the Coulomb interaction between them as well as by the stopping force acting on the antiprotons in a Na_{1074} cluster (Fig. 5.15) due to the

dynamic screening. The latter is a function of the inter-particle distance. Thus, the antiprotons move in an effective potential that includes both interactions mentioned above. Our model, however, will be oversimplified and only valid for relatively short dynamics (still much larger than those that we can treat with TDDFT calculations) since we will neglect the effect of stopping in the center of mass velocity and only focus on the effect of the effective inter-particle potential in the motion of the relative position of the antiprotons.

The effective potential is shown in Fig. 5.20. The figure also includes the pure Coulomb potential as a function of the inter-particle distance. At $d \to 0$ the effective potential is of the Coulomb form. At large d it oscillates around zero. Unlike the Coulomb potential, which is always repulsive, the effective potential in our case is attractive for some values of d.

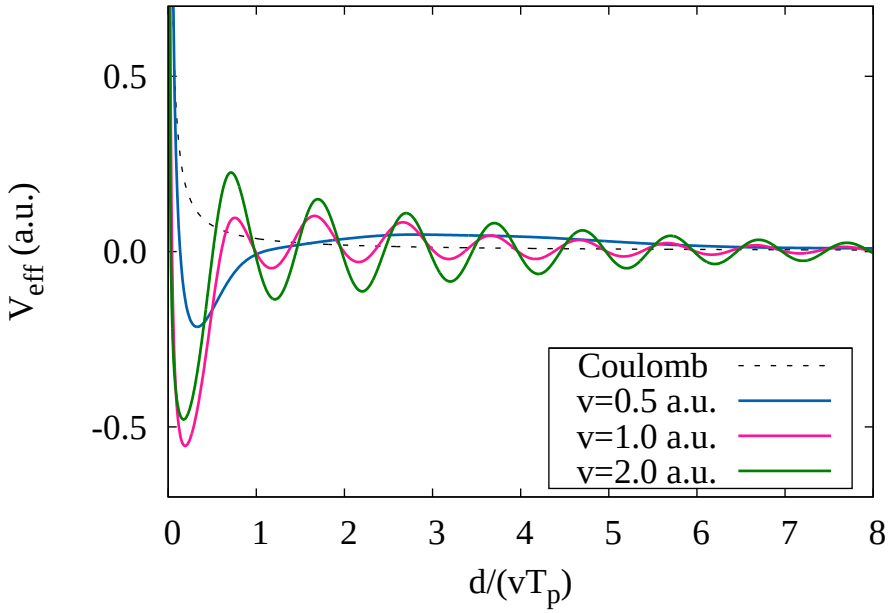

Figure 5.20: Effective potential in which two antiprotons move as a function of the parameter $d/(vT_p)$ for three different velocities of the antiprotons. Here, v refers to the center of mass velocity. The two antiprotons are assumed to move with velocities close to this values.

We performed the Velocity Verlet calculations for two antiprotons with initial velocity 1 a.u. and different initial distances between them, for a time of 5000 a.u. inside the metal. The results are presented in Fig. 5.22 for a set of selected values of the initial distance d between the antiprotons, indicated in Fig. 5.21. In the upper panel of Fig. 5.22 the initial distance is $d_0 = 2$ a.u. At such short distance the effective potential is very repulsive (see Fig. 5.20) and as a consequence the

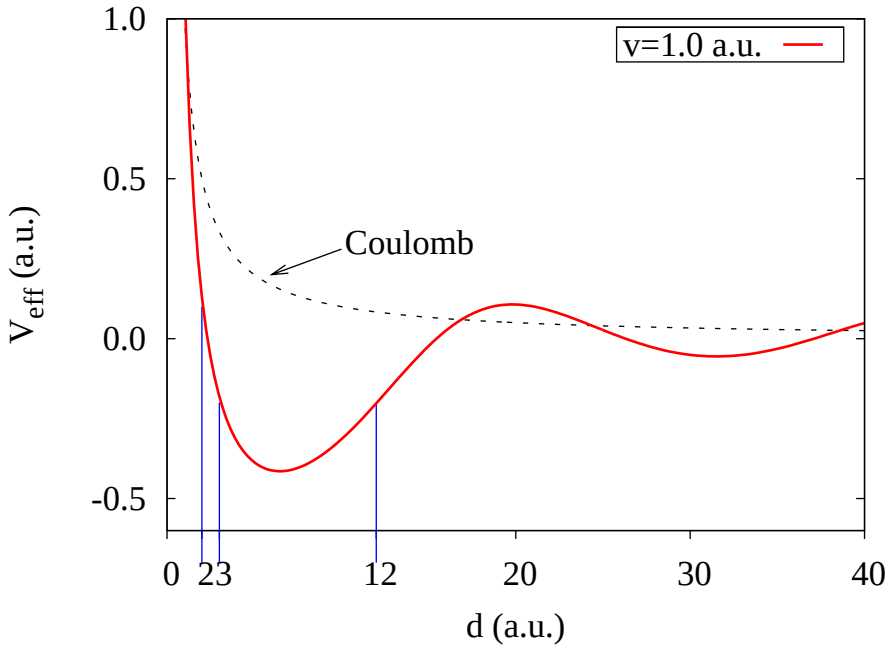

Figure 5.21: Effective potential for antiprotons moving with velocities close to $v = 1$ a.u. and pure Coulomb potential as a function of the distance between the antiprotons. Blue lines indicate the values of d used for the Verlet calculations.

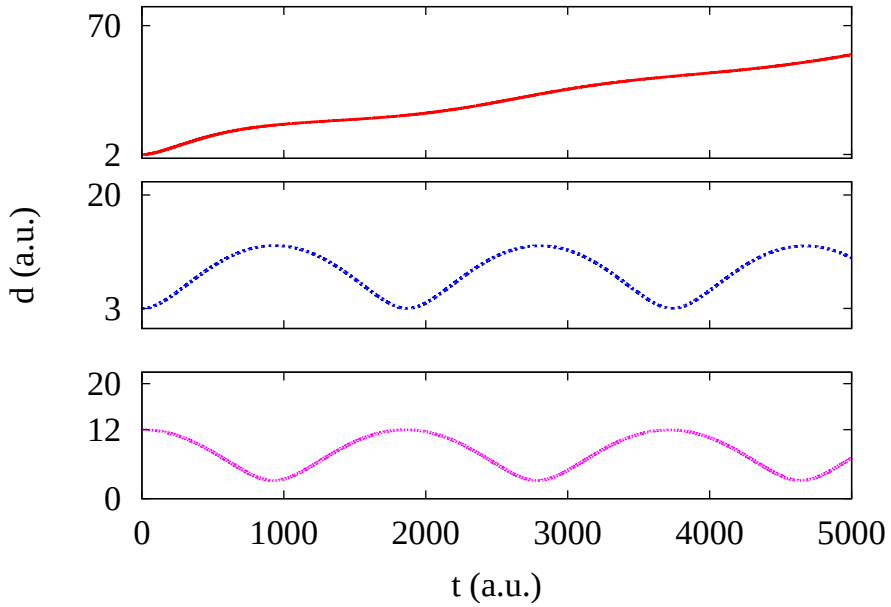

Figure 5.22: Distance between the antiprotons as a function of time for three different values of the initial distance, namely d_0=2, d_0=3, and d_0=12. The initial velocity of the antiprotons is $v_0 = 1$ a.u.

antiprotons move away from each other over the full trajectory. In the middle panel the antiprotons start to move at a distance $d_0 = 3$ a.u. from each other.

Under these initial conditions, at first, the distance between the two particles grows. When the distance reaches the value of approximately 12 a.u., it starts to decrease. Subsequently, under our hypothesis that disregards the effect of losses in the velocity and, thus, in the effective potential for this relatively short propagation time, we observe an oscillating behavior of the relative distance between the antiprotons. In the lower panel, the initial distance is $d_0 = 12$ a.u. Here we also observe the oscillations of the distance in time, but in opposite phase as compared with the previous case. This behavior is consistent with the form of the effective potential. The oscillating character of the effective potential leads to the pairing of the antiprotons. As a consequence and according to our simple model, we conclude that two antiprotons may move through a metallic medium for a long time in a correlated way. Of course, in a more refined model, under development at the moment, the pairing of the particles only takes place for a finite time interval.

5.2.6 Conclusions

In this section we presented the study of the interaction of two antiprotons with metallic clusters. We have studied the vicinage effect in the energy loss of the antiprotons colliding with metal clusters of different sizes. We calculated the stopping power ratio for three different velocities of the antiprotons and for a wide range of distances d between the particles. We have shown that, at low velocities of the antiprotons and at large distances between them, the stopping ratio is roughly equal to 1. At intermediate and high velocities the stopping ratio oscillates around 1 and the origin of the oscillations lies on the plasmon created by the antiprotons in the metal. At short distances between the antiprotons the stopping ratio has a minimum that corresponds to different values of d depending on the velocity.

Furthermore, we have studied in detail the energy loss of each antiproton individually and we have shown that the first antiproton creates a plasmon which affects the motion of the second antiproton. We have shown as well that, at some distances between the antiprotons, the second one can be accelerated. We proved this by performing a dynamic calculation in which we allowed for the velocities of both particles to change according to Newton's equations of motion. This calculation includes the cluster induced force on each antiproton as well as the

Coulomb force between them. As a result we have shown that the Coulomb repulsion between the antiprotons inside the cluster is dynamically screened and that, under certain initial conditions, an effective attraction between the antiprotons can appear. We think that this is a quite remarkable result. Although there has been much speculation to date on the possibility of trapping charged particles in the wake of a moving projectile in a metallic medium, most of those results were based on models where the simultaneous effect of the two particles in the medium was approximated. To the best of our knowledge this is the first non-perturbative calculation at the TDDFT level of theory that predicts that such pairing among equally charged particles can be obtained.

Finally we have studied how two antiprotons would interact if they move in an extended metallic system using a very simplified model fitted to our first-principles results. Using Velocity Verlet algorithm we have shown that the effective attraction between two antiprotons due to the screening processes inside the metal may lead to the pairing of particles. Under certain initial conditions two antiprotons can move in a correlated way inside the metal for a long time. We are currently developing a more sophisticated model that accounts for the overall stopping of the pair of particles and, thus, gives rise to pairing during a finite time. Still, according to our estimations, this time could easily exceed the picosecond time scale depending on the initial conditions.

5.3 Vicinage effect in the energy loss of hydrogen dimers

In the previous chapters we presented the studies of the interaction of charged particles with metals. We used the SJM to represent metallic targets. Here we apply SJM to study the problem of the stopping of hydrogen dimers, and how it differs from that of a single hydrogen atom. Our calculations are then compared to experimental results obtained in different types of targets, including SiO_2, Al_2O_3, TiO_2 and carbon thin films. These targets are very different from the metal particles considered so far. Indeed, the use of the SJM can be questioned for such insulating and semiconducting materials. However, under certain conditions, the jellium model gives reasonable results for stopping provided that the electronic density is properly defined.

The study of the vicinage effect in the energy loss of a hydrogen dimer H_2 moving inside this kind of materials is motivated by the existence of experimental measurements for hydrogen ions H_2^+ colliding with SiO_2 [61]. In the experiments the main observation is that for low projectile energies the stopping power ratio $R < 1$. However, after some threshold velocity, at high energies, the stopping ratio becomes $R > 1$. The transition region from $R < 1$ to $R > 1$ is quite sharp. In their paper, Shubieta *et al.* [61] explain this transition as associated to the plasmon excitation threshold. Using TDDFT we calculate the stopping power ratio for the hydrogen dimer H_2 moving with different velocities through a spherical cluster and give an alternative explanation for the behavior of R trying to disentangle the contribution of each constituent atom in the dimer to the total stopping power. We compare our results with the already published experimental stopping ratio for hydrogen ions H_2^+ colliding with SiO_2 [61] and also with new experimental results for different targets, obtained by the same authors.

We also study the effect of the charge-state of the projectile in the stopping ratio. From previous studies it is known that, depending on the impact parameters (incident energy, target thickness) the hydrogen ion H_2^+ can either lose the bound electron or to be neutralized, while moving inside the solid [103, 104]. We consider three different charge-state fractions for the projectile, namely H_2^{++}, H_2^+, and H_2. We keep the distance between the two protons in the dimer constant for all three charge-state fractions. The target material in our system of interest

is a thin film of about $10 - 25$ Å. Thus, the distance between the dissociated fragments do not increase significantly and therefore the two fragments move in a correlated way. We calculate the stopping power for the hydrogen dimer in all three possible charge-states and analyze the effect of the charge-state in detail. The same is done for the H^+ and H fractions of the hydrogen atom. It should be noted that these are the initial charge-states of the projectiles before entering the cluster. Inside and after leaving the cluster the charge-states can be modified.

In this section we use the same methodology as in the previous one with the only difference that now we can set different orientations of the dimer with respect to the direction of motion ($z-$axis). This became possible thanks to some modifications in the WPP code made by the author of the code, Dr. Andrey Borissov, which allows us to perform fully three-dimensional calculations in the cylindrical coordinates (ρ, ϕ, z). A schematic view of the process is shown in Fig. 5.23. The distance between the two protons in the dimer is fixed and equals $d = 2$ a.u., which corresponds to the distance between them in the experiment. The velocity v of the projectiles is kept constant during propagation. The angle Θ between the axis connecting the two protons and the $z-$axis determines the orientation of the dimer and is fixed in time.

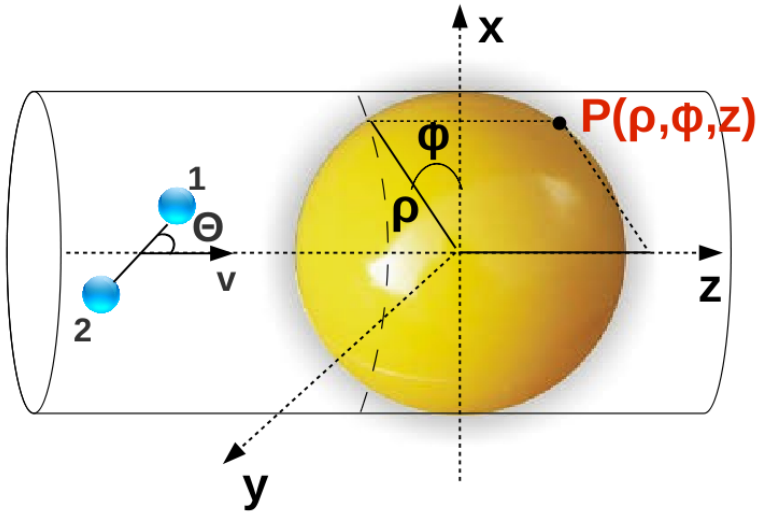

Figure 5.23: Sketch of the process. A hydrogen dimer (with a bond length $d = 2$ a.u., corresponding to the equilibrium bond length of H_2^+) moves along the $z-$axis with a constant velocity v and crosses the spherical cluster through the geometrical center. The axis of the hydrogen dimer makes an angle Θ with the direction of motion.

The ground state of the cluster and of the hydrogen projectiles (with a bound

state) are calculated separately. For the cluster, the ground state is calculated within the SJM using spherical symmetry. The ground states of H_2^+, H_2, and H projectiles are calculated using cylindrical coordinates. This allows us to set an angle Θ for the orientation of the dimer. The total ground state wave functions, in the case in which target and projectile are still decoupled, are the sum

$$\psi_i^{\mathrm{tot}}(\rho,\phi,z) = \psi_i^{\mathrm{cl}}(\rho,\phi,z) + \psi_i^{\mathrm{H_2(H)}}(\rho,\phi,z), \tag{5.6}$$

where the KS states of the cluster are interpolated to cylindrical coordinates.

We consider first a cluster with a density defined by $r_\mathrm{s} = 1.56$ a.u., corresponding to the effective density of SiO_2 (to the observed plasma frequency of SiO_2 [61]). The total number of electrons in the system is equal to the number of electrons in a closed-shell cluster ($N = 338$) plus the number of electrons traveling with a projectile. The radius of the cluster is $R_\mathrm{cl} = 10.87$ a.u. (5.75 Å). Our results for $r_\mathrm{s} = 1.56$ a.u. can also be applied to the experimental stopping ratio of hydrogen dimers interacting with Al_2O_3 ($r_\mathrm{s} = 1.5$ a.u.) and carbon ($r_\mathrm{s} = 1.6$ a.u.) thin films. The difference in r_s for these systems has a negligible effect.

In order to represent the density of TiO_2 we use $r_\mathrm{s} = 1.35$ a.u. In this case the number of electrons in the cluster is $N = 562$. The radius of the cluster is $R_\mathrm{cl} = 11.14$ a.u. (5.9 Å).

The time-dependent electronic density of the system $n(\rho,\phi,z,t)$ is obtained by time-propagation. From the density we calculate the forces acting on each projectile inside the cluster. The stopping power is calculated as the average energy loss per unit path length (5.3). In the case of the dimer, the stopping power is calculated for each proton separately. The total stopping for the dimer is a sum of two contributions: $S_{\mathrm{H_2}} = S_{\mathrm{H^1}} + S_{\mathrm{H^2}}$. The details of the three-dimensional calculations are given in Appendix A.

The stopping power ratio is calculated as

$$R = \frac{S_{\mathrm{H_2}}}{2S_\mathrm{H}}, \tag{5.7}$$

where S_H is the stopping power of a hydrogen atom moving with the same velocity as the H_2 dimer.

5.3.1 Stopping power and stopping ratio for neutral projectiles

Let us consider first the neutral fractions of both molecular and atomic hydrogen. For long interaction times and low impact velocities we usually expect that our charged projectiles will be eventually neutralized. Although the relevance of this assumption for the experimental data on very thin films that we will be addressing can be questioned, particularly at high impact energies, we will start our analysis using neutral projectiles. In this case the stopping ratio is calculated as the ratio between the stopping power for the neutral hydrogen molecule and twice the stopping power for the hydrogen atom.

In order to correctly compare our calculated results with the experiment we consider two main orientations of the hydrogen dimer with respect to the direction of motion. First, a parallel orientation ($\Theta = 0°$), when the internuclear axis is aligned along the trajectory of the center of mass of the dimer. Second, a perpendicular orientation ($\Theta = 90°$), when the internuclear axis is perpendicular to the direction of motion. In Fig. 5.24 we show the results of our calculated electronic stopping power for the H_2 dimer in the two different orientations and twice the stopping power for the hydrogen atom as a function of the projectiles' kinetic energy. The results are shown for two different densities of the target cluster, $r_s = 1.56$ a.u. in panel (a), and $r_s = 1.35$ a.u. in panel (b).

The stopping power for the dimer is not the same as twice the stopping for the hydrogen atom for both orientations of the dimer and for both densities of the cluster. The maxima of the stopping in all three curves are shifted one with respect to another. This gives us a hint of what is the ratio between those values and, therefore, the vicinage effect for the H_2 dimer in both orientations. In particular, the perpendicular stopping power never crosses the stopping for the single atom, which means that the perpendicular component of the stopping ratio never crosses $R = 1$ in the range of energies considered here.

The stopping ratio, Eq. (5.7), as a function of the projectile incident energy is shown in Fig. 5.25 for the dimer in two different orientations and is compared with the experimental data for the two densities considered. In the case of the lower density ($r_s = 1.56$ a.u.) shown in Fig. 5.25(a), the parallel component of the calculated stopping ratio crosses $R = 1$ at an energy of about 90 keV/amu, which is very close to the experimental results. Both components (parallel and per-

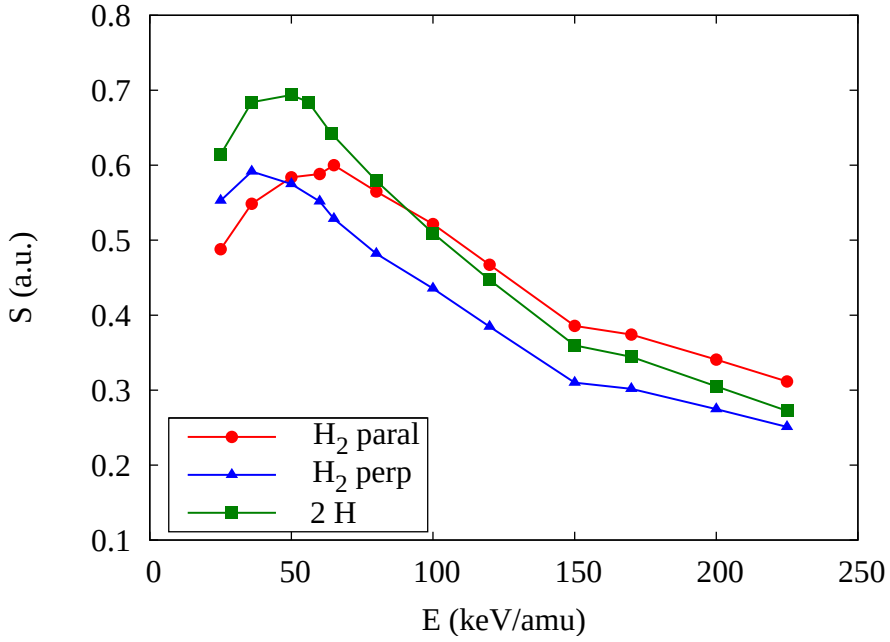

(a)

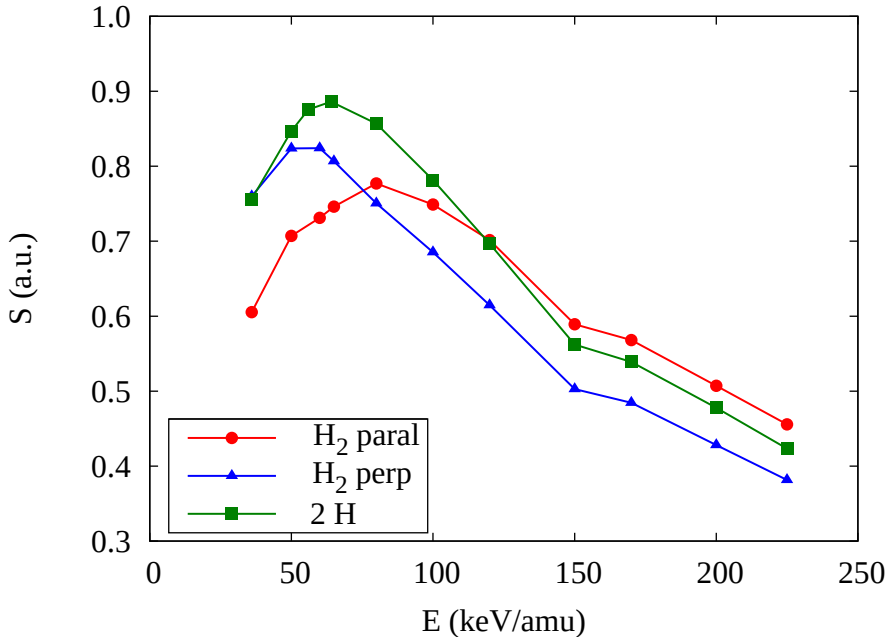

(b)

Figure 5.24: Stopping power, S, as a function of the kinetic energy per proton for the hydrogen dimer (H_2) in two different orientations, parallel and perpendicular. The results for twice the stopping power of the hydrogen atom are plotted as well. Two different densities are shown: a) $r_s = 1.56$ a.u., b) $r_s = 1.35$ a.u.

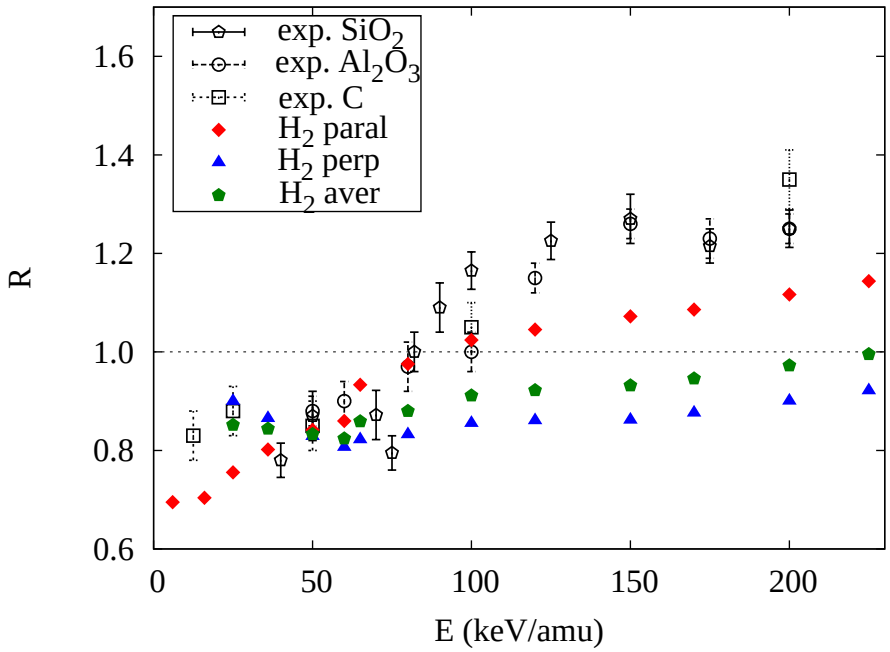

(a)

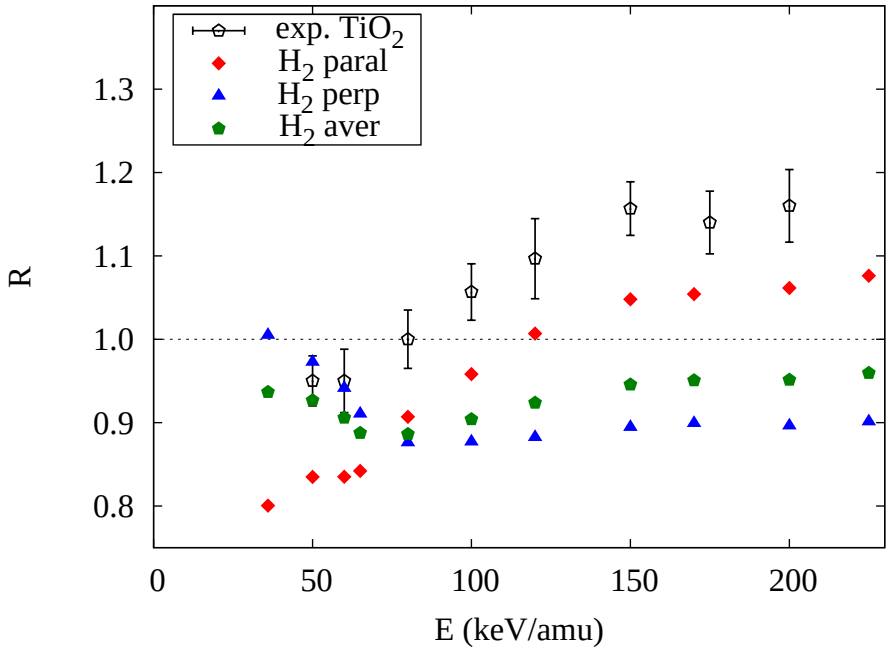

(b)

Figure 5.25: Stopping power ratio, R, as a function of the kinetic energy per proton for the hydrogen dimer H_2 in two different orientations, parallel and perpendicular. The results are shown for a) $r_s = 1.56$ a.u., b) $r_s = 1.35$ a.u. and compared with the experimental stopping ratio.

pendicular) of the stopping ratio agree well with the experiment at low energies. However, at large energies, above 70 keV/amu, the perpendicular component is much lower than the experimental values and never crosses the $R = 1$ value. On the contrary, the parallel component crosses the $R = 1$ value and becomes $R > 1$ at high energies, although still with values lower than the experimental ones. For the stopping power ratio averaged over orientations we include twice the contribution from the perpendicular orientation and once from the parallel, which corresponds to a totally random orientation of the dimer in the experiment:

$$R_{\text{aver}} = (2R_{\text{perp}} + R_{\text{paral}})/3. \tag{5.8}$$

We see that, although the result for the average stopping ratio shows the same tendency of increasing R with the incident velocity observed in the experiment, at high energy R is underestimated in the simulations as compared to the experimental results.

At higher density ($r_s = 1.35$ a.u.), corresponding to TiO_2 (Fig. 5.25 (b)), the behavior is similar. The calculated stopping ratio for the perpendicular orientation of the dimer is again too small at high energies. The parallel orientation gives the stopping ratio with qualitatively the same behavior as the experimental stopping ratio. However, in this case the crossing point between the "parallel" and "perpendicular" ratios and also the crossing of $R = 1$ for the parallel component of the stopping ratio are shifted towards higher energies as compared with the previous density (panel (a)). The average stopping power ratio is in agreement with the experiment at low energies, but is far from the experimental values at intermediate and high energies.

The fact that the parallel stopping ratio is closer to the experiment may indicate that it is the parallel orientation the preferential one for the dimers. This conclusion would be consistent with the torque acting on the dimer inside the cluster. The calculation of the torque is shown in Fig. 5.26 for different angles of the dimer axis with respect to the direction of motion (see the details of the calculations in Appendix A). From this figure we see that the torque is negative for all angles and for all energies considered. The negative torque means that the cluster induced forces acting on the dimer tend to rotate it towards the positive direction of the $z-$axis, i.e., to align it parallel to the direction of motion. However, at high projectile velocities, the crossing of the thin films used in experiments is too fast and there is not enough time for the dimer to be rotated

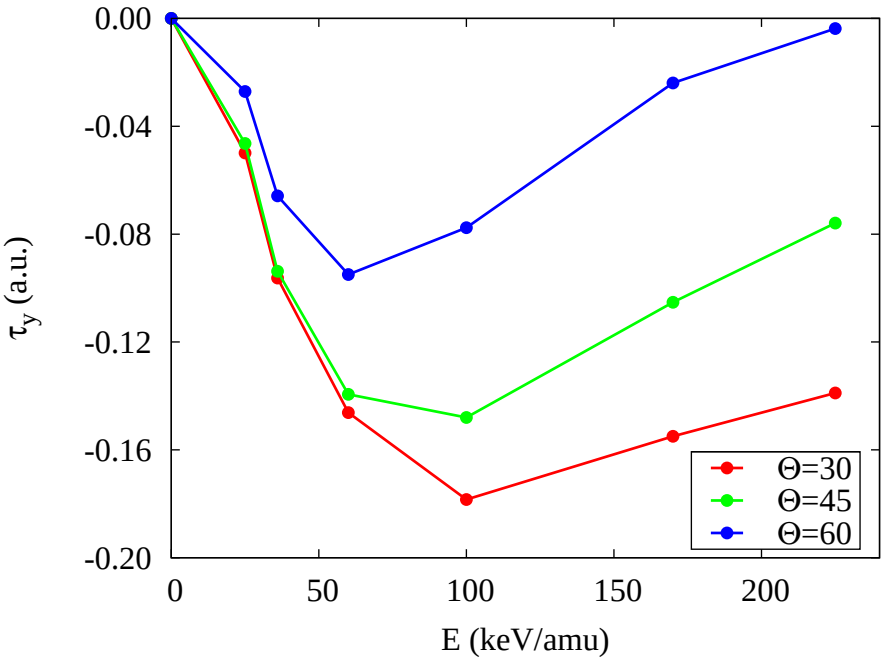

Figure 5.26: Torque, τ_y, acting on the hydrogen dimer H_2 as a function of the incident energy for angles Θ= 30, 45 and 60 degrees.

and the angle Θ cannot change significantly. The concluding remark of this subsection is therefore that we should look for alternative arguments to explain the difference between the calculated stopping power ratio and the measured one (Fig. 5.25) at high energies.

5.3.2 Charge-state effect in the stopping power

The discrepancy between experimental measurements and theoretical results in Fig. 5.25 can be rectified if we consider the role of other charge-states of the projectiles at high energies. In order to show this we calculate the stopping power for all possible initial charge-states of the projectiles, such as H_2^{++}, H_2^{+}, H_2 and also H^+ and H. The results of such calculations are shown in Fig. 5.27.

From Fig. 5.27(a) we see that at high energies the stopping power differs significantly depending on the charge-state, being much larger for a proton than for a neutral hydrogen atom. At low energies, however, both curves reach the same limit. Below 40 keV the stopping power is the same for both projectiles. The same is observed in the case of the dimer in parallel orientation (Fig. 5.27(b)). For the perpendicular dimer the different charge-state values of the stopping power

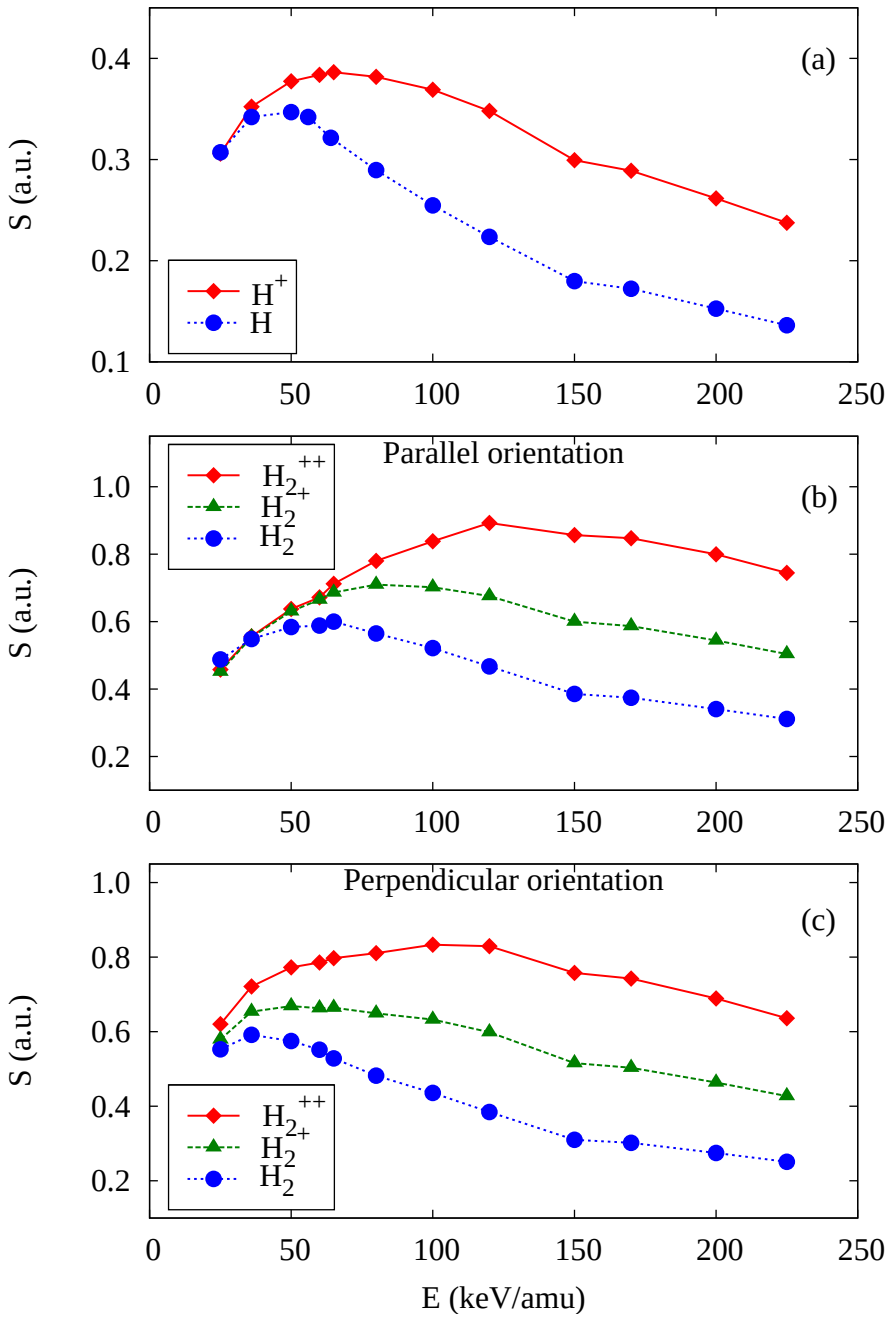

Figure 5.27: Stopping power, S, as a function of the projectile energy for hydrogen in different initial charge-states: (a) hydrogen atom; (b) dimer in parallel orientation; (c) dimer in perpendicular orientation. Results are shown for fully ionized, partially ionized, and neutral species.

are not the same, but close to each others at low energies. Similar stopping power at low energies means that although initially the projectiles are in different charge-states, during the collision process the total electron density around the moving

protons is similar.

The charge-state of hydrogen projectiles interacting with a solid is known to be dependent on the energy. Both for atomic and molecular hydrogen at energies above 40 keV the fully ionized fractions dominate, reaching 100% at about 200 keV, as can be seen in Fig. 5.28 for the case of Mg targets. Below 40 keV the neutral fractions dominate [103, 105]. Although the exact distribution of the charge fractions as a function of the projectile energy is material dependent, the general behavior is, in general, similar. This means that at high energies we should take the H^+ fraction for the atomic projectile and the H_2^{++} fraction for the molecular projectiles to calculate the stopping ratio. At low energies, however, the neutral fractions (H atom and H_2 molecule) will be dominant. Taking into account that at low energies the stopping powers for both neutral and fully ionized projectiles are very similar (Fig. 5.27), we can use H^+ and H_2^{++} projectiles to estimate the stopping power ratio in the whole range of energies considered.

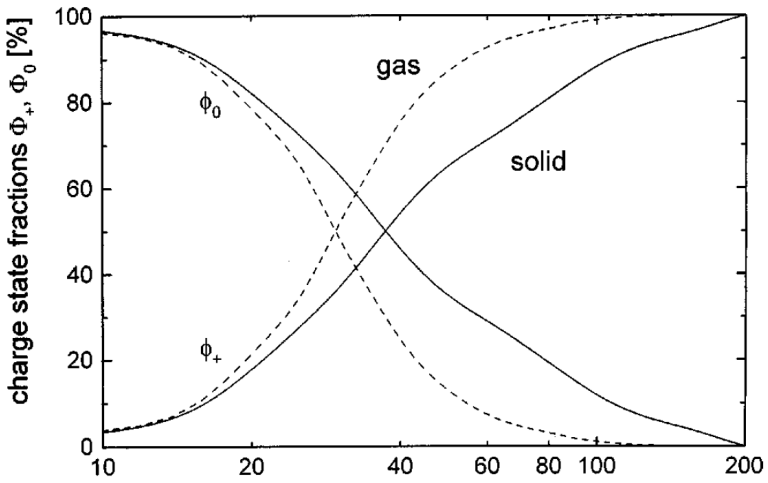

Figure 5.28: Equilibrium charge-state fractions for protons (Φ_+) and for neutral hydrogen (Φ_0) for the solid and the gas phase of Mg [105].

5.3.3 Stopping power and stopping ratio for fully ionized projectiles

Figure 5.29 shows the stopping power for the hydrogen dimer H_2^{++} in parallel and perpendicular orientations as well as twice the stopping power for a single proton. We see that, in contrast to the results for initially neutral dimers

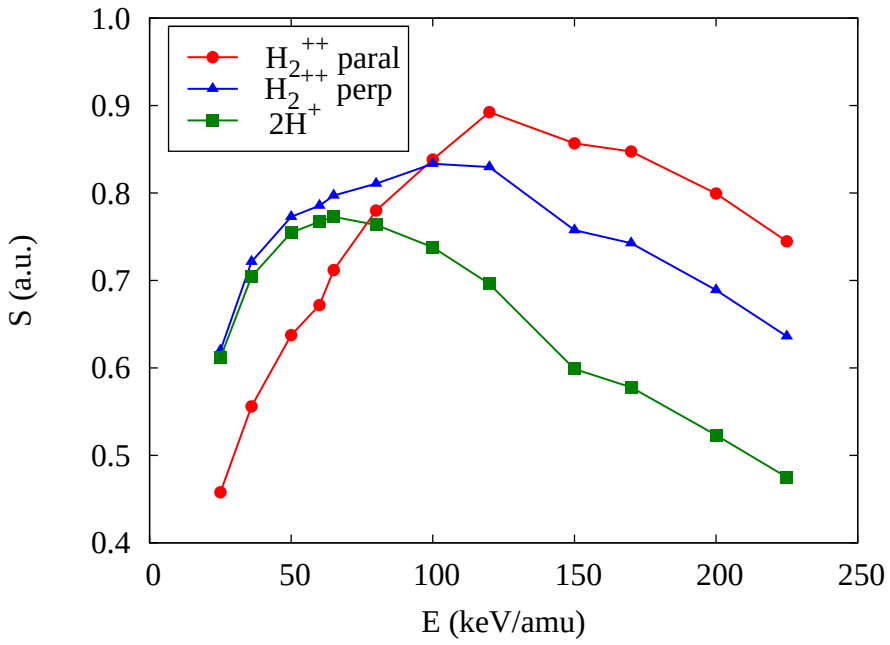

Figure 5.29: Stopping power, S, as a function of the projectile energy for H_2^{++} in parallel and perpendicular orientations, as compared with twice the stopping power for a single proton. Density of the cluster is defined by $r_s = 1.56$ a.u.

(Fig. 5.24), in the case of fully ionized dimers both the stopping power for parallel and for perpendicular dimers are larger than the stopping for a single proton at high energies. This means that in the case of fully ionized dimers not only the stopping ratio for the parallel dimer, but also the one for the perpendicular dimer are larger than 1 at high energies. This can be seen in Fig. 5.30.

In Fig. 5.30 we show the results of our calculated stopping power ratio as a function of the incident kinetic energy of the projectiles for a H_2^{++} dimer in two different orientations and compare it with the experimental data for SiO_2, Al_2O_3 and C. From Fig. 5.30 one can see that the calculated average stopping ratio (Eq. (5.8)) perfectly agrees with the experiments. The transition from $R < 1$ to $R > 1$ is well reproduced. At high and intermediate energies the calculated and the experimental results fit within the error bars. The agreement between the experimental data and the calculated results is remarkable taking into account the simplicity of our approach based on the jellium model. At low energies there is a small deviation of the calculated stopping ratio from the experimental, being the consequence of the differences in the stopping power for different charge-states of the perpendicular dimer at $E < 40$ keV (Fig. 5.27(c)). Also, at low velocities we eventually expect to find discrepancies between our

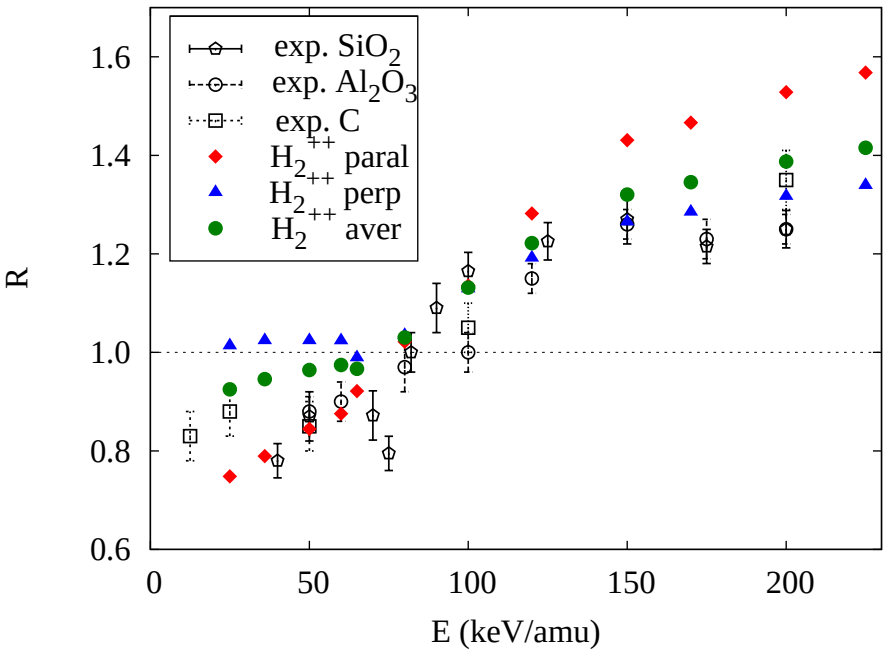

Figure 5.30: Stopping power ratio, R, for H_2^{++} as a function of the projectile energy. Calculated stopping ratio for the dimer moving in parallel, perpendicular and averaged orientations through the jellium cluster with $r_s = 1.56$ a.u. is compared to the experimental stopping ratio for randomly oriented hydrogen ions in SiO_2, Al_2O_3 and carbon C thin films.

approach based on a description of the target as a metal (although with an effective electron density of experimental targets) and the experimental results obtained in insulating and semiconducting materials.

The stopping ratio at high energies is much larger than unity. In order to understand this behavior, we analyzed in detail the individual contributions of protons in dimers H_2^{++} to the total stopping power in the cluster with $r_s = 1.56$ a.u. In Fig. 5.31 we show the stopping power for each proton in a parallel dimer separately as well as for one of the protons in a perpendicular dimer and for a single proton. This figure shows that at high energies the stopping power for the single proton is lower than the stopping power for any proton in a dimer. This means that, for the particular inter-particle distance considered here, the interference in the dynamic response of the target electrons to the motion of two particles in close proximity to each other tend to increase the energy loss (and therefore the stopping power of the target) for each of these particles as compared with the energy loss of an individual particle. Another interesting observation here is that the stopping power for the second proton of the parallel dimer is much

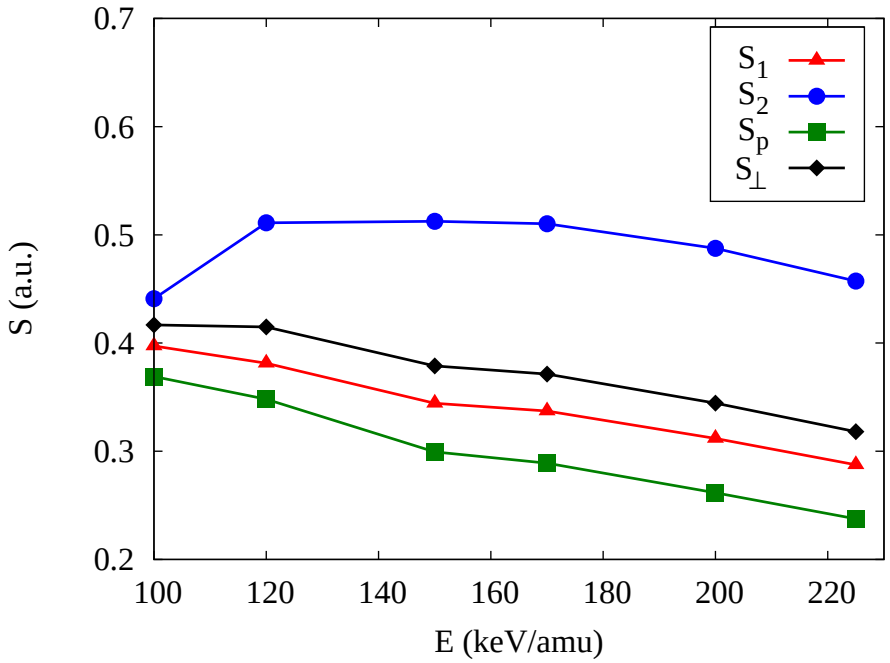

Figure 5.31: Stopping power, S, as a function of the projectile energy for the first (S_1) and the second (S_2) protons in the parallel dimer, for a single proton (S_p) and for one of the protons of the perpendicular dimer ($S_\perp$).

larger than the stopping power for the first proton. This can be easily understood if we take a look at how these particles are screened inside the cluster.

5.3.4 Nonlinear screening of protons in a cluster

The energy loss or the stopping power is a consequence of the dynamic screening of the moving projectiles by the electrons of the cluster. In Fig. 5.32 we show the snapshots of the induced electronic density inside the cluster when two protons in different orientations or a single proton are passing through the center of the cluster with velocity 2.5 a.u. (corresponding to 150 keV/amu of kinetic energy). The protons move along the $z-$axis from left to right. The induced density is the difference between the electronic density at a given time t and the electronic density at time $t = 0$:

$$\Delta n(\mathbf{r}, t) = n(\mathbf{r}, t) - n(\mathbf{r}, t = 0). \tag{5.9}$$

This quantity is plotted in the $(\rho, z, \phi = 0)$ plane, which contains the two protons

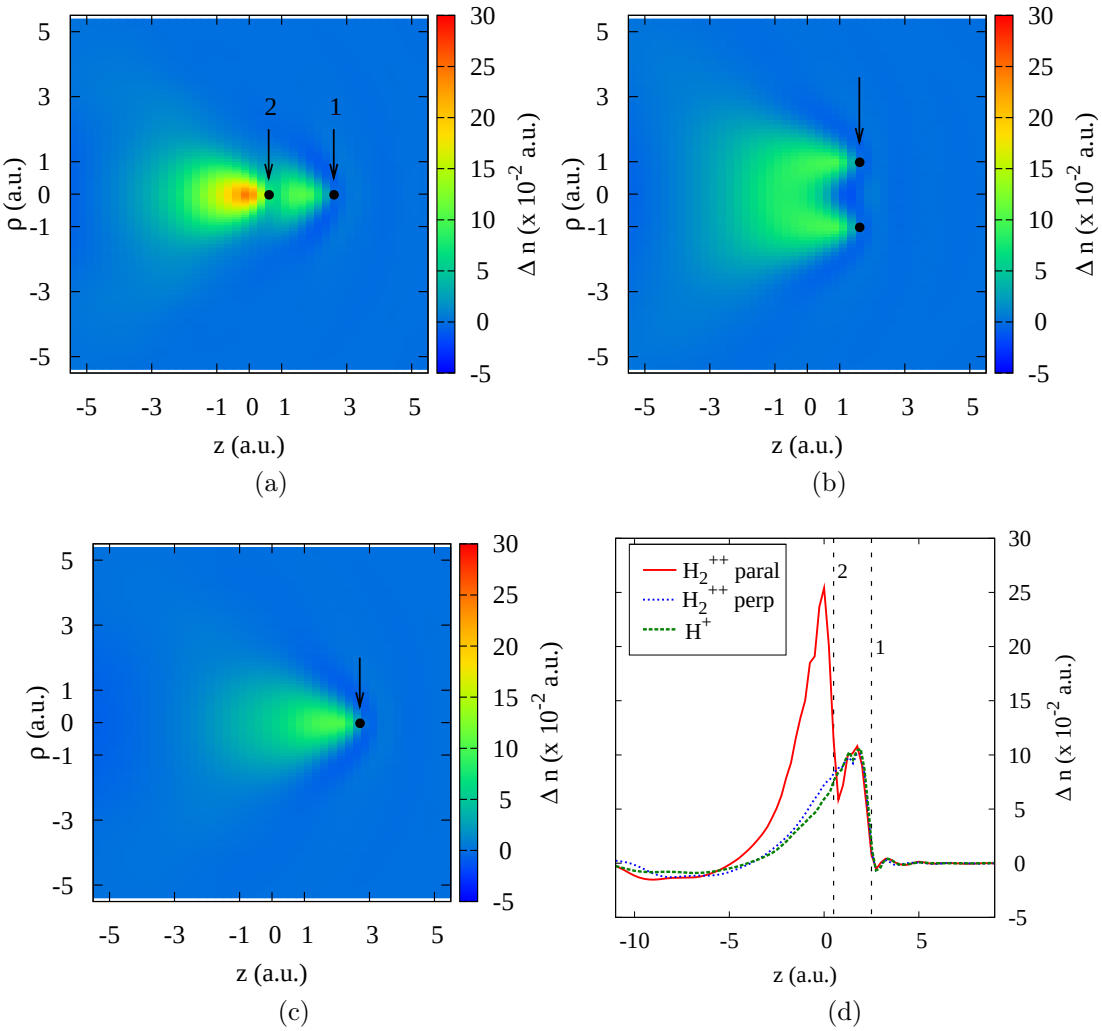

Figure 5.32: Snapshot of the induced electronic density inside the cluster (r_s = 1.56 a.u.) due to the movement of a) two protons with the axis aligned along the trajectory; b) two protons with the axis perpendicular to the trajectory; c) one proton. Panel d) shows the induced density along the trajectory ($z-$axis) at ρ = 0 for a) and c) and at $\rho = 1$ for b). Velocity in all the cases is $v = 2.5$ a.u. Black dots indicate the positions of the protons.

in the dimer. The center of the cluster is located at ($\rho = 0, z = 0$). In the panel (a) of Fig. 5.32 the change in electronic density varies in the range $[-5 : 30] \times 10^{-2}$ a.u. In the two other panels, (b) and (c), the scale for $\Delta n(\mathbf{r}, t)$ is limited to the same values to facilitate the visual comparison. In the panels (a), (b), and (c) of Fig. 5.32 we see the cone-shaped screening cloud behind each projectile, which means that the projectiles create a wake within the target. This form of the screening cloud is characteristic for high projectile energies. The velocity of the protons is much higher than the Fermi velocity of the electrons ($\upsilon_{\mathrm{F}} = 1.23$ a.u.) in the cluster. Thus, the response of the cluster electrons to the movement of the projectiles is delayed. Moreover, the distance between two protons is small and therefore the parallel dimer is screened as a single object by the cluster electrons. This leads to a much larger accumulation of charge behind the second proton than behind the first one (Fig. 5.32(a)) and gives rise to a larger stopping power for the second proton in the parallel dimer.

For the perpendicular dimer the picture is different (Fig. 5.32(b)). Both protons are screened equally and the screening cloud behind each one looks similar to the screening of the single proton (Fig. 5.32(c)).

In order to quantify the differences shown in panels (a), (b), and (c) we show in Fig. 5.32(d) the change in the electronic density of the cluster along the trajectory ($z-$axis) for $\rho = 0$ in the case of the parallel orientation of the dimer and the single proton and for $\rho = 1$ in the case of the perpendicularly oriented dimer. Figure 5.32(d) shows that there is an interference in the screening of both protons in the perpendicular dimer, not noticeable in Fig. 5.32(b). This explains the smaller change in electronic density around the single proton (and therefore the smaller value of the stopping power) as compared with the proton in the perpendicular dimer.

A nonlinear treatment of electron dynamics in the cluster perturbed by the moving protons is essential for the correct estimation of a vicinage effect. In order to prove this we plot in Fig. 5.33 the change in electronic density induced by the moving parallel dimer H_2^{++} in two different approximations. In panel (a) of Fig. 5.33 we plot a snapshot of the density change induced by a pair of protons moving through the cluster. In turn, in panel (b) of Fig. 5.33 we plot the sum of two snapshots of the density change induced by a single proton at two different positions (at a distance 2 a.u.). Therefore, the latter is the linear combination of the change in density. In panel (c) we compare both results, plotting the induced

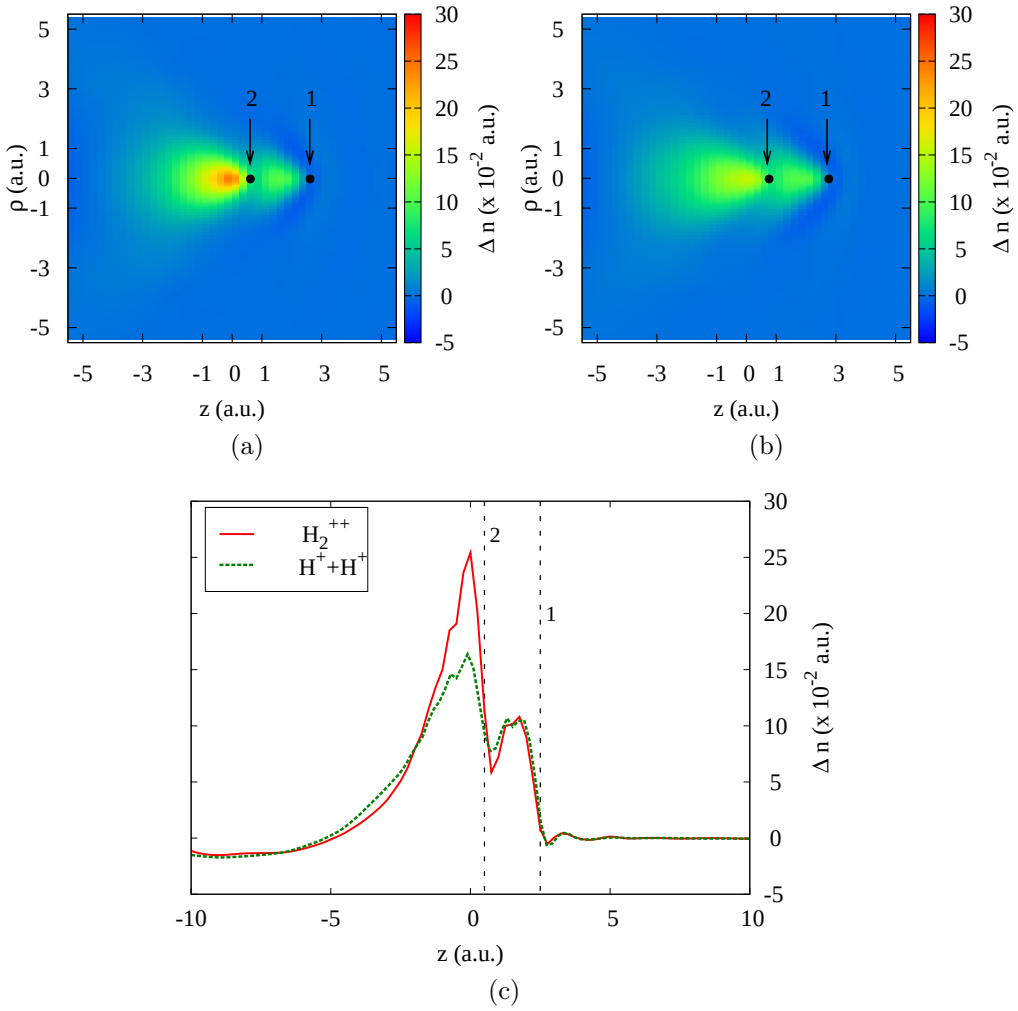

Figure 5.33: (a) Snapshot of the induced electronic density inside the cluster by a hydrogen dimer. (b) The sum of the induced densities by a single proton at two different positions. (c) A cut of the induced densities from (a) and (b) at $\rho = 0$.

density along the $z-$axis for $\rho = 0$. From this figure we see that the induced density around the second proton (as well as the minimum between the two maxima in the induced density) is underestimated in linear theory, as compared with the nonlinear calculation.

5.3.5 Conclusions

In this section we have shown the results for the stopping power ratio for a hydrogen dimer in different orientations traversing a jellium cluster in a large range

of projectile energies. The influence of the charge-state of the hydrogen projectiles on the stopping power is investigated. We compared our calculated results with experimental measurements. A good agreement with the experimental stopping power ratio at all energies is only achieved in the case of the initially fully ionized projectiles. At low energies the calculated results for neutral projectiles also give a reasonable agreement with the experiment. The similarity of the theoretical results for the stopping power of projectiles with different initial charge-states at low energies indicates that the total amount of the electron density around the moving protons inside the target are similar.

We analyzed in detail the individual contributions of each proton in the dimers to the total stopping power and have shown that the stopping power for the second proton in the parallel dimer is much larger than for the first one. We explained this behavior in terms of the dynamic screening of the protons inside the cluster. We have stressed as well the importance of the nonlinear treatment of the dynamic screening processes.

5.4 Summary

In this chapter we have shown that the energy loss of projectiles travelling through metallic media can vary depending on the initial state of the projectile-target system. First, in Section 5.1, we have shown that the energy loss of an antiproton crossing an Al cluster previously excited is lower than the energy loss of an antiproton crossing a ground state cluster. Second, in Section 5.2, we have made a systematic study of the energy loss of two antiprotons moving at different distances from each other through different metallic clusters. We have shown that the total energy loss of the pair of particles strongly depends on the distance between them. At high antiproton velocities the total energy loss oscillates as a function of the distance between the particles. The oscillations arise because of the interaction between the second antiproton and the wake created by the antiproton which first enters the cluster. Due to the oscillations, the second antiproton can even have a negative energy loss, i.e., it can gain energy and thus can be accelerated. As a result the distance between the two particles can decrease. This can lead to an effective bonding of the two antiprotons which then move in a correlated way through the cluster.

In Section 5.3, we performed a fully three-dimensional study of the vicinage effect in the energy loss of a hydrogen dimer moving with different orientations through the spherical cluster. We have shown that the calculated stopping ratio for the dimer of protons is in good agreement with the experiment if the charge-states of the projectiles are correctly accounted for. The detailed analysis of the induced density inside the cluster and also of the individual stopping powers for each proton in the dimer helped us to understand the behavior of the stopping ratio.

Chapter 6

TDDFT calculation of the electronic friction of antiprotons colliding with metal clusters

In this chapter we study the dissipative force experienced by a negatively charged particle (an antiproton) penetrating a metal cluster. In our case, the antiproton is chosen as a projectile because it has large mass as compared to the electrons of the cluster. Therefore we can assume that the velocity of the antiproton does not change while crossing the cluster. This allows us to study the dependence of the dissipative force on the projectile velocity.

The metal cluster is represented in the framework of the SJM. We study two different metals - Na ($r_s = 4$) and Al ($r_s = 2.07$). The antiproton (ap) moves along the z-axis with a constant velocity v and crosses the cluster through its center (as shown in Fig. 6.1). The initial position of the antiproton is such that there is no interaction between the antiproton and the cluster.

The total force felt by the moving antiproton is made of two contributions - the adiabatic component $F_{\mathrm{adiab}}[z_{\mathrm{ap}}(t)]$ and the nonadiabatic (dissipative) component $F_{\mathrm{dissip}}[z_{\mathrm{ap}}(t), t]$. Therefore, the dissipative force on the antiproton is:

$$F_{\mathrm{dissip}}[z_{\mathrm{ap}}(t), t] = F_{\mathrm{tot}}[z_{\mathrm{ap}}(t), t] - F_{\mathrm{adiab}}[z_{\mathrm{ap}}(t)] \tag{6.1}$$

We can find the total force acting on the antiproton crossing a spherical cluster

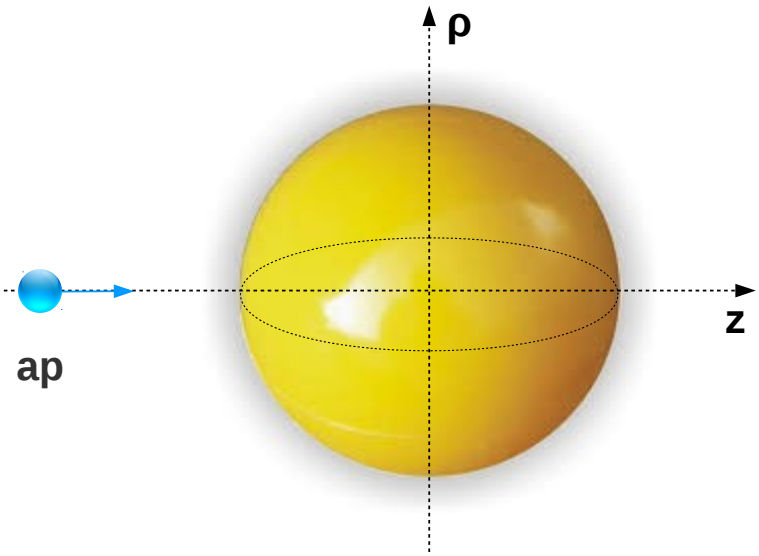

Figure 6.1: Sketch of the process. An antiproton crosses the spherical cluster through the geometrical center.

from the time-dependent electronic density:

$$F_{\rm tot}[z_{\rm ap}(t),t] = 2\pi \int \rho d\rho dz \frac{n(\rho,z,t) - n_0^+(\rho,z)}{[(z_{\rm ap}(t)-z)^2+\rho^2]^{3/2}}[z_{\rm ap}(t)-z] \tag{6.2}$$

In order to find the dissipative force we first need to calculate the adiabatic component of the force. The adiabatic force only depends on the position of the particle and, as far as the process for which the particle appears at that position is sufficiently slow, this force and the energy of the system should not depend on the concrete history of the system. This is the so-called adiabatic switching which tells us that, under certain conditions, the slow switching on of an interaction does not alter the quantum state of the system. In our case, we start with the metal cluster in its ground state and slowly switch on the particle at a given position on the z-axis, either inside or outside the cluster, while following the time evolution of the electron wave functions. During this process the system will remain very close (in principle, the slowest the process the closest) to the ground state of the each instantaneous configuration. The charge Q should be switched on from 0 to -1 very slowly and for this purpose we use a *sin* function:

$$Q(t) = -\sin\left(\frac{\pi}{2T}t\right), \tag{6.3}$$

with the constant $T = 225$ a.u. After time $t = T$ the charge is equal to -1, thus the antiproton has been created at a given position while the system remains in its ground state. At this time we calculate the force acting on the charge. By calculating the force at different positions of the antiproton we can obtain the adiabatic force for the whole trajectory. The full curve is obtained by numerical interpolation of the adiabatic values. The same method is used to calculate the adiabatic component of the total energy of the system.

For velocities below the Fermi velocity of the electrons (for Na it is $v_{\mathrm{F}} = 0.48$ a.u. and for Al it is $v_{\mathrm{F}} = 0.93$ a.u.) the dissipative force can be described, at least in bulk metals, as a friction force and we expect the following linear relation:

$$F_{\mathrm{dissip}}[z_{\mathrm{ap}}(t)] = -\eta[z_{\mathrm{ap}}(t)]v_{\mathrm{ap}}, \tag{6.4}$$

from which we can find the friction coefficient:

$$\eta[z_{\mathrm{ap}}(t)] = -\frac{F_{\mathrm{dissip}}[z_{\mathrm{ap}}(t)]}{v_{\mathrm{ap}}}. \tag{6.5}$$

The validity of this approximation, in which a position dependent friction coefficient is defined for an inhomogeneous system (metallic cluster), will be tested in the present work by means of the explicit time-dependent simulation of the electron dynamics of the cluster electrons.

6.1 Total energy and forces

We consider as targets three sodium clusters ($r_{\mathrm{s}} = 4$), composed by 20 (Na_{20}, radius of the cluster is $R_{\mathrm{cl}} = 10.86$ a.u.), 106 (Na_{106}, $R_{\mathrm{cl}} = 18.93$ a.u.), and 1074 (Na_{1074}, $R_{\mathrm{cl}} = 40.96$ a.u.) electrons. This allows us to study the effect of the size of the cluster on the friction coefficient. We consider as well one Al cluster ($r_{\mathrm{s}} = 2.07$) composed by 106 electrons (Al_{106}, $R_{\mathrm{cl}} = 9.8$ a.u.) in order to account for the effect of a different density.

In Fig. 6.2 we show the total energy of the Na_{106} cluster as a function of the antiproton position when the antiproton crosses the cluster moving with different velocities. The orange curve is the adiabatic energy shown as a reference. Point $z = 0$ corresponds to the center of the cluster. From Fig. 6.2 we see that, when the antiproton is still far from the cluster, the energy keeps a constant value.

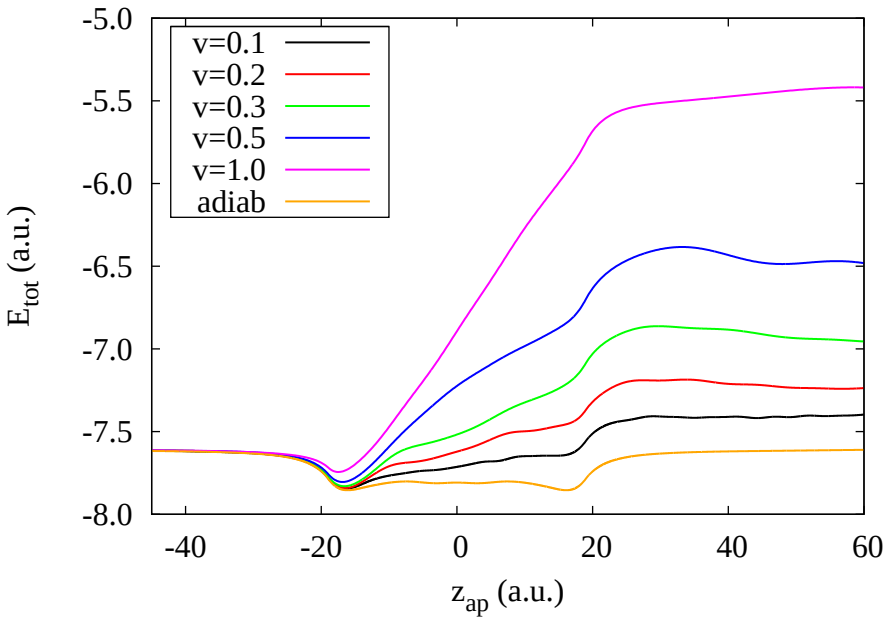

Figure 6.2: Total energy of the system for different antiproton velocities (Na_{106} cluster). Orange line shows the adiabatic component.

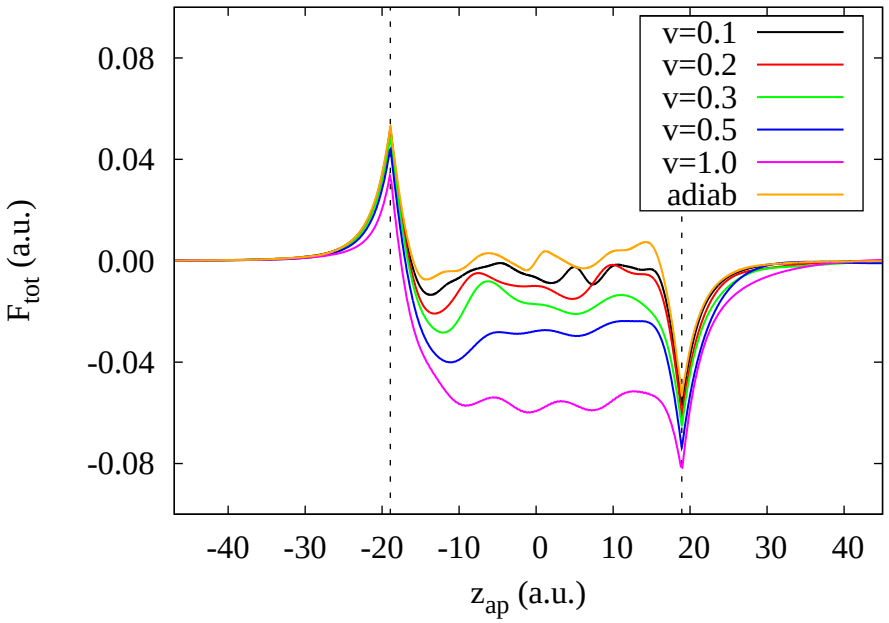

Figure 6.3: Total force felt by the antiproton crossing the Na_{106} cluster with different velocities as a function of the antiproton position. Orange line shows the adiabatic component. Vertical dashed lines show the border of the positive background of the cluster.

This value is the total energy of the ground state cluster. When the antiproton approaches and crosses the cluster surface there is a rapid decrease of the energy.

This reduction of the energy depends on the velocity of the antiproton. At high velocities there is not enough time to fully develop the attractive polarization charge around the antiproton at the time of the crossing of the cluster surface. At small velocities, however, we get a large decrease of the energy upon crossing the surface because a slow charge is more effective in polarizing the medium. After the crossing of the surface, the energy increases and it reaches finally a constant value. The difference between the adiabatic energy and the energy for a given velocity when the antiproton has left the cluster corresponds to the energy loss of the antiproton moving with this particular velocity.

Figure 6.3 shows the total force acting on the moving antiproton as a function of its position. The peaks in the force when the antiproton crosses the cluster surfaces are due to the polarization charge created in the cluster by the moving charge. The singular character of the force at the surface is due to the fact that the positive background charge is given by a step function. Inside the cluster the force is almost flat and roughly corresponds to the stopping power for each velocity of the projectile. The same behavior of the total energy and force is observed for all other clusters studied.

Subtracting the adiabatic force (Fig. 6.3, orange curve) from the total force we obtain the dissipative force experienced by the antiproton. The dissipative force is shown in Fig. 6.4 as a function of the antiproton position for several projectile velocities. From this figure we see that, when the antiproton approaches the cluster surface, the dissipative force increases. Inside the cluster it is oscillating around a mean value which, as in the case of the total force, corresponds to the stopping power. The reason for this is that the mean value of the adiabatic force is roughly zero. An interesting observation is that the dissipative force is not the same on the way "in" and "out" of the cluster. The value of the force is larger when the antiproton crosses the border moving out from the cluster.

The asymmetry is better seen from Fig. 6.5, where the dissipative force is shown outside the cluster in the way in and in the way out from the cluster. In order to understand the asymmetry in the dissipative force, let us look at the electronic density distribution in the Na_{106} cluster for different positions of the antiproton outside and inside the cluster.

In Fig. 6.6 we show the electronic density of the spherical cluster Na_{106} as a function of the (z, ρ) coordinates at different time steps. The antiproton crosses the cluster moving with velocity $v = 0.3$ a.u. Pictures correspond to six different

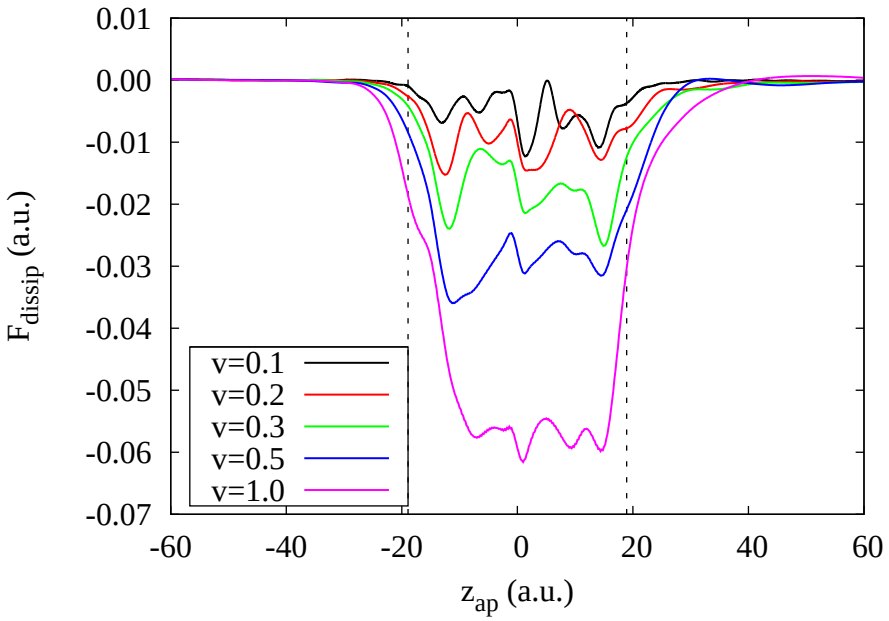

Figure 6.4: Dissipative force felt by the antiproton moving with different velocities through the Na_{106} cluster as a function of the antiproton position. Vertical dashed lines show the border of the positive background of the cluster.

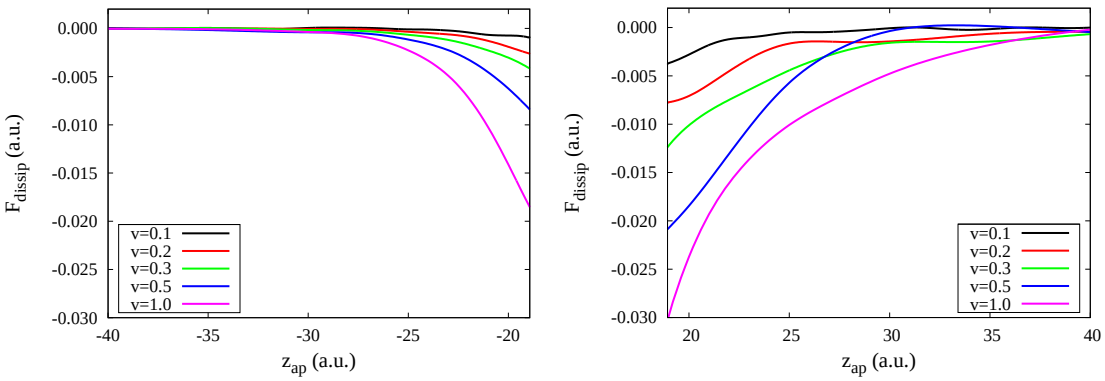

Figure 6.5: Left – the dissipative force felt by the antiproton approaching the Na_{106} cluster with different velocities is shown up to the cluster surface; right – the dissipative force felt by the antiproton leaving the cluster is shown from the cluster surface.

antiproton positions: a) $z = -30$ a.u, b) $z = -20$ a.u, c) $z = -10$ a.u, d) $z = 10$ a.u, e) $z = 20$ a.u, f) $z = 30$ a.u. When the antiproton is still far from the cluster (Fig. 6.6a) the cluster is unperturbed. Approaching the surface of the cluster the antiproton polarizes it and we see a depletion of electronic charge at the cluster surface (Fig. 6.6b). Therefore, when entering the cluster, the antiproton crosses an area of low electronic density. While moving inside the cluster, the antiproton

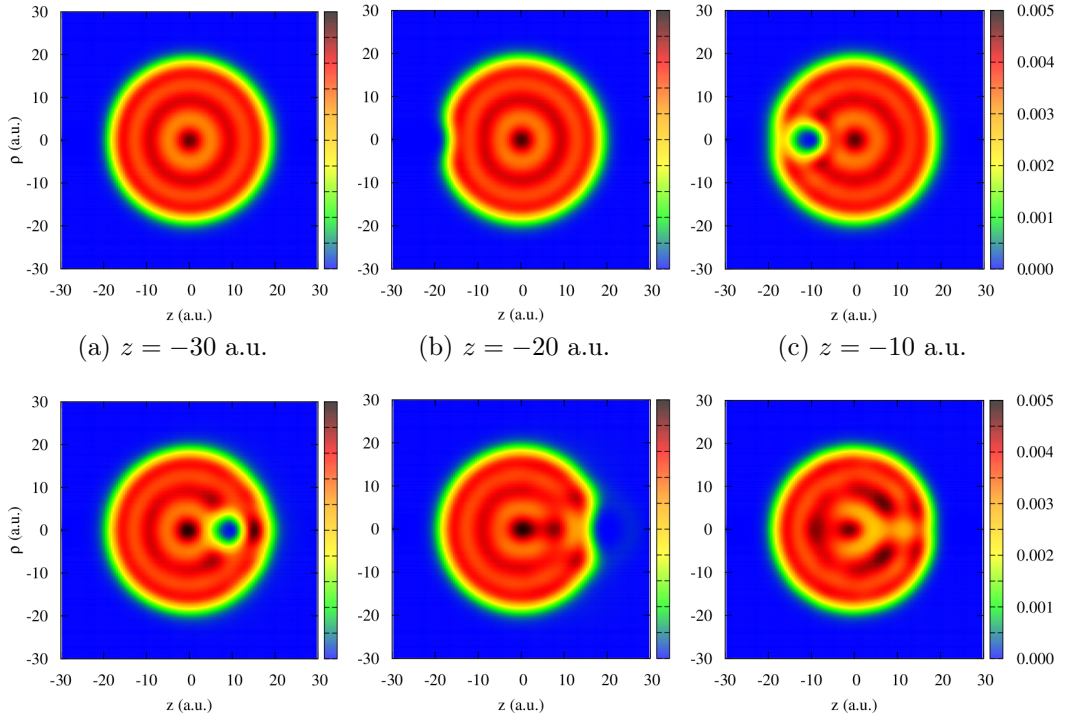

(a) $z = -30$ a.u. (b) $z = -20$ a.u. (c) $z = -10$ a.u.

(d) $z = 10$ a.u. (e) $z = 20$ a.u. (f) $z = 30$ a.u.

Figure 6.6: Electronic density of the spherical cluster Na_{106} as a function of (z, ρ) coordinates at different time steps. Cluster radius is $R_{cl} = 18.93$ a.u. Antiproton velocity is $v = 0.3$ a.u. Pictures correspond to six different antiproton positions: a) $z = -30$ a.u, b) $z = -20$ a.u, c) $z = -10$ a.u, d) $z = 10$ a.u, e) $z = 20$ a.u, f) $z = 30$ a.u.

pushes the cluster electrons away from its path and we can see the screening hole around the antiproton (Fig. 6.6c and 6.6d). When the antiproton enters the cluster, the screening hole is not yet fully developed (Fig. 6.6b) and the force is not sufficiently attractive. On the other hand, when the antiproton moves away from the cluster, the hole is still large (Fig. 6.6e), because the antiproton moves too fast for the adiabatic polarization limit to be valid. When the antiproton is already far from the cluster, we can still see some polarization at the surface of the cluster (Fig. 6.6f), which was not observed when the antiproton was approaching the cluster, at the same distance. (Fig. 6.6a). This is why the dissipative force on the antiproton on its way out of the cluster is larger than on its way in (see Fig. 6.5).

6.2 Friction coefficient

Knowing the dissipative force we now can calculate the friction coefficient using Eq. (6.5). The friction coefficient is shown in Fig. 6.7 as a function of the antiproton position for the cluster Na_{106}. We can see that far from the cluster surface the friction coefficient is equal to zero. Approaching the cluster surface, the friction coefficient increases showing a behavior almost independent on velocity. Inside the cluster the friction coefficient oscillates. At low velocities of the antiproton the oscillations are very large, because in this case cluster size effects play a role and strong oscillations in the electronic density of the cluster arise. However, in the case of the fast antiproton motion, the collision timescale is shorter and the antiproton creates a wake behind similar to the one arising in an infinite medium. We compare our results with the friction coefficient obtained using the local density friction approximation (LDFA, orange line). In the LDFA, the friction coefficient of the projectile is that of the same projectile moving in a homogeneous free electron gas (FEG) with electron density equal to that of the system at the point in which the projectile is located. The LDFA has been successfully applied, for instance, for the description of electron-hole pairs excited in physico-chemical processes at surfaces [62, 106].

From Fig. 6.7 we can see that the values of the friction coefficient obtained with LDFA and with TDDFT are of the same order of magnitude. Let us look at the friction coefficient in the area close to the surface of the cluster when the antiproton is approaching it (Fig. 6.8 left) and when the antiproton is moving away from the cluster surface (Fig. 6.8 right). From these plots we can see that the friction coefficient depends on the direction of motion of the antiproton. It is smaller for the motion towards the cluster and larger for the motion away from the cluster. In the left panel the LDFA friction coefficient is above the values obtained with TDDFT while in the right panel it is below the TDDFT values. We can understand this if we look at Fig. 6.6. Comparing panels Fig. 6.6a and Fig. 6.6f we see that, when the antiproton is moving towards the cluster but is still far away, the cluster is unperturbed. However, when the antiproton is at the same distance from the cluster but is moving away from it, the cluster is in an excited state, i.e., it is still polarized. The antiproton feels this polarization and therefore experiences a larger force, which leads to a larger value of the friction coefficient. In LDFA this effect is not taken into account because the friction

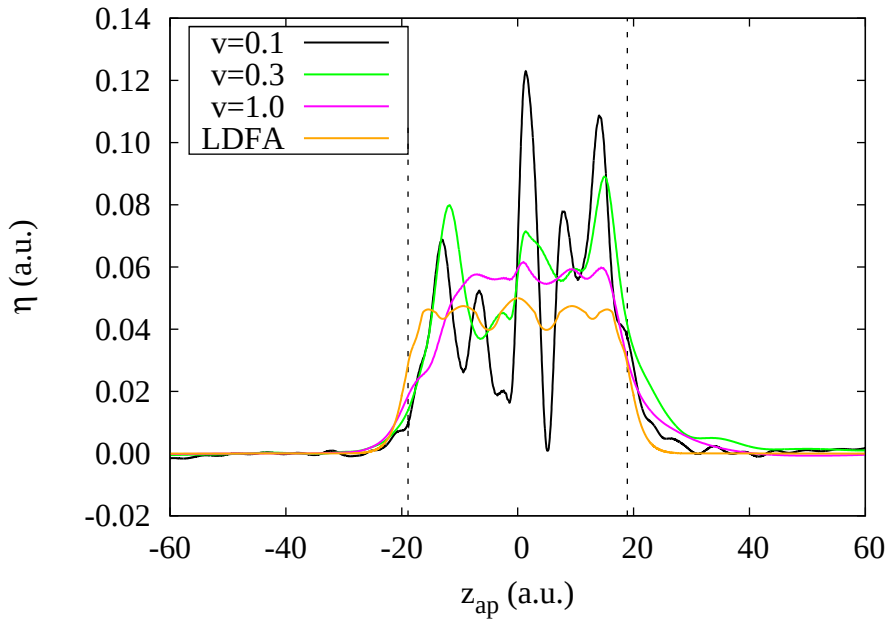

Figure 6.7: Friction coefficient for the antiproton moving with different velocities through the Na_{106} cluster. Orange line shows the result for the friction coefficient in LDFA approximation.

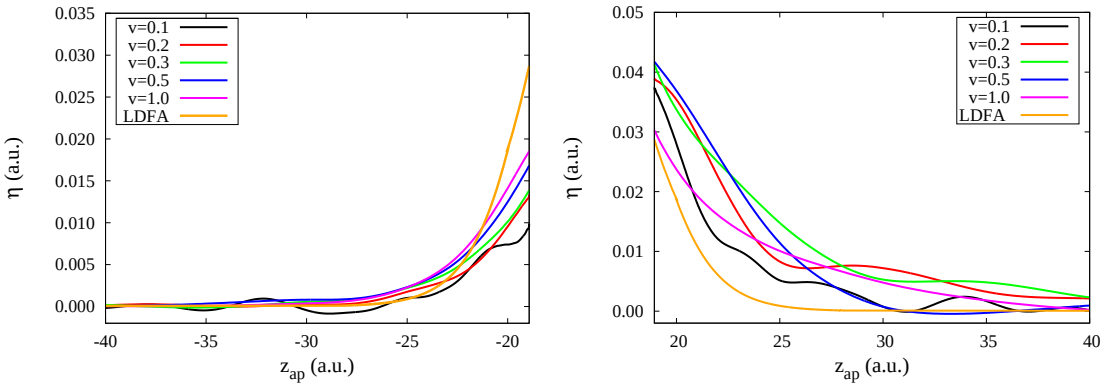

Figure 6.8: Friction coefficient for an antiproton moving with different velocities through the Na_{106} cluster: left – for the antiproton approaching the cluster up to the cluster surface; right – for the antiproton leaving the cluster, starting from the cluster surface. Orange line is the friction coefficient in LDFA approximation.

coefficient is calculated from the unperturbed local density at the position of the projectile. Hence, the LDFA friction coefficient is the same for the charge moving towards and away from the cluster surface.

The same behavior is observed in the case of a smaller cluster Na_{20} (Fig. 6.9) and in the case of a larger cluster Na_{1074} (Fig. 6.10). It is also similar for an Al_{106}

cluster (Fig. 6.11), which means that this behavior is general for the interaction of the antiprotons with metals. The fact that the friction coefficient depends on the

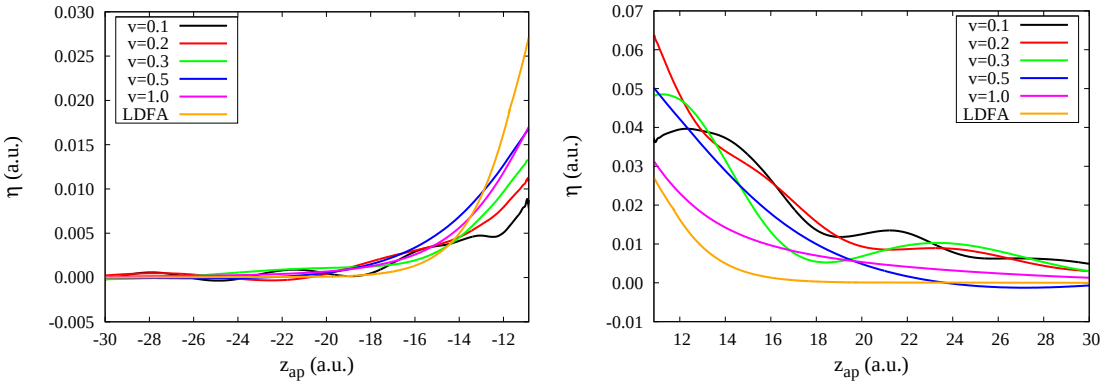

Figure 6.9: The same as Figure 6.8 but for the cluster Na_{20}. Cluster radius is 10.86 a.u.

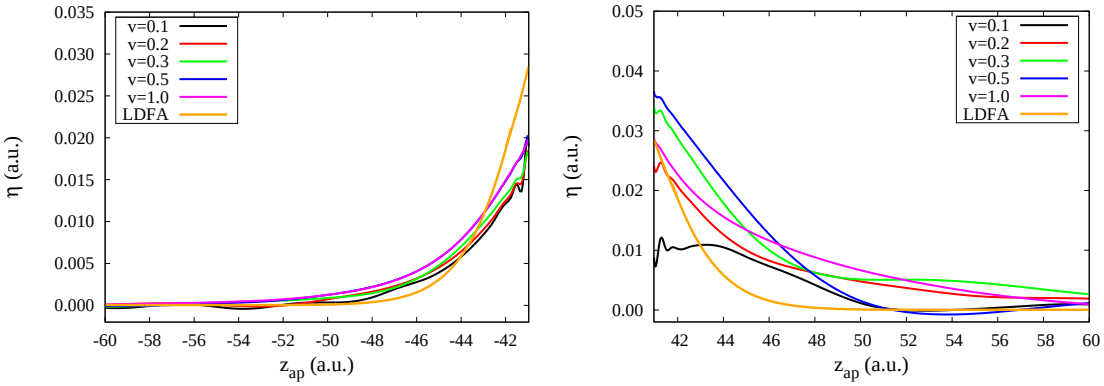

Figure 6.10: The same as Figs 6.8 and 6.9 but for the cluster Na_{1074}. Cluster radius is 40.96 a.u.

direction of motion of the projectile was already observed by Baer *et al.* They calculated the friction coefficient for a hydrogen atom colliding with a sodium cluster using TDDFT (Ehrenfest molecular dynamics) [38].

One can notice that at low projectile velocities the friction coefficient has oscillations which are not seen at high velocities. To explain this behavior we show in Fig. 6.12 and Fig. 6.13 the snapshots of the induced electronic density inside the cluster as a function of the (z, ρ) coordinates for low and high antiproton velocities. The three panels correspond to different positions of the antiproton as indicated on each plot. From Fig. 6.12 we can see that at low velocity the

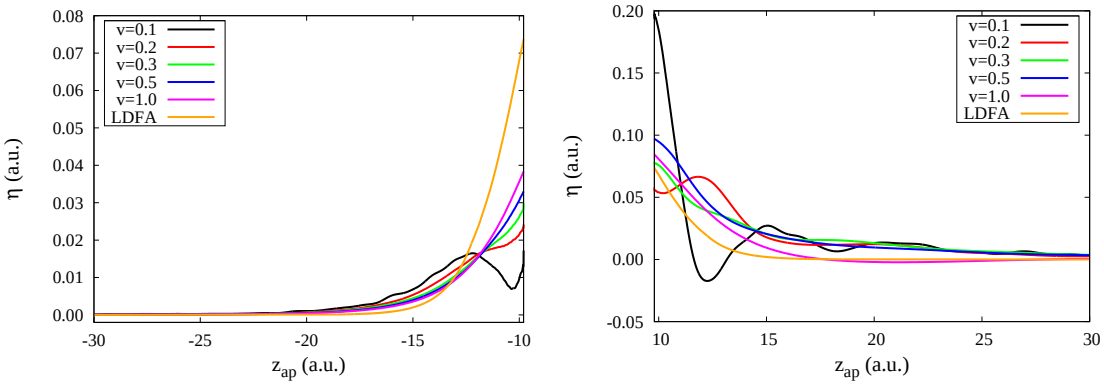

Figure 6.11: The same as Figs. 6.8 - 6.10 but for the cluster Al_{106}. Cluster radius is 9.8 a.u.

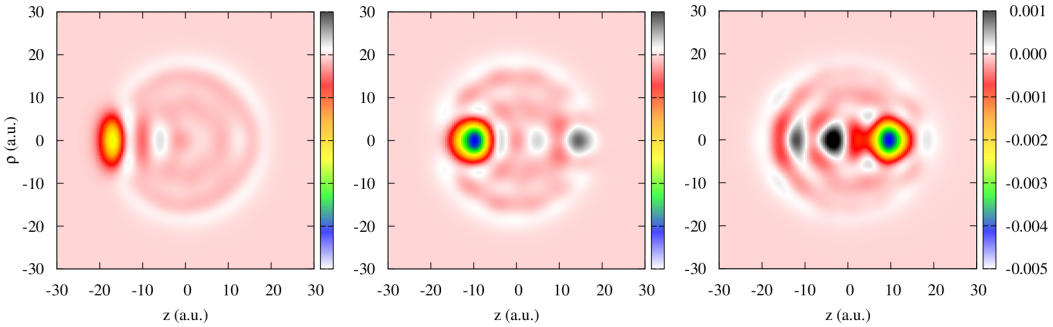

(a) $z = -20$ a.u. (b) $z = -10$ a.u. (c) $z = 10$ a.u.

Figure 6.12: Change in electronic density of the spherical cluster Na_{106} as a function of (z, ρ) coordinates at different time steps. Cluster radius is $R_{cl} = 18.93$ a.u. Antiproton velocity is $\upsilon = 0.1$ a.u. Pictures correspond to three different antiproton positions: a) $z = -20$ a.u, b) $z = -10$ a.u, c) $z = 10$ a.u.

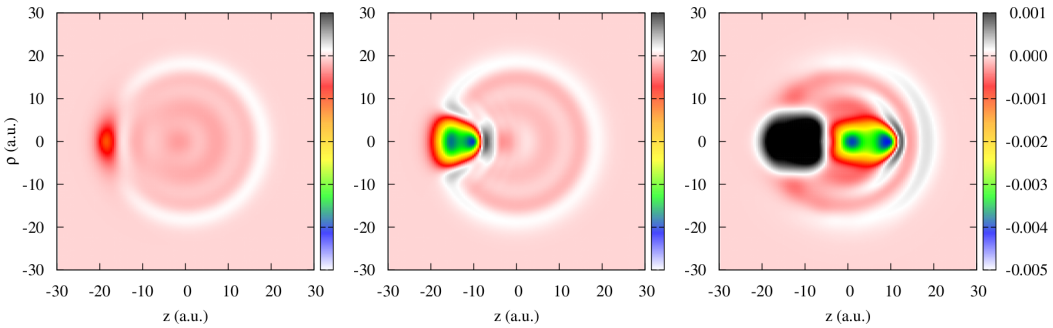

(a) $z = -20$ a.u. (b) $z = -10$ a.u. (c) $z = 10$ a.u.

Figure 6.13: The same as Fig. 6.12, but for the antiproton velocity $\upsilon = 1$ a.u.

antiproton excites the cluster electrons yet before crossing the surface of the cluster. The oscillation wave of the cluster electrons moves towards the other side of the cluster and then turns back. Therefore, it can act back on the projectile which by that time is entering the cluster. The rebound of these excited electrons at the cluster surface is reflected in the force as oscillations. Therefore, the oscillations are a consequence of the finite size of our system and would not be found, in principle, in an infinite system, as our results for the largest cluster suggest (see Fig. 6.10).

At large projectile velocity (Fig. 6.13) the situation is completely different. There is no wave front moving back because the cluster electrons are slower than the projectile and the force shows no oscillations. The projectile creates a wake behind it. The screening cloud surrounding the antiproton is strongly asymmetric, which is a sign of the nonadiabaticity of the process.

6.3 Conclusions

In summary, the friction coefficient obtained with TDDFT is showing a behavior nearly independent on the velocity for velocities below 1 a.u., but depends on the projectile-surface distance. In other words, the friction coefficient depends on the density profile of the cluster. The direction of motion of the projectile (towards or away from the cluster) plays an important role for all systems studied. The reason for that is that the electronic state of the cluster is not the same at different stages of the collision. We have shown that due to the polarization effects the friction coefficient on the way out of the cluster is larger than the friction coefficient on the way into the cluster in many cases. The LDFA results are in qualitative agreement with our TDDFT results. However, in the LDFA, the friction coefficient only depends on the local electronic density and therefore this approximation does not take into account the asymmetry in the polarization effects discussed above.

These conclusions are valid for all cluster sizes due to the local character of the screening process. For the same reason our results for an antiproton approaching the surface of a metal cluster are expected to be reasonably similar in the case of an infinite metal surface.

The total and the induced density plots help to interpret the obtained results

for the forces and the friction coefficient. In particular, they are useful to explain the existence of oscillations in the friction coefficient at low projectile velocities.

Chapter 7

Summary and outlook

In summary, in this thesis we focused on the study of the dynamic screening and energy loss of charged (antiproton, electron, proton, molecular hydrogen ion) and neutral (hydrogen atom and molecule) particles interacting with spherical jellium clusters. The time-dependent density functional theory (TDDFT) is used to calculate the time-evolution of the electronic density inside the cluster in response to the field of the moving projectiles. The real-time TDDFT approach is an efficient tool for studying dynamical processes in matter in a broad range of projectile energies. The use of this method has allowed us to understand more about the energy loss and dynamic screening processes when a particle penetrates a solid.

In particular, in Chapter 4 we used a semi-classical model to study the energy loss of an electron photoemitted from the center of a metal cluster or from an atom adsorbed on the cluster surface. We have shown that the dynamic screening of the core-hole left behind affects significantly the movement of the photoemitted electron. Namely, it leads to the reduction of the electronic energy loss. The reduction is especially large at low electron velocities. This is a consequence of the repulsive (accelerating) force acting on the electron from the cluster electrons piled up around the hole at the first stage of the photoemission, when the photoemitted electron is still close to the hole. In the adiabatic limit (very low electron velocities) we expect to recover the reduction of the binding energy of the hole due to the screening provided by the metal. This is routinely taken into account in the analysis of photoemission spectroscopy from core shells. However, in our analysis we stressed the importance of the coupled electron-hole dynamic screening, and how the overall effect must depend on the average velocity of the

photoemitted electron, i.e., on the photon energy used to create the excitation. We stressed as well the importance of the coupled electron-hole dynamic screening. Further steps in the investigation of this subject can be the calculation of the photoemission spectra including the effect of the hole screening in order to provide information that can be used to interpret photoemission experiments and to obtain information about the dynamics of screening from them.

In Chapter 5 we focused on the effect of the initial state of the metal cluster and of the projectile on the energy loss processes. First we calculated the energy loss of an antiproton traversing small Al clusters initially either in the ground state or in an excited state. We have shown that the antiproton interacting with a previously excited cluster loses less energy than the antiproton traversing a cluster in its ground state. This is partially due to the emission of one electron from the cluster during the first collision with the antiproton, which also leads to the blue shift of the cluster plasmon frequency.

Furthermore, in Chapter 5 we investigated how the energy loss of a particle can be modified by the presence of another particle in its close proximity. This was done for two different systems, namely, two antiprotons and two protons (and hydrogen atoms) with spherical jellium cluster. When dealing with two antiprotons oriented parallel to the direction of motion, the main conclusion of our study is that the stopping power ratio (the ratio between the stopping of the pair divided by twice the stopping of a single projectile) oscillates around 1 for large distances between the antiprotons and for velocities larger than the Fermi velocity. The oscillations are due to the plasmon excited by the first antiproton in the cluster. We performed a dynamical calculation including the Coulomb force between the antiprotons and showed that inside the cluster the Coulomb repulsion between the two particles is completely screened. The complex effects of the dynamic screening can thus lead to an effective attraction between two negatively charged particles moving through a metallic medium.

In the second case, we have calculated the stopping ratio for a hydrogen dimer interacting with a spherical cluster with an effective electronic density representative of SiO_2 and compared our results with experiments. We have considered different orientations of the hydrogen dimer with respect to the direction of motion and a broad range of projectile velocities. We have emphasized the strong dependence of the stopping ratio on the charge-state of projectiles. This is instrumental to understand the experimental results. For the fully ionized hydrogen

dimer our calculated stopping ratio perfectly reproduced the experimental findings. Further study of this subject can include the calculation of the stopping power ratio for heavier projectiles, such as LiF. This will require the use of pseudopotentials instead of the Coulomb potential to represent the core of the atomic projectiles.

Finally, in Chapter 6 we studied the dissipative effects in the interaction of an antiproton colliding with spherical metal clusters of different densities and sizes. We have calculated the dissipative (friction) force acting on the antiproton and the friction coefficient. As a result we have shown that the friction coefficient for an antiproton approaching the cluster surface is almost independent of the size of the cluster. We also show that the friction coefficient is weakly dependent on the velocity of the antiproton for the range of velocities considered, but shows a strong dependence on the position outside the cluster, indicating that, as expected, it approximately follows the density profile. Interestingly, we show that the friction coefficient shows a systematic dependence on the direction of motion, namely, the friction coefficient is different for an antiproton approaching the cluster and going away from the cluster. This can be easily understood in terms of the dynamics of the cluster polarization which, at sufficiently large velocities, is delayed with respect to the antiproton motion. Our results are in qualitative agreement with the local density friction approximation (LDFA) frequently used to calculate the friction coefficient in the context of physico-chemical processes at surfaces.

Appendix A

Details of the three-dimensional calculations

The ground state of the hydrogen dimer in Section 5.3 is calculated in a two-dimensional cylindrical grid (ρ, z) with two protons of the dimer located on the $z-$axis and the center of mass of the dimer at $z = 0$.

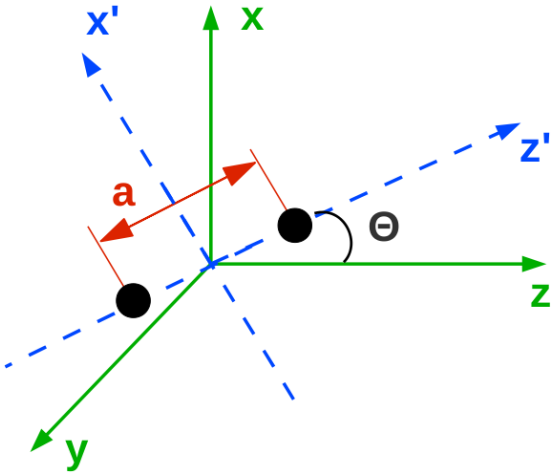

Figure A.1: Coordinate system for the hydrogen dimer. The dimer electrons are described in the coordinate system rotated by an angle Θ with respect to the global coordinate system.

After obtaining the ground state wave function of the dimer $\psi_{H_2}(\rho, z)$, we interpolate it into a three-dimensional grid, $\psi_{H_2}(\rho, \phi, z)$, of a larger size together with the cluster wave functions in order to start the time propagation. Different orientations of the dimer with respect to the direction of motion are introduced by rotating the system of coordinates of the dimer (x', y, z') by an angle Θ with

respect to the global system of coordinates (x, y, z), with the $y-$axis being the rotation axis (Fig. A.1), thus being $y' = y$. The hydrogen atoms are located on the $z'-$axis with the center of mass at the origin of coordinates. The distance between the two protons in the dimer is a = 2 a.u.

The coordinates of the two protons in the global system (x, y, z) are:

$$\begin{aligned} x_0 &= \pm\frac{a}{2}\sin(\Theta), \\ y_0 &= 0, \\ z_0 &= \pm\frac{a}{2}\cos(\Theta) + z_{\rm cm}, \end{aligned} \tag{A.1}$$

where $z_{\rm cm}$ is the position of the center of mass of the dimer, which can be defined as $z_{\rm cm} = z_{\rm init} + \upsilon t$, where υ is the velocity with which the dimer moves and $z_{\rm init}$ is the initial position of the dimer on the $z-$axis. The initial position of the dimer is chosen to be at $z_{\rm init} = -40$ a.u., far enough from the cluster surface to avoid interaction between the cluster and the projectile at the begining of the time propagation.

We use cylindrical coordinates in our time-dependent calculations, in which

$$\begin{aligned} x &= \rho\cos(\phi), \\ y &= \rho\sin(\phi), \\ z &= z. \end{aligned} \tag{A.2}$$

The dimer moves along the $z-$axis and crosses the cluster through the geometrical center. The parameters of the three-dimensional cylindrical grid (i.e., the step on each of the three axes) are the following: $\Delta z = 0.25$ a.u., $\Delta\rho = 0.35$ a.u., $\Delta\phi = 0.26$ rad. The time-step for the propagation is $\Delta t = 0.05$ a.u.

In order for the electrons of the dimer to move with the same velocity as the protons at $t = 0$ we need to apply a phase to the wave function computed for the static hydrogen dimer. This is done in the following way:

$$\psi_{\rm H_2}(\rho, \phi, z) = \psi_{\rm H_2}^{\rm static}(\rho, \phi, z)\; e^{i(z - z_{\rm init})\upsilon}. \tag{A.3}$$

The potential for each proton due to the electrons and the positive background

of the cluster is:

$$V(x_0, y_0, z_0) = \int_0^{2\pi} d\phi \int_0^{R_{\max}} \rho \; d\rho \int_{Z_{\min}}^{Z_{\max}} dz \frac{n_0^+(\rho, \phi, z) - n(\rho, \phi, z, t)}{\sqrt{(x - x_0)^2 + (y - y_0)^2 + (z - z_0)^2}} \; , \tag{A.4}$$

where $n_0^+(\rho, \phi, z)$ is the positive background density and $n(\rho, \phi, z, t)$ is the time-dependent electronic density.

In order to calculate the stopping power for the hydrogen dimer, we need to find the force acting on each proton along the trajectory ($z-$axis):

$$F_z = -\frac{\partial}{\partial z_0} \; V(x_0, y_0, z_0), \tag{A.5}$$

$$F_z = - \int_0^{2\pi} d\phi \int_0^{R_{\max}} \rho \; d\rho \int_{Z_{\min}}^{Z_{\max}} dz \; \frac{[n_+(\rho, \phi, z) - n(\rho, \phi, z, t)] \;\; (z - z_0)}{[(x - x_0)^2 + (y - y_0)^2 + (z - z_0)^2]^{3/2}} \; . \tag{A.6}$$

Another two components of the force along the $x-$axis, F_x, and along the $y-$axis, F_y, needed for the calculation of the torque on the dimer, are calculated in a way similar to Eq. (A.6).

The torque acting on the particle is:

$$\tau = \mathbf{F} \times \mathbf{r} \tag{A.7}$$

where $\mathbf{r}$ is the displacement vector, i.e., the distance from the point at which the torque is calculated to the point at which the force is applied. In our case the torque is computed with respect to the center of mass of the dimer. Taking into account the symmetry of the process, namely that the dimer axis is rotated in the (x, z)-plane and therefore $F_y = 0$, the torque on each atom is the following:

$$\begin{aligned} \tau_x &= 0, \\ \tau_y &= F_x \; z_0 - F_z \; x_0, \\ \tau_z &= 0. \end{aligned} \tag{A.8}$$

Here $z_0 = \pm\frac{a}{2}\cos(\Theta)$ and $x_0 = \pm\frac{a}{2}\sin(\Theta)$, because we calculate the torque with respect to the $y-$axis. Knowing the force and the torque on each atom in the dimer we can find the total force and the total torque on the dimer by summing up the individual contributions.

Resumen en castellano

La estructura electrónica y las propiedades de los sólidos, superficies y nanoestructuras se pueden estudiar experimentalmente mediante diferentes técnicas espectroscópicas. En estos experimentos, el material se estudia mediante la interacción con partículas incidentes tales como electrones (espectroscopía electrónica de perdida de energía, EELS), fotones (espectroscopía de fotoemisión, PES), o iones (dispersión de iones, IS). Los proyectiles que penetran en el sólido o en la superficie crean excitaciones electrónicas en el material estudiado. La descripción cuantitativa de la dinámica de dichas partículas en las superficies y en los sólidos, así como la dinámica electrónica asociada, es esencial para la correcta interpretación de los resultados de los experimentos.

Esta tesis está dedicada al estudio de las excitaciones electrónicas creadas durante la interacción de partículas cargadas y neutras con agregados metálicos. Las excitaciones electrónicas están asociadas con la disipación de la energía, lo que en nuestro caso significa la transferencia de energía cinética de un proyectil en movimiento a los electrónes de un agregado metálico o viceversa. En concreto, estudiamos los procesos de disipación en fenómenos físicos tales como el apantallamiento electrónico y el frenado de electrónes durante la fotoemisión, el apantallamiento electrónico y el frenado de iones y moléculas que atraviesan agregados metálicos y la fricción electrónica en superficies metálicas. La investigación de estos procesos nos permite obtener información sobre las propiedades de ambos, el material estudiado y el proyectil.

La complejidad de estos procesos dinámicos en sólidos es un reto para los métodos teóricos. En esta tesis estudiamos la interacción de los agregados metálicos con partículas en movimiento utilizando una metodología eficiente basada en la teoría del funcional de la densidad dependiente del tiempo (TDDFT), un método *ab initio* basado en la mecánica cuántica que nos permite estudiar los procesos dinámicos que tienen lugar durante la interacción de las partículas con la mate-

ria en una amplia gama de velocidades de los proyectiles. Más concretamente, usamos el método de propagación de paquetes de onda (WPP), una herramienta eficaz para el tratamiento de procesos dinámicos en el dominio temporal.

En esta tesis estudiamos estos fenómenos en dos contextos diferentes, aunque los métodos que usamos para este propósito son similares en ambos casos.

El primer tema, que se describe en el Capítulo 4 de la presente tesis, se relaciona con la fotoemisión. La fotoemisión, o el efecto fotoeléctrico, es la emisión de los electrones de un objeto después de la absorción de un fotón. Fue descubierto hace más de 100 años por H. Hertz. En 1905 Albert Einstein explicó este efecto como un fenómeno cuántico. Hoy en día, la espectroscopía de fotoemisión es una de las técnicas más importantes que se utilizan para estudiar la estructura de moléculas, superficies y sólidos. En esta técnica se utiliza un analizador para medir la energía cinética de los electrones emitidos. El espectro de fotoemisión, como resultado de tal experimento, proporciona información sobre las energías de enlace de los electrones de valencia o más ligados en el material, dependiendo de la energía de los fotones entrantes (UV o rayos X). Esto permite analizar la composición del material estudiado, así como su estado electrónico y químico.

En los últimos años, los avances en la tecnología láser han hecho posible el desarrollo de la espectroscopía de fotoemisión en el rango de attosegundos (1 as $= 10^{-18}$ s). Estas espectroscopías permiten el acceso a la escala de tiempo del movimiento electrónico en los átomos. Debido a este avance experimental, hay un creciente interés en la descripción teórica de los procesos electrónicos dinámicos que tienen lugar en la escala de tiempo de attosegundos. Por eso, en esta tesis estudiamos el apantallamiento dinámico y la pérdida de energía de un electrón emitido desde un agregado metálico, así como la dinámica del apantallamiento del hueco localizado dejado atrás. Además estudiamos el caso de la fotoemisión desde un adsorbato sobre la superficie del agregado. En este caso, además de los procesos de pérdida de energía y apantallamiento se analiza la transferencia de carga del sustrato de metal al adsorbato.

Consideramos el caso en que un electrón interno es fotoemitido desde uno de los átomos en el agregado metálico (o el átomo adsorbido). El movimiento del electrón está representado clásicamente, mientras que la dinámica de la densidad electrónica del agregado se calcula con TDDFT. Calculamos la pérdida de energía del electrón emitido para velocidades diferentes. Como resultado vemos que el apantallamiento dinámico del hueco creado por los electrones del agregado afecta

al movimiento del electrón emitido, lo que da lugar a una reducción significativa de la energía perdida por el fotoelectrón. Esto es el resultado de una fuerza de aceleración debido al apilamiento de carga electrónica alrededor del hueco. Este efecto depende de la velocidad y es mayor cuando menor es la velocidad del electrón emitido. La aceleración observada del electrón emitido se mantiene incluso en un cálculo más realista en el que se permite que la velocidad del electrón varíe de acuerdo con las ecuaciones de movimiento de Newton, incluyendo la atracción de Coulomb entre el hueco y el electrón.

En el caso de la fotoemisión desde el adsorbato se observa el mismo efecto. El electrón emitido desde el adsorbato se acelera por la carga electrónica transferida del agregado metálico al adsorbato, así como por la carga apilada en la superficie para apantallar el hueco (carga imagen). Hemos demostrado que la cantidad de energía obtenida por el electrón emitido debido al apantallamiento del hueco depende no solo de la velocidad del electrón, sino también de la distancia entre la superficie y el adsorbato. La principal razón detrás de dicha dependencia está en los diferentes procesos de transferencia de carga que acompañan la fotoemisión en cada caso. Hemos demostrado que, dependiendo de la distancia entre el agregado metálico y el átomo adsorbido, los electrones del agregado pueden pasar a un nivel más ligado del átomo y permanecer allí o pasar al nivel resonante $(2s + 2p_z)$ resultando en oscilaciones de la densidad electrónica con el tiempo.

El segundo tema, que se describe en los Capítulos 5 y 6 de la tesis, se relaciona con los procesos de pérdida de energía y los efectos disipativos en la interacción de antiprotones y protones, así como de moléculas, con agregados metálicos de diferentes tamaños. Una partícula cargada moviéndose a través de un objeto metálico es capaz de crear excitaciones electrónicas en el medio a expensas de su propia energía cinética. La investigación sobre este fenómeno ha sido amplia en física de materia condensada y ciencia de materiales debido a su relevancia en varios campos fundamentales y aplicados, tales como el daño por radiación, la física médica, y la pulverización catódica de iones.

En el Capítulo 5 investigamos cómo el poder de frenado para el proyectil en función de la velocidad puede cambiar dependiendo de las condiciones iniciales, tales como el estado de excitación inicial del agregado (si se encuentra en su fundamental o no) y la presencia de otra partícula en las proximidades del proyectil en movimiento. En primer lugar, calculamos la pérdida de energía de un antiprotón atravesando un pequeño agregado de aluminio, tanto cuando el agregado está

inicialmente en el estado fundamental como cuando está inicialmente en un estado electrónico excitado. Se muestra que el antiprotón pierde menos energía al penetrar una partícula previamente excitada. Mostramos también que el proyectil crea un plasmón en la partícula y que el máximo de la frecuencia de plasmón se traslada a frecuencias más altas en la colisión con el agregado previamente excitado. Esto se corresponde con el periodo más corto y la amplitud más grande observados en las oscilaciones de la densidad electrónica después de la segunda colisión del antiprotón con el agregado metálico.

En segundo lugar, investigamos el *efecto de vecindad*, es decir, como cambia el poder de frenado para un proyectil moviéndose próximo a otro proyectil. Investigamos este efecto para dos antiprotones en función de la velocidad de los proyectiles y de la distancia entre ellos. Para cuantificar el efecto de vecindad en la pérdida de energía de dos partículas hacemos el cálculo del poder de frenado relativo, R. El poder de frenado relativo es el cociente entre el poder de frenado total de la agrupación de dos antiprotones y el doble del poder de frenado para un solo antiprotón. Hemos demostrado que a bajas velocidades de los antiprotones y a grandes distancias entre ellos el poder de frenado relativo es igual a uno. A velocidades medias y altas el poder de frenado relativo oscila alrededor de uno y la causa de las oscilaciones es el plasmón creado por los antiprotones en el metal. A distancias cortas entre los antiprotones el poder de frenado relativo tiene un mínimo que corresponde a diferentes distancias entre los antiprotones dependiendo de la velocidad.

Además, hemos estudiado en detalle la pérdida de energía de cada antiprotón individualmente y hemos demostrado que el primer antiprotón crea el plasmón que afecta al movimiento del segundo antiprotón. Hemos demostrado también que, para algunas distancias entre los antiprotones, la segunda partícula se puede acelerar en vez de ser frenada. Para ello, hemos realizado un cálculo dinámico real en el que permitimos que las velocidades de las dos partículas varíen de acuerdo a las ecuaciones de movimiento de Newton, incluyendo la fuerza inducida por los electrónes del medio en cada antiprotón y la fuerza de Coulomb entre ellos. Como resultado de este cálculo hemos demostrado que dentro del agregado metálico la repulsión de Coulomb entre los antiprotones está apantallada y, bajo ciertas condiciones iniciales, esto conduce a la atracción efectiva entre los antiprotones.

La última parte del Capítulo 5 está dedicada al estudio del efecto de vecindad en el frenado del dímero de hidrógeno. Utilizamos agregados con altas densidades

electrónicas que corresponden a las densidades efectivas en óxidos de Al, Ti y Si. En este caso investigamos el efecto de vecindad como una función de la energía cinética del proyectil y comparamos nuestros resultados con medidas experimentales. Realizamos el estudio utilizando cálculos tridimensionales y comparando el efecto de vecindad para dímeros con diferentes orientaciones (eje del dímero paralelo o perpendicular) con respecto a la dirección de movimiento. Nuestros resultados para el poder de frenado relativo están en buen acuerdo con los resultados experimentales si el estado de carga de los proyectiles se toma en cuenta correctamente. En particular, demostramos que para explicar los datos obtenidos a altas velocidades debe considerarse un proyectil totalmente ionizado.

Analizando individualmente el poder de frenado para cada protón en el dímero ionizado demostramos que el poder de frenado para el segundo protón es mucho más grande que para el primero, cuando el dímero está orientado paralelamente. Esta observación se correlaciona con la mayor acumulación de carga inducida calculada alrededor del segundo protón con respecto al primer protón y a un protón que viaje sólo. Esto es una consecuencia de la respuesta de los electrones del medio a la perturbación producida por el par de protones y a la estructura cónica de la nube de apantallamiento para altas velocidades del proyectil. Como resultado, la mayor parte de la nube de apantallamiento se encuentra detrás del segundo protón que a su vez apantalla al primer protón de la influencia de los electrones apilados. Esto da lugar a un poder de frenado mayor para el segundo protón en el dímero. Para la orientación perpendicular del dímero la imagen es completamente diferente. La nube de apantallamiento es igual para ambos protones y similar a la nube de apantallamiento de un único protón.

El Capítulo 6 está dedicado a la investigación de la fuerza disipativa y de fricción experimentada por un antiprotón que penetra un agregado metálico. Se demuestra que el coeficiente de fricción es casi independiente de la velocidad del proyectil, pero depende fuertemente de la distancia entre la partícula y la superficie del agregado. En otras palabras, el coeficiente de fricción depende del perfil de densidad electrónica del agregado metálico. La dirección del movimiento del proyectil (entrando o saliendo de la partícula) también influye en la fuerza disipativa calculada para todos los sistemas considerados. Nuestros cálculos demuestran que, debido a los efectos de polarización de la superficie del agregado, el coeficiente de fricción para la partícula saliente es mayor que el coeficiente de fricción para la partícula entrante en la mayoría de los casos. Los resultados de

la aproximación de la fricción de densidad local (LDFA) están en acuerdo cualitativo con nuestros resultados TDDFT. Sin embargo, en la aproximación LDFA el coeficiente de fricción solamente depende de la densidad local y por lo tanto esta aproximación no tiene en cuenta los efectos de polarización del medio. Estas conclusiones son válidas para todos los tamaños de agregados considerados debido al carácter local del proceso de apantallamiento. Por la misma razón se espera que nuestros resultados para un antiprotón que penetra un pequeño agregado metálico puedan ser válidos en el caso de una superficie metálica infinita. Los gráficos de la densidad inducida y de densidad total ayudan a interpretar los resultados obtenidos para las fuerzas y para el coeficiente de fricción. En particular, pueden explicar la existencia de oscilaciones en el coeficiente de fricción a bajas velocidades de proyectil.

La conclusión final de este trabajo es que la metodología TDDFT en tiempo real es una herramienta muy eficaz para el estudio de los procesos electrónicos dinámicos en la materia. Permite describir con precisión la interacción de partículas atómicas con diferentes blancos en una amplia gama de energías del proyectil. El uso de este método nos ha permitido avanzar en la comprensión de los procesos de pérdida de energía y de apantallamiento dinámico cuando una partícula penetra en un sólido.

Publications

Part of the results presented in this thesis is published in the peer-reviewed journals:

- N. E. Koval, D. Sánchez-Portal, A. G. Borisov, and R. Díez Muiño, *Dynamic screening of a localized hole during photoemission from a metal cluster*, Nanoscale Res. Lett. 7:447, 2012.
- N. E. Koval, D. Sánchez-Portal, A. G. Borisov, and R. Díez Muiño, *Dynamic screening and energy loss of antiprotons colliding with excited Al clusters*, Nucl. Instr. Meth. B 317:56–60, 2013.

In preparation:

- N. E. Koval, A. G. Borisov, R. Díez Muiño, and D. Sánchez-Portal, *Dynamically induced attraction between external negative charges in metals.*
- N. E. Koval, A. G. Borisov, D. Sánchez-Portal, and R. Díez Muiño, *Charge transfer and dynamic screening processes in the photoemission from an adsorbate on a metal cluster.*
- N. E. Koval, A. G. Borisov, L. Rosa, P. L. Grande, D. Sánchez-Portal, and R. Díez Muiño, *Vicinage effect in the energy loss of H_2 dimers from TDDFT simulations.*

Bibliography

[1] A.G. Borisov, J.P. Gauyacq, and S.V. Shabanov. Wave packet propagation study of the charge transfer interaction in the F^--Cu(111) and -Ag(111) systems. *Surf. Sci.*, 487:243–257, 2001.

[2] E.V. Chulkov, A.G. Borisov, J.P. Gauyacq, D. Sánchez-Portal, V.M. Silkin, V.P. Zhukov, and P.M. Echenique. Electronic excitations in metals and at metal surfaces. *Chem. Rev.*, 106:4160–4206, 2006.

[3] A.G. Borisov, D. Sánchez-Portal, R. Díez Muiño, and P.M. Echenique. Building up the screening below the femtosecond scale. *Chem. Phys. Lett.*, 387:95–100, 2004.

[4] A.G. Borisov, D. Sánchez-Portal, R. Díez Muiño, and P.M. Echenique. Dimensionality effects in time-dependent screening. *Chem. Phys. Lett.*, 393: 132–137, 2004.

[5] M. Quijada, A.G. Borisov, R. Díez Muiño, and P.M. Echenique. Time-dependent density functional calculation of the energy loss of antiprotons colliding with metallic nanoshells. *Phys. Stat. Sol.*, 205:1312–1316, 2008.

[6] M. Quijada, A.G. Borisov, I. Nagy, R. Díez Muiño, and P.M. Echenique. Time-dependent density-functional calculation of the stopping power for protons and antiprotons in metals. *Phys. Rev. A*, 75:042902, 2007.

[7] URL http://www.development.root-1.de/Atomic_Blender.php.

[8] U. Heiz and U. Landman (Eds.). *Nanocatalysis*. Springer-Verlag, 2007.

[9] G. W. Bryant, F. J. García de Abajo, and J. Aizpurua. Mapping the plasmon resonances of metallic nanoantennas. *Nano Lett.*, 8(2):631–636, 2008.

[10] T. B. Hoang, G. M. Akselrod, C. Argyropoulos, J. Huang, D. R. Smith, and M. H. Mikkelsen. Ultrafast spontaneous emission source using plasmonic nanoantennas. *Nat. Commun.*, 6:7788, 2015.

[11] H. A. Atwater and A. Polman. Plasmonics for improved photovoltaic devices. *Nat. Mater.*, 9:205–213, 2010.

[12] X. Li, W. C. H. Choy, L. Huo, F. Xie, W. E. I. Sha, B. Ding, X. Guo, Y. Li, J. Hou, J. You, and Y. Yang. Dual plasmonic nanostructures for high performance inverted organic solar cells. *Adv. Mater.*, 24(22):3046–3052, 2012.

[13] F. Pincella, K. Isozaki, and K. Miki. A visible light-driven plasmonic photocatalyst. *Light: Sci. Appl.*, 3:e133, 2014.

[14] P. Wang, B. Huang, Y. Dai, and M.-H. Whangbo. Plasmonic photocatalysts: harvesting visible light with noble metal nanoparticles. *Phys. Chem. Chem. Phys.*, 14:9813–9825, 2012.

[15] L. Polavarapu and L. M. Liz-Marzán. Towards low-cost flexible substrates for nanoplasmonic sensing. *Phys. Chem. Chem. Phys.*, 15:5288, 2013.

[16] M. Li, S. K. Cushing, and N. Wu. Plasmon-enhanced optical sensors: a review. *Analyst*, 140:386–406, 2015.

[17] T. G. Dietz, M. A. Duncan, D. E. Powers, and R. E. Smalley. Laser production of supersonic metal cluster beams. *J. Chem. Phys.*, 74:6511–6512, 1981.

[18] A. W. Castleman Jr. and Puru Jena. Cluster: a bridge between disciplines. *PNAS*, 103(28), 2006.

[19] W. D. Knight, K. Clemenger, W. A. de Heer, W. A. Saunders, M. Y. Chou, and M. L. Cohen. Electronic shell structure and abundances of sodium clusters. *Phys. Rev. Lett.*, 52:2141, 1984.

[20] W. Ekardt. Work function of small metal particles: Self-consistent spherical jellium-background model. *Phys. Rev. B*, 29:1558, 1984.

[21] D. E. Beck. Self-consistent calculation of the polarizability of small jellium spheres. *Phys. Rev. B*, 30:6935–6942, 1984.

[22] W. A. de Heer. The physics of simple metal clusters: experimental aspects and simple models. *Rev. Mod. Phys.*, 65:611, 1993.

[23] W. Schattke and M. A. Van Hove. *Solid-State Photoemission and Related Methods: Theory and Experiment.* WILEY-VCH, Berlin, 2003.

[24] Friedrich Reinert and Stefan Hüfner. Photoemission spectroscopy - from early days to recent applications. *New J. Phys.*, 7:97, 2005.

[25] A. Schmidt-Ott, P. Schurtenberger, and H. C. Siegmann. Enormous yield of photoelectrons from small particles. *Phys. Rev. Lett.*, 45:1284–1287, 1980.

[26] C. Noguera, D. Spanjaard, and J. Friedel. Dynamic screening of core hole. I. Semiclassical model. *J. Phys. F: Metal Phys.*, 9:1189, 1979.

[27] Zachary H. Levine. Dynamic screening effects in photoemission from oriented acetylene. *Phys. Rev. A*, 36:1181–1186, 1987.

[28] Z. Wei, F. O. Schumann, C. H. Li, L. Behnke, G. Di Filippo, G. Stefani, and J. Kirschner. Dynamic screening probed by core-resonant double photoemission from surfaces. *Phys. Rev. Lett.*, 113:267603, 2014.

[29] D. Bauer. Modeling the core-hole screening in jellium clusters using density functional theory. *New Journal of Physics*, 14:055012, 2012.

[30] A. L. Cavalieri, N. Müller, Th. Uphues, V. S. Yakovlev, A. Baltuska, B. Horvath, B. Schmidt, L. Blümel, R. Holzwarth, S. Hendel, M. Drescher, U. Kleineberg, P. M. Echenique, R. Kienberger, F. Krausz, and U. Heinzmann. Attosecond spectroscopy in condensed matter. *Nature*, 449:1029–1032, 2007.

[31] R. Díez Muiño, D. Sánchez-Portal, V. M. Silkin, E. V. Chulkov, and P.M. Echenique. Time-dependent electron phenomena at surfaces. *P. Natl. Acad. Sci. USA*, 108:971, 2011.

[32] A. K. Kazansky and P.M. Echenique. One-electron model for the electronic response of metal surfaces to subfemtosecond photoexcitation. *Phys. Rev. Lett.*, 102:177401, 2009.

[33] C. Lemell, B. Solleder, K. Tőkési, and J. Burgdörfer. Simulation of attosecond streaking of electrons emitted from a tungsten surface. *Phys. Rev. A*, 79:062901, 2009.

[34] E. E. Krasovskii. Attosecond spectroscopy of solids: Streaking phase shift due to lattice scattering. *Phys. Rev. B*, 84:195106, 2011.

[35] I. Nagy, A. Arnau, and P.M. Echenique. Screening and stopping of charged particles in an electron gas. *Phys. Rev. B*, 48:5650, 1993.

[36] P.M. Echenique, R.M. Nieminen, J.C. Ashley, and R.H. Ritchie. Nonlinear stopping power of an electron gas for slow ions. *Phys. Rev. A*, 33:897, 1986.

[37] I. Nagy, A. Arnau, and P.M. Echenique. Nonlinear stopping power and energy-loss straggling of an interacting electron gas for slow ions. *Phys. Rev. A*, 40:987, 1989.

[38] R. Baer and N. Siam. Real-time study of the adiabatic energy loss in an atomic collision with a metal cluster. *J. Chem. Phys.*, 121:6341, 2004.

[39] A.V. Krasheninnikov, Y. Miyamoto, and D. Tománek. Role of electronic excitations in ion collisions with carbon nanostructures. *Phys. Rev. Lett.*, 99:016104, 2007.

[40] J.M. Pruneda, D. Sánchez-Portal, A. Arnau, J.I. Juaristi, and E. Artacho. Electronic stopping power in LiF from first principles. *Phys. Rev. Lett.*, 99: 235501, 2007.

[41] A.A. Correa, J. Kohanoff, E. Artacho, D. Sánchez-Portal, and A. Caro. Nonadiabatic forces in ion-solid interactions: the initial stages of radiation damage. *Phys. Rev. Lett.*, 108:213201, 2012.

[42] M.A. Zeb, J. Kohanoff, D. Sánchez-Portal, A. Arnau, J.I. Juaristi, and E. Artacho. Electronic stopping power in gold: The role of d electrons and the H/He anomaly. *Phys. Rev. Lett.*, 108:225504, 2012.

[43] A. Castro, M. Isla, J. I. Martinez, and J. A. Alonso. Scattering of a proton with the Li_4 cluster: Non-adiabatic molecular dynamics description based on time-dependent density-functional theory. *Chem. Phys.*, 399:130, 2012.

[44] A. Lim, W. M. C. Foulkes, A. P. Horsfield, D. R. Mason, A. Schleife, E. W. Draeger, and A. A. Correa. Electron elevator: excitations across the band gap via a dynamical gap state. *Phys. Rev. Lett.*, 116:043201, 2016.

[45] F. Chandezon, C. Guet, B. A. Huber, D. Jalabert, M. Maurel, E. Monnand, C. Ristori, and J.C. Rocco. Critical sizes against Coulomb dissociation of highly charged sodium clusters obtained by ion impact. *Phys. Rev. Lett.*, 74:3784, 1995.

[46] J. Daligault, F. Chandezon, C. Guet, B.A. Huber, and S. Tomita. Energy transfer in collisions of metal clusters with multiply charged ions. *Phys. Rev. A*, 66:033205, 2002.

[47] V. Kasperovich, G. Tikhonov, K. Wong, P. Brockhaus, and V.V. Kresin. Polarization forces in collisions between low-energy electrons and sodium clusters. *Phys. Rev. A*, 60:3071, 1999.

[48] V. Kasperovich, K. Wong, G. Tikhonov, and V.V. Kresin. Electron capture by the image charge of a metal nanoparticle. *Phys. Rev. Lett.*, 85:2729, 2000.

[49] V. Kasperovich, G. Tikhonov, K. Wong, and V.V. Kresin. Negative-ion formation in collisions of low-energy electrons with neutral sodium clusters. *Phys. Rev. A*, 62:063201, 2000.

[50] A. Halder, A. Liang, Ch. Yin, and V.V. Kresin. Double and triple ionization of silver clusters by electron impact. *J. Phys.: Condens. Matter*, 24:104009, 2012.

[51] W. Brandt, A. Ratkowski, and R. H. Ritchie. Energy loss of swift proton clusters in solids. *Phys. Rev. Lett.*, 33:1325, 1974.

[52] Néstor R. Arista. Stopping of molecules and clusters. *Nucl. Instr. and Meth. B*, 164-165:108–138, 2000.

[53] R. Díez Muiño and A. Salin. Energy and angular momentum transfer in the excitation of electron-hole pairs by slow dimers. *Phys. Rev. B*, 62:5207, 2000.

[54] M. Alducin, R. Díez Muiño, J. I. Juaristi, and P. M. Echenique. Nonlinear effects in the energy loss of a slow dipole in a free-electron gas. *Phys. Rev. A*, 66:054901, 2002.

[55] M. Alducin, R. Díez Muiño, and A. Salin. Vicinage effects in the energy loss of slow LiH molecules in metals. *Nucl. Instr. and Meth. B*, 232:178–183, 2005.

[56] Z. L. Mišković, Y.-N. Wang, and Y.-H. Song. Dynamics of fast molecular ions in solids and plasmas: A review of recent theoretical developments. *Nucl. Instr. and Meth. B*, 256:57–65, 2007.

[57] S. M. Shubeita, M. A. Sortica, P. L. Grande, J. F. Dias, and N. R. Arista. Signature of plasmon excitations in the stopping ratio of fast hydrogen clusters. *Phys. Rev. B*, 77:115327, 2008.

[58] S. M. Shubeita, R. C. Fadanelli, J. F. Dias, P. L. Grande, C. D. Denton, I. Abril, R. Garcia-Molina, and N. R. Arista. Role of electronic excitations in the energy loss of H_2^+ projectiles in high-k materials. *Phys. Rev. B*, 80: 205316, 2009.

[59] S. M. Shubeita, P. L. Grande, J. F. Dias, R. Garcia-Molina, C. D. Denton, and I. Abril. Energy loss of swift H_2^+ and H_3^+ molecules in gold: Vicinage effects. *Phys. Rev. B*, 83:245423, 2011.

[60] P. Sigmund and A. Schinner. Stopping of swift hydrogen diclusters: oscillator model. *Eur. Phys. J. D*, 61:39–50, 2011.

[61] S. M. Shubeita, M. A. Sortica, P. L. Grande, J. F. Dias, and N. R. Arista. Signature of plasmon excitations in the stopping ratio of fast hydrogen clusters. *Phys. Rev. B*, 77:115327, 2008.

[62] J. I. Juaristi, M. Alducin, R. Díez Muiño, H. F. Busnengo, and A. Salin. Role of electron-hole pair excitations in the dissociative adsorption of diatomic molecules on metal surfaces. *Phys. Rev. Lett.*, 100:116102, 2008.

[63] Geert-Jan Kroes. Towards chemically accurate simulation of molecule-surface reactions. *Phys. Chem. Chem. Phys.*, 14:14966–14981, 2012.

[64] Jorge Kohanoff. *Electronic structure calculations for solids and molecules: theory and computational methods*. Cambridge University Press, 2006.

[65] R. O. Jones and O. Gunnarsson. The density functional formalism, its applications and prospects. *Rev. Mod. Phys.*, 61:689–746, 1989.

[66] Richard M Martin. *Electronic Structure. Basic theory and practical methods.* Cambridge University Press, 2004.

[67] P. Hohenberg and W Kohn. Inhomogeneous electron gas. *Phys. Rev.*, 136: B864–B871, 1964.

[68] W. Kohn and L.J. Sham. Self-consistent equations including exchange and correlation effects. *Phys. Rev.*, 140:A1133–A1138, 1965.

[69] E. Runge and E.K.U. Gross. Density-functional theory for time-dependent systems. *Phys. Rev. Lett.*, 52:997, 1984.

[70] C. Fiolhais, F.M.S. Nogueira, and M.A.L. Marques (Eds.). *A Primer in Density-Functional Theory.* Springer-Verlag, Berlin Heidelberg, 2003.

[71] M.A.L. Marques, N.T. Maitra, F.M.S. Nogueira, E.K.U. Gross, and A. Rubio (Eds.). *Fundamentals of Time-Dependent Density Functional Theory.* Springer-Verlag, Berlin Heidelberg, 2012.

[72] Matthias Brack. The physics of simple metal clusters: self-consistent jellium model and semiclassical approaches. *Reviews of Modern Physics*, 65:No. 3, 1993.

[73] Roy L. Johnston. *Atomic and Molecular Clusters.* Taylor and Francis, 2002.

[74] John A. Blackman. *Metallic Nanoparticles, in: Prasanta Misra (ed.), The book series, Handbook of metal physics.* Elsevier B.V., 2009.

[75] N. W. Ashcroft and N. David Mermin. *Solid State Physics.* Harcourt College Publishers, Philadelphia, 1967.

[76] J.P Perdew and A. Zunger. Self-interaction correction to density-functional approximations for many-electron systems. *Phys. Rev. B*, 23:5048, 1981.

[77] O. Gunnarson and B.I. Lundqvist. Exchange and correlation in atoms, molecules, and solids by the spin-density-functional formalism. *Phys. Rev. B*, 13:4274, 1976.

[78] M. D. Feit, Jr. J. A. Fleck, and A Steiger. Solution of the Schrödinger equation by a spectral method. *J. Comput. Phys.*, 47:412, 1982.

[79] M. D. Feit and Jr. J. A. Fleck. Solution of the Schrödinger equation by a spectral method II: Vibrational energy levels of triatomic molecules. *J. Chem. Phys.*, 78:301, 1983.

[80] David J. Tannor. *Introduction to quantum mechanics: a time-dependent perspective*. University Science Books, 2nd edition, 2007.

[81] D. Kosloff and R. Kosloff. A Fourier method solution for the time-dependent Schrödinger equation as a tool in molecular dynamics. *J. Comput. Phys.*, 52:35–53, 1983.

[82] W. H. Press, S. A. Teukolsky, W. T. Vetterling, and B. P. Flannery. *Numerical Recipes in Fortran 77. The Art of Scientific Computing*. Cambridge University Press, 1986.

[83] J. W. Gadzuk and N. Šunjić. Excitation energy dependence of core-level X-ray-photoemission-spectra line shapes in metals. *Phys. Rev. B*, 12:524, 1975.

[84] H.-J. Freund and M. Neumann. Photoemission of molecular adsorbates. *Appl. Phys. A*, 47:3–23, 1988.

[85] Nils Mårtensson and Anders Nilsson. Core-level line shapes of adsorbates: effects of electronic and vibrational excitations. *J. Electron Spectrosc. Relat. Phenom*, 52:1–46, 1990.

[86] Helena Tillborg, Anders Nilsson, and Nils Mårtensson. Shake-up and shake-off structures in core level photoemission spectra from adsorbates. *J. Electron Spectrosc. Relat. Phenom*, 62:73–93, 1993.

[87] A. Sandell, A. Beutler, R. Nyholm, J. N. Andersen, S. Andersson, P. A. Brühwiler, N. Mårtensson, J. Libuda, K. Wolter, O. Seiferth, M. Bäumer, H. Kuhlenbeck, and H.-J. Freund. Observation of a low-energy adsorbate core-level satellite for CO bonded to palladium: coordination-dependent effects. *Phys. Rev. B*, 57:13199–13208, 1998-II.

[88] M. Häming, A. Schöll, E. Umbach, and F. Reinert. Adsorbate-substrate charge transfer and electron-hole correlation at adsorbate/metal interfaces. *Phys. Rev. B*, 85:235132, 2012.

[89] K. Hermann and P. S. Bagus. New mechanism for screening in core-level photoemission of adsorbates: Model studies. *Phys. Rev. B*, 28(2):560–567, 1983.

[90] O. Gunnarsson and K. Schönhammer. CO on Cu(100) – explanation of the three-peak structure in the X-ray-photoemission-spectroscopy core spectrum. *Phys. Rev. Lett.*, 41:1608, 1978.

[91] P. Nordlander and J. C. Tully. Energy shifts and broadening of excited hydrogen-atom levels in the vicinity of a metal surface. *Phys. Rev. Lett.*, 61:990, 1988.

[92] P. Nordlander and J. C. Tully. Energy shifts and broadening of atomic levels near metal surfaces. *Phys. Rev. B*, 42:5564, 1990-II.

[93] A. G. Borisov, V. Sametoglu, A. Winkelmann, A. Kubo, N. Pontius, J. Zhao, V. M. Silkin, J. P. Gauyacq, E.V. Chulkov, P.M. Echenique, and H. Petek. π resonance of chemisorbed alkali atoms on noble metals. *Phys. Rev. Lett.*, 101:266801, 2008.

[94] L.D. Landau and E.M. Lifshitz. *Electrodynamics of continuous media*. Pergamon Press, 2nd edition, 1984.

[95] P. M. Echenique. Interaction of slow ions with bulk and surfaces. *Nucl. Instr. and Meth. B*, 27:256–265, 1987.

[96] I. Nagy, A. Arnau, P.M. Echenique, and E. Zaremba. Low-velocity antiproton stopping power. *Phys. Rev. B*, 40(17):11983, 1989-I.

[97] Th. Fennel, K.-H. Meiwes-Broer, J. Tiggesbäumker, P.-G. Reinhard, P. M. Dinh, and E. Suraud. Laser-driven nonlinear cluster dynamics. *Rev. Mod. Phys.*, 82:1793, 2010.

[98] F. Calvayrac, P.-G. Reinhard, and E. Suraud. Nonlinear plasmon response in highly excited metallic clusters. *Phys. Rev. B*, 52:17056–17059, 1995.

[99] V. Kresin. Static electric polarizabilities and collective resonance frequencies of small metal clusters. *Phys. Rev. B*, 39:3042, 1989-I.

[100] F. Calvayrac, P.-G. Reinhard, E. Suraud, and C.A. Ullrich. Nonlinear electron dynamics in metal clusters. *Phys. Rep.*, 337:493, 2000.

[101] P. Ludwig, H. Kählert, and M. Bonitz. Ion-streaming induced order transition in three-dimensional dust clusters. *Plasma Phys. Control. Fusion*, 54: 045011, 2012.

[102] Zhaoyang Chen. *Molecular dynamics simulation of charged dusts in plasmas*. PhD thesis, Abteilung für physik und astronomie an der Ruhr Universität Bochum, 2004.

[103] C. D. Denton, I. Abril, M. D. Barriga-Carrasco, R. Garcia-Molina, G. H. Lantschner, J. C. Eckardt, and N. R. Arista. Effect of the neutral charge fraction in the coulomb explosion of H_2^+ ions through aluminum foils. *Nucl. Instr. and Meth. B*, 193:198–203, 2002.

[104] S. M. Shubeita, R. C. Fadanelli, J. F. Dias, and P. L. Grande. Determination of film thicknesses through the breakup of H_2^+ ions. *Surf. Sci.*, 608:292–296, 2013.

[105] M. Bergsmann, W. Raab, G. Schrenk, F. Kastner, R. Díez Muiño, A. Arnau, A. Salin, P. Bauer, and P. M. Echenique. Phase effect in stopping of H ions in Mg. *Phys. Rev. B*, 62:3153–3159, 2000-I.

[106] L. Martin-Gondre, M. Alducin, G. A. Bocan, R. Díez Muiño, and J. I. Juaristi. competition between electron and phonon excitations in the scattering of nitrogen atoms and molecules off tungsten and silver metal surfaces. *Phys. Rev. Lett.*, 108:096101, 2012.

Materials Physics Center

Centro de Física de Materiales

Materialen Fisika Zentroa

Donostia International Physics Center